Radiative Transfer in Highly Thick Media through Rayleigh and Raman Scattering with Atomic Hydrogen

Seok-Jun Chang

August 2021

Department of Astronomy and Space Science

The Graduate School

Sejong University

Radiative Transfer in Highly Thick Media through Rayleigh and Raman Scattering with Atomic Hydrogen

Seok-Jun Chang

A thesis submitted to the Faculty of the Sejong University in partial fulfillment of the requirements for the degree of Doctor of Philosophy in Department of Astronomy and Space Science.

August 2021

Approved by Hee-Won Lee

Major Advisor

Radiative Transfer in Highly Thick Media through Rayleigh and Raman Scattering with Atomic Hydrogen

by

Seok-Jun Chang

Approved _____

Graziano Rossi, Committee Chair

Approved _____

Benjamin L'Huillier, Committee Member

Approved _____

Yujin Yang, Committee Member

Approved _____

Kwang-Il Seon, Committee Member

Approved _____

Hee-Won Lee, Advisor

Disclaimer

I hereby declare that the work in this thesis is performed by the student alone, except where indicated below. Professor Hee-Won Lee is the thesis advisor and has contributed to the research.

Abstract

Radiative Transfer in Highly Thick Media through Rayleigh and Raman Scattering with Atomic Hydrogen

We adopt a Monte Carlo approach to investigate the formation of the various spectral line features through Rayleigh and Raman scattering in highly thick media of atomic hydrogen. Raman scattering considered in this work proceeds with an incidence of a far UV photon onto a hydrogen atom in the ground state $1s$ resulting in re-emission of an optical or IR photon with the hydrogen atom left in the excited $2s$ or $3s$ state, respectively. We developed a 3D Monte Carlo code, 'Sejong Radiative Transfer through Rayleigh and Raman Scattering (STaRS)', to trace far UV photons that are subject to Rayleigh and Raman scattering.

Far UV photons near Lyβ and Lyγ are relocated to optical photons near Hα and Hβ through Raman scattering, for which the efficiency peaks around line centers leading to the formation of broad wing features around Balmer lines. These broad wing features are prevalently found in symbiotic stars, wide binary systems of a hot white dwarf and a mass-losing giant. In fact, many symbiotic stars exhibit very broad Hα wings with a width of a few times 10^3 km s^{-1}. We find that in the two symbiotic stars Z An-

dromedae and AG Draconis, the Hβ wings are weaker and narrower than than the Hα counterparts, which is consistent with the Raman scattering origin.

A similar study was carried out to study the formation of broad Balmer wings in active galactic nuclei. The unification model of active galactic nuclei requires the presence of a thick molecular torus that obscures the broad line region near the supermassive black hole. In the presence of a neutral component with H I column density exceeding 10^{22} cm^{-2} in typical active galactic nuclei, the broad Lyα emission line can be Rayleigh scattered. In particular, Rayleigh scattered Lyα can be linearly polarized if the neutral region coincides with the molecular torus. Interestingly enough, the central part of Lyα for which the optical depth is huge is polarized in the direction that differs by $90°$ from the direction along which the far wing part of Lyα is polarized. Future spectropolarimetry of active galactic nuclei will shed much light on the presence of the molecular torus and the unification scheme of active galactic nuclei.

Lyα blobs are quite extended objects with a physical size ~ 100 kpc that are found in the high z universe with $z \sim 2-4$. We assume that the Lyα emission source is an active galaxy surrounded by an extended neutral region. Through a combination of resonance and Rayleigh scattering, Lyα photons spread out both in the physical space and wavelength space to

form a Lyα halo. The diffusion in the phase space through resonance and Rayleigh scattering of Lyα is also accompanied by the development of linear polarization. We compute the surface brightness and linear polarization of Lyα in order to make a quantitative comparison with observation. It is found the column density of the scattering medium is the major parameter to determine the size of the observable Lyα halos.

Contents

List of Figures

vi

x

List of Tables

Chapter 1

Introduction

Hydrogen is the most abundant element in the universe, which is, in the cosmological context, attributed to its simplest structure consisting of a proton and an electron. The two-body system of hydrogen is completely described by the Keplerian potential or equivalently Coulomb potential if we neglect small quantum effects such as the fine and hyperfine structures associated with the spins and also quantum field effects such as the Lamb shift. The Coulomb potential admits wave functions given in a closed form with analytic functions.

Having a deep interest in numbers, the Swiss mathematician Johann Balmer announced the simple formula in 1885 satisfied by the optical wavelengths of hydrogen lines, now known to be the Balmer series. Subsequently, Balmer's empirical formula was extended to accommodate the far UV and

infrared lines that are now called 'Lyman series' and 'Paschen, Brackett and Pfundt series.' The Rydberg formula, an extended formula of Balmer's formula, was explained by Bohr's atomic model and eventually fully understood with the advent of quantum mechanics contributed by Heisenberg, Schrodinger, and Dirac.

It comes as no surprise that the two leading Balmer lines Hα and Hβ were included in the Fraunhofer lines listed as 'C' and 'F,' respectively. Early spectral classification of stars was based on the absorption strength of Hα before the rearrangement was made according to the stellar temperature. However, there are exceptional or peculiar stars showing hydrogen emission lines instead of absorption.

In the case of an ionized medium, the hydrogen emission lines play an important role as the main coolant. It is often the case that very faint objects in a high redshift universe exhibit only discernible hydrogen emission lines with an addition of a handful of lines from other atomic or ionic species. Depending on the physical extent, these high z Lyα emission sources are classified into Lyα emitters (LAEs) and Lyα blobs. The physical extension of Lyα blobs ranges over 100 kpc with at best poorly resolved ionizing sources. Hayes et al. (2011) made a surprising discovery that Lyα emission from the Lyα blob 'LAB1' is polarized exhibiting a concentric pattern. The polarization of Lyα results from scattering with atomic hydrogen. Because

the escape of Lyα in a moderately optically thick medium is made after a large number of local scatterings followed by a significant frequency diffusion until the medium is optically thin, the development of polarized Lyα is closely associated with the scattering events occurring far off the resonance, which is in turn dependent on the scattering geometry, kinematics, and H I column density.

Numerous Lyα absorption features found in most quasar spectra provide essential information on the baryon distribution in the intergalactic space. These features are classified into Lyα forest, Lyman limit systems and damped Lyα systems, depending on the H I column density. In particular, a damped Lyα system is defined as an absorption feature with $N_{\mathrm{HI}} > 10^{20.3}$ cm^{-2}. Considering that this high column density is comparable to that of the disk of a spiral galaxy, damped Lyα systems are presumed to be a proto-disk galaxy found in the high z universe.

We may classify the nonrelativistic interaction of electromagnetic waves with atomic electron into Rayleigh and Raman scattering based on the elasticity. Rayleigh scattering refers to elastic scattering, where the frequencies of the incident and scattered photons are the same. In the case of Raman scattering, the initial and final electronic states differ by ΔE, which is accompanied by the difference $\Delta \nu = \Delta E/h$ between the frequencies of the incident and scattered photons. One good example of Raman interaction is

an inelastic process of Lyβ with a hydrogen atom in the ground state resulting in an emission of an optical photon Hα with the hydrogen atom left in the excited $2s$ state. In this way, Raman scattering plays an important role in converting far UV radiation into other spectral region with longer wavelength.

The cross sections for Rayleigh and Raman scattering can be computed using the time dependent second order perturbation theory, in which the interaction Hamiltonian may be written as

$$H_{\text{int}} = -\frac{e}{2m_e c}(\mathbf{p} \cdot \mathbf{A} + \mathbf{A} \cdot \mathbf{p}) + \frac{e^2}{2m_e c^2}\mathbf{A} \cdot \mathbf{A}. \qquad (1.1)$$

Here, $\mathbf{A}$ is the vector potential representing the incident and scattered radiation field. The matrix elements of the momentum operator $\mathbf{p}$ are closely associated with those of the dipole operators, leading to the selection rule of $\Delta l = \pm 1$ for a single electron atom like hydrogen.

The cross section as a function of incident wavelength is given by the infinite sum over all p states if the scattering hydrogen atom is initially in the ground $1s$ state. In particular, in the vicinity of a line center wavelength, the cross section is sharply peaked due to the dominant contribution from the single line transition. In this case, the cross section is well-approximated by a Lorentzian function, and the scattering process is referred to as resonance scattering, constituting the most common scattering processes in a scattering medium with a line center optical depth less than

$\tau_0 < 10^4$. Non-resonance scattering processes become important in highly thick media. Fig. 1.1 illustrates schematically various types of photon scattering with atomic hydrogen.

Highly thick neutral regions are found in an extended atmospheric region of an evolved giant. In particular, in a symbiotic star, a binary system of a giant and a white dwarf, the extended giant atmosphere can be probed through Rayleigh scattering when the giant eclipses the white dwarf. A more interesting case is obtained when Raman scattering of far UV radiation takes place in the neutral region around the giant. In fact, the broad emission features formed at 6830 Å and 7082 Å are found in about a half of symbiotic stars. These two features were identified as Raman-scattered features of far UV doublet lines O VI at 1032 Å and 1038 Å by Schmid (1989).

These special emission features are known only in symbiotic stars, consistent with the very special requirement for the formation of Raman-scattered O VI, which is the co-existence of a highly thick H I region and a strong far UV emission region. This unique condition is ideally met in symbiotic stars and also probably in active galactic nuclei. The strength and line profiles of Raman-scattered O VI features in symbiotic stars are determined by the H I column density, covering factor and kinematics of the neutral region with respect to the O VI emission region. High resolution and deep spectroscopy of Raman-scattered O VI provides important information regarding the mass

loss and mass transfer processes in symbiotic stars.

Raman scattering is invoked to be responsible for broad Balmer wings observed in symbiotic stars. It is also an interesting possibility that the same processes operate in active galactic nuclei. The efficiency of Raman scattering is strongly peaked around Lyman line centers, resulting in broad weak emission features around Balmer lines. Raman wings can also be an important spectroscopic tool to probe the H I distribution that is present along the observer's line of sight to the source.

Scattered radiation is also characterized by polarization. In particular, linear polarization may develop in an anisotropic scattering geometry and the relative motion between the emission and scattering regions gives rise to complicated line profiles including multiple-peak structures and broad wings. An excellent example is provided by spectropolarimetric observations of Seyfert 2 galaxies exhibiting broad lines in the linearly polarized fluxes, lending strong support to the unification model of active galactic nuclei (Miller & Goodrich 1990; Tran 2010).

In this thesis, I present my works on radiative transfer involving the scattering processes between far UV photon and atomic hydrogen. Fig. 1.2 summarizes the research works in which I have participated so far in relation to radiative transfer in thick neutral media. This thesis is organized as follows. In Chapter 2, I introduce the 3D Monte Carlo code 'STaRS,' which
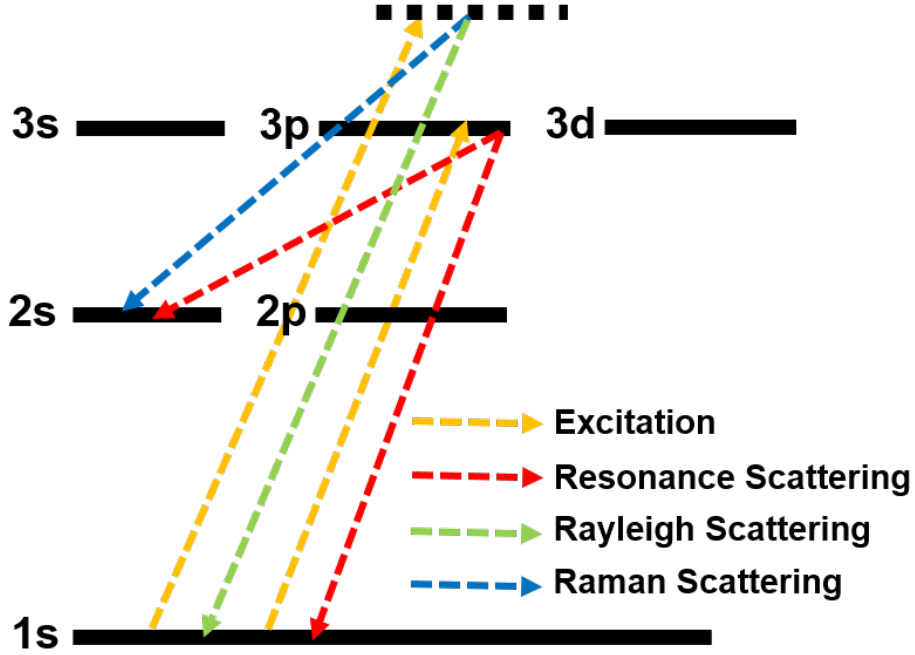
Figure 1.1: Schematic illustrations of the scattering processes with atomic hydrogen.

was developed for the radiative transfer involving Raman and Rayleigh scattering (Chang et al. 2020). Chapter 3 & 4 present the formation of broad wings near Balmer lines in symbiotic stars (Chang et al. 2018B) and active galactic nuclei (Chang et al. 2015). In Chapter 5, studied the polarization of scattered Lyα in AGN unification scheme (Chang et al. 2017). Chapter 6 represents current work, Lyα radiative transfer in the early universe (Chang et al. prep).

Literature	Subject	Type of Scattering	Object
Chang et al. 2015	Scattering Wing of Hα and Hβ	Raman Scattering	AGN
Lee et al. 2016	Raman Scattered O VI	Raman Scattering	Symbiotic Stars
Chang et al. 2017	Polarization of Lyα	Rayleigh scattering	AGN
Chang et al. 2018A	Resonantly Scattered Hα and Lyβ	Resonance Scattering	ISM
Chang et al. 2018B	Scattering Wing of Hα and Hβ	Raman Scattering Thomson Scattering	Symbiotic Stars
Choi et al. 2020	Raman scattered He II	Raman scattering	Planetary Nebulae
Chang et al. 2020	Grid-Based Simulation	Rayleigh scattering Raman scattering	STaRS
Chang et al. prep	Scattered Lyα in CGM and IGM	Resonance Scattering Rayleigh Scattering	Lyα Blobs

Figure 1.2: A list of the research works I have participated in regarding radiative transfer in highly thick neutral media.

Chapter 2

3D Grid-Based Monte Carlo Code for Radiative Transfer through Raman and Rayleigh Scattering with Atomic Hydrogen

2.1   Introduction

Interaction of electromagnetic radiation with an atomic electron may be classified into Rayleigh and Raman scattering (e.g. Sakurai 1967). Rayleigh

scattering refers to the elastic process where the scattered photon has the
same wavelength as the incident one. Otherwise, we have Raman scattering
in which the initial and final electronic states differ so that the scattered
photon emerges with the energy difference, which is enforced by the law of
energy conservation. Raman spectroscopy is particularly useful in revealing
the complicated energy level structures of a molecule in chemistry.

In astrophysics, Nussbaumer et al. (1989) provided a pioneering dis-
cussion on Raman scattering with atomic hydrogen, introducing a new spec-
troscopic tool to diagnose gaseous emission nebulae including symbiotic stars
and active galactic nuclei. Relevant Raman scattering processes start with
a far UV photon more energetic than Lyα incident on an hydrogen atom
in the ground state and end with an outgoing photon with energy less than
that of Lyα leaving behind the hydrogen atom in the $2s$ state. They in-
troduced basic atomic physics of Rayleigh and Raman scattering illustrat-
ing the cross sections and presented a number of candidate far UV spectral
lines that may result in detectable Raman-scattered features (e.g., Saslow &
Mills 1969). One notable point is that the branching ratio of Raman and
Rayleigh scattering of far UV radiation near Lyβ is approximately 0.15 so
that most Lyβ photons are Rayleigh (or resonantly) scattered several times
before they are converted into Hα photons to escape from the thick neutral
region.

Schmid (1989) identified the broad emission features at 6825 Å and
7082 Å found in about half of symbiotic stars as Raman scattered features
of O VI 1032 and 1038 Å emission lines, respectively (Akras et al. 2019).
Symbiotic stars are wide binary systems composed of a hot white dwarf and
a mass-losing red giant. Hydrodynamical studies suggest that some fraction
of slow stellar wind is gravitationally captured to form an accretion disk (de
Val-Borro et al. 2017; Chen et al. 2017; Saladino et al. 2018), where O
VI$\lambda\lambda$1032 and 1038 are important coolants.

Considering very small Raman scattering cross sections $\sim 10^{-23}$ cm^2
for O VI$\lambda\lambda$1032 and 1038 doublet lines, the operation of Raman scattering
requires a special condition that a very thick neutral region is present in the
vicinity of a strong O VI emission region. This special condition is ideally
met in symbiotic stars, where a thick neutral region surrounding the giant
component is illuminated by strong far UV radiation originating from the
nebular region that may be identified with the accretion flow onto the hot
component.

Raman-scattered O VI features in symbiotic stars exhibit complicated
profiles with multiple peaks separated by $\sim 30 - 50$ km s^{-1} indicative of the
O VI emission regions with physical dimension of ~ 1 au (e.g. Shore et al.
2010; Heo & Lee 2015; Lee et al. 2019). Because Raman and Rayleigh
scattering sufficiently off resonance shares the same scattering phase func-

tion as Thomson scattering(Schmid 1995; Yoo et al. 2002; Chang et al.
 2017), strong linear polarization may develop in an anisotropic scattering
geometry. Harries & Howarth (1996) conducted spectropolarimetric observa-
tions of many symbiotic stars to show that Raman-scattered O VI features
are strongly polarized. They also found that most Raman-scattered O VI
features show polarization flip in the red wing part, where the polarization
develops nearly perpendicularly to the direction along which the main part
is polarized. Lee & Park (1999) proposed that the polarization flip is closely
associated with the bipolar structure of symbiotic stars (see also Heo et al.
 2016).

Raman scattering plays an interesting role of redistributing far UV ra-
diation near Lyβ and Lyγ into near Hα and Hβ, respectively. He II be-
ing a single electron ion with $Z = 2$, the transition to $n = 2$ from an
energy level from $n = 2k, k > 1$ gives rise to emission lines with wave-
lengths slightly shorter than those of H I Lyman series $k \to 1$, for which the
cross sections for Rayleigh and Raman scattering are conspicuously large.
van Groningen (1993) found Raman-scattered He II features near Hβ in the
symbiotic nova RR Telescopii. Péquignot et al. (1997) discovered the same
spectral feature in the young planetary nebula NGC 7027, which constitutes
the first discovery of a spectral feature formed through Raman scattering
with atomic hydrogen in planetary nebulae. Subsequently, Raman-scattered

He II at 6545 Å has been detected in several symbiotic stars (Birriel 2004;
Jung & Lee 2004; Sekeráš & Skopal 2015) and in the young planetary neb-
ulae NGC 6302, IC 5117, NGC 6790, NGC 6886, and NGC 6881 (Groves et
al. 2002; Lee et al 2001; Lee et al. 2006; Kang et al. 2009; Choi & Lee
2020).

It is particularly notable that the case B recombination theory allows
one to deduce the strengths of incident far UV He II lines (Storey & Hum-
mer 1995), yielding faithful estimates of Raman conversion efficiencies. This
is extremely useful in the measurement of H I content in symbiotic stars
and young planetary nebulae, which makes Raman spectroscopy a totally
new approach to probing the mass loss processes occurring in the late stage
of stellar evolution (Lee et al. 2006; Choi et al. 2020). Furthermore, Hα
and Hβ in symbiotic stars and young planetary nebulae often display fairly
extended wings that may indicate the presence of fast tenuous stellar wind
(e.g., Arrieta & Torres-Peimbert 2002). Broad wings around Balmer lines
may also arise via Raman scattering far-UV continuum around Lyman lines,
which requires further investigation (Lee 2000; Yoo et al. 2002; Chang et
al. 2018).

Additional examples include Raman scattering of C II$\lambda\lambda$1036 and 1037
forming optical features at 7023 Å and 7054 Å, which were reported in the
symbiotic nova V1016 Cygni by Schild & Schmid (1996). Dopita et al.

(2016) investigated the H II regions in the Orion Nebula (M42) and five H
II regions in the Large and Small Magellanic Clouds to discover Raman-
scattered features at 6565 Å and 6480 Å formed through Raman scattering
of O I $\lambda 1025.76$ and Si II $\lambda 1023.70$, respectively.

The Monte Carlo approach is an efficient numerical technique to de-
scribe radiative transfer in various regions having a dust component(e.g. Cel-
nikier & Lefévre 1974; Seon 2015) and a molecular component(e.g. Brinch
& Hogerheijde 2010). A similar approach has been applied to radiative
transfer of an electron scattering (e.g. Angel 1969; Seon et al. 1994). Lyα
deserves special attention being characterized by large scattering optical depth
(e.g. Eide et al. 2018; Seon & Kim 2020).

Schmid (1992) performed Monte-Carlo simulations to investigate the
formation of Raman-scattered O VI features in an expanding H I region with
an assumption that a given line photon has an invariant scattering cross
section as it propagates through the H I medium. Similar studies were pre-
sented by Lee & Lee (1997), who adopted a density matrix formalism to
determine the physical information of scattered radiation including polariza-
tion. Chang et al. (2015) investigated the formation of broad Balmer wings
near Hα and Hβ in the unification scheme of active galactic nuclei and pre-
sented quantitatively the asymmetry of the wings formed in neutral regions
with extremely high H I column density $\sim 10^{23}$ cm^{-2}.

In this paper, we introduce a new grid-based Monte Carlo code entitled
"Sejong Radiative Transfer for Rayleigh and Raman Scattering ($STaRS$), We
also present our test of the code by revisiting the formation of Balmer wings
and Raman O VI features through Raman scattering with atomic hydrogen.

2.2   Grid Based Monte Carlo Simulation

In this section, we describe 'STaRS' and discuss the basic atomic physics of
Rayleigh and Raman scattering with atomic hydrogen. Fig. 2.1 is a schematic
illustration of a few representative transitions pertaining to the two types of
scattering. Thus far, detected Raman-scattered features are limited to those
associated with the final de-excitation to $2s$ state. The second order time-
dependent perturbation theory is used to compute the scattering cross sec-
tions known as the Kramers-Heisenberg formula (e.g., Bethe & Salpeter
1957; Sakurai 1967; Saslow & Mills 1969).

In our grid based Monte Carlo code, we divide the region of interest
into a large number of small cubes or cells in the Cartesian coordinate sys-
tem, where each cell is characterized by uniform physical properties in the
three dimensional space. Here, the uniform physical properties include H
I number density $n_{\mathrm{HI},G}$ and the velocity $\mathbf{v}_G$. We assign the emissivity j_e
to each cell and generate an initial photon using $j_e(\lambda_i, x, y, z)$, where λ_i is
the wavelength of the initial photon. STaRS is mainly written in *Fortran*

with Message Passing Interface implemented for parallel computing. We also

adopt the shared memory technique by *intel MPI*.

Fig. 2.2 shows a flow chart for radiative transfer simulations using STaRS.

A simulation starts with the setup of the scattering geometry by assigning

to each cell appropriate physical conditions. Initial far UV photons are gen-

erated in accordance with our prescription of j_e. Each photon is tagged with

the information of the unit wavevector $\hat{\mathbf{k}}$, the position vector $\mathbf{r}$, the wave-

length λ, and the density matrix ρ composed of the Stokes parameters, I,

Q, U, and V. The free path d for next scattering position $\mathbf{r}'$ is computed

by transforming the scattering optical depth into the physical depth.

Decision is made whether the photon escapes from the region or is scat-

tered into another direction. If the next scattering position $\mathbf{r}'$ is outside the

scattering region, the photon is assumed to reach the observer as a far UV

photon. Otherwise, we generate a new photon using the scattering phase

function for an electric dipole process and determine the scattering type.

We assume that the region is transparent to Raman-scattered photons. The

scattered photon escapes from the scattering region if the scattering is Ra-

man. Otherwise, the Rayleigh scattered photon is regarded as an incident

photon propagating to a new scattering position. The procedure is repeated

until escape.

In Sec. 2.2.1 and 2.2.2, we provide more detailed descriptions on the
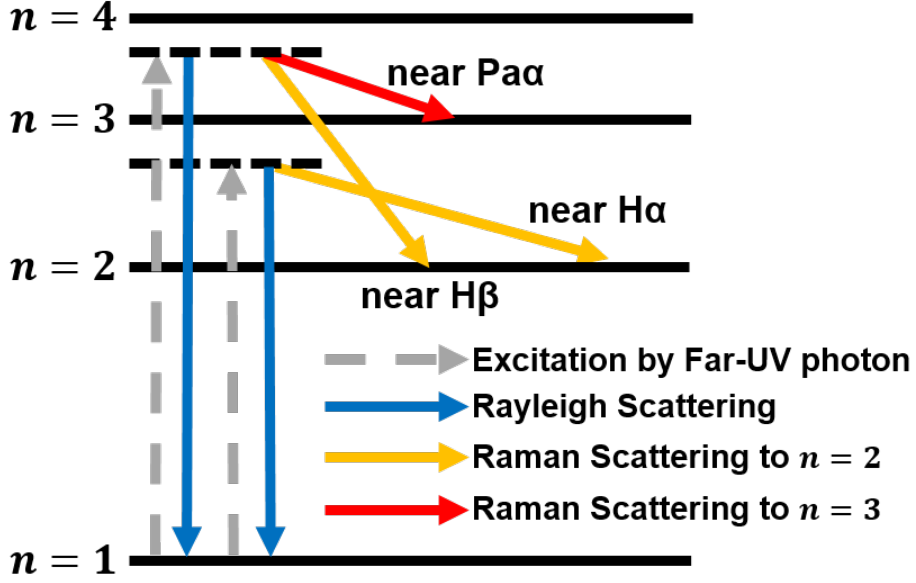
Figure 2.1: Schematic illustrations of energy levels and electronic transitions associated with Raman and Rayleigh scattering with a hydrogen atom of far UV electromagnetic radiation.

scattering geometry and generation of initial far UV photon prescribed by j_e. In Sec. 2.2.3, we describe the computation of a free path d. We discuss the basic properties of the scattered photons in Sec. 2.2.4.

2.2.1 Geometry : Scattering Region

The medium for radiative transfer through Raman and Rayleigh scattering corresponds to a thick H I region that is easily found in the slow stellar wind from a red giant (Lee & Lee 1997; Lee et al. 2019). No consideration on the thermal motion of neutral hydrogen is given because the variation of the cross section and the branching ratio in the scale of thermal speed is
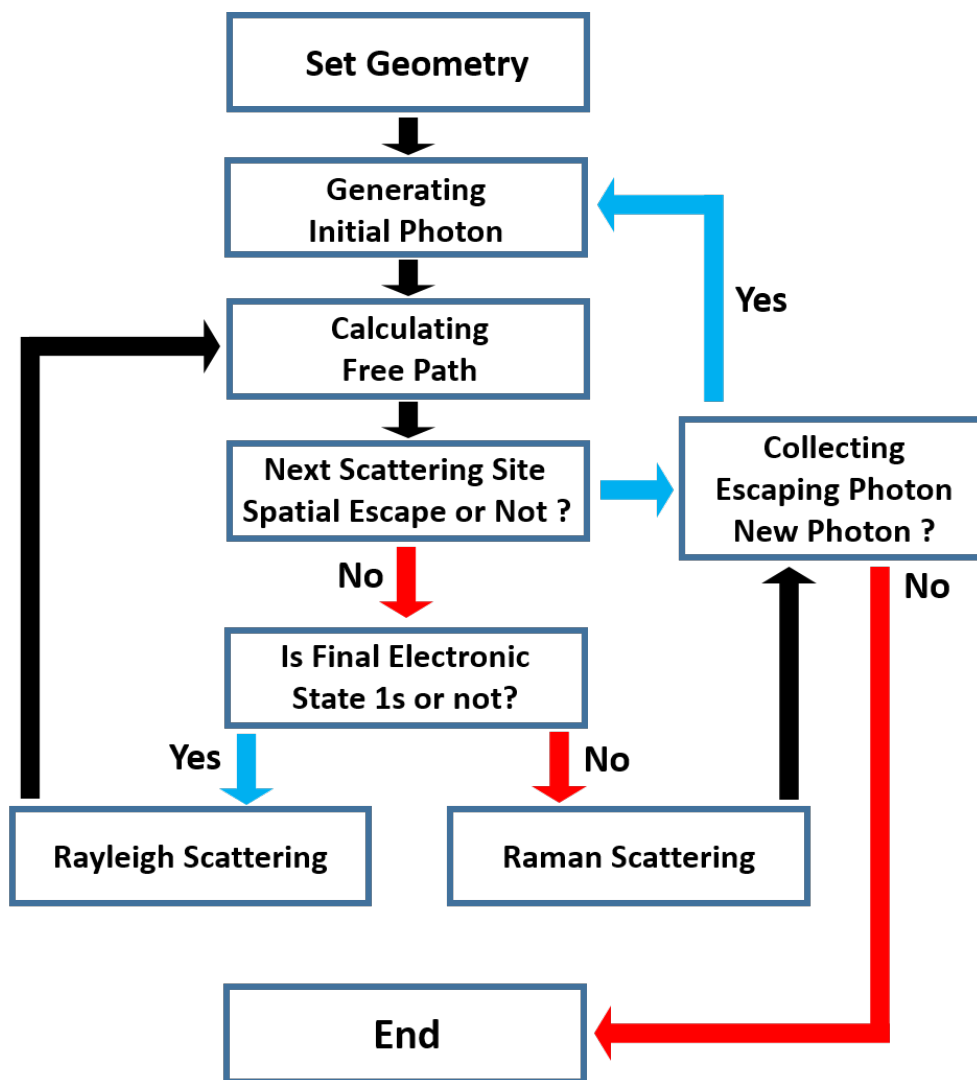
Figure 2.2: A flow chart of STaRS.

negligible (Chang et al. 2015, 2018).

In our simulation, we divide the scattering region into a large number of cells having a fixed size. Each cell is identified by a set of three indices (iX, iY, iZ) with iX, iY and iZ running from 1 to N_X, N_Y and N_Z. If we denote by X_{min} and X_{max} the range of x coordinates for the scattering region, the boundary of the iXth cell on the x axis is given by

$$X_G(iX) = X_{min} + \frac{X_{max} - X_{min}}{N_X}(iX - 1). \tag{2.1}$$

We also define $Y_G(iY)$ and $Z_G(iZ)$ in a similar way.

Therefore, for any point $P(x, y, z)$ in the cell identified with (iX, iY, iZ), we have

$$X_G(iX) < x < X_G(iX + 1) \tag{2.2}$$

$$Y_G(iY) < y < Y_G(iY + 1)$$

$$Z_G(iZ) < z < Z_G(iZ + 1).$$

Each cell is also identified by its center point, whose coordinates are given by the following relations

$$X_C(iX) = \frac{X_G(iX) + X_G(iX + 1)}{2} \tag{2.3}$$

$$Y_C(iY) = \frac{Y_G(iY) + Y_G(iY + 1)}{2}$$

$$Z_C(iZ) = \frac{Z_G(iZ) + Z_G(iZ + 1)}{2}.$$

2.2.2 Emission Source : Initial Photon

The operation of Raman scattering with atomic hydrogen requires the co-existence of a strong far UV source and a thick neutral region. In the case of symbiotic stars and young planetary nebulae, a strong far UV emission region is formed near an accreting white dwarf or a hot central star and a thick neutral region is also present in association with the mass loss of a giant star. In the simulation, the emissivity $j_e(\lambda, x, y, z)$ is prescribed as a function of wavelength and position. Regarding j_e as the normalized probability density function, we pick a wavelength λ_i and a starting position (x_i, y_i, z_i) of an initial photon in accordance with $j_e(\lambda, x, y, z)$.

We find the spatial index (iX, iY, iZ) from (x_i, y_i, z_i) to determine the cell that contains the starting position. For simplicity, we assume that the initial photon is completely unpolarized and that the unit wavevector of the initial photon is selected from an isotropic distribution. Thus, the initial unit wavevector $\hat{\mathbf{k}} = (k_x, k_y, k_z)$ is obtained using two uniform random numbers

r_1 and r_2 between 0 and 1 with the following prescription

$$
\begin{aligned}
\mu &= \cos\theta = 2r_1 - 1 \qquad\qquad\qquad (2.4)\\
\phi &= 2\pi r_2 \\
k_x &= \sin\theta \cos\phi \\
k_y &= \sin\theta \sin\phi \\
k_z &= \cos\theta.
\end{aligned}
$$

Because scattered radiation is polarized in an anisotropic geometry, it is important to carry the polarization information. The four Stokes parameters (I, Q, U, V) are necessary to describe the polarization state. An equivalent way is provided by considering the 2×2 density matrix defined by

$$
\rho = \begin{bmatrix} (I+Q)/2 & (U+iV)/2 \\ (U-iV)/2 & (I-Q)/2 \end{bmatrix}. \qquad\qquad (2.5)
$$

.

In our simulation, the Stokes parameter V, representing circular polarization, is always set to zero because no circular polarization develops from initially unpolarizd photons in electric dipole processes associated with Raman and Rayleigh scattering. Initially unpolarized photons are described by

a simple ρ is given by

$$\rho_{11} = 0.5 \tag{2.6}$$

$$\rho_{22} = 0.5$$

$$\rho_{12} = \rho_{21} = 0 \ .$$

The wavelength measured by an observer lying on the photon path is
kept in the simulation. We assume that the emitters are in random motion
and also subject to the bulk motion associated with the grid. If we let the
velocity of the emitter be $\mathbf{v}_{\mathrm{emit}}$ including bulk and random velocities, the
wavelength in the grid frame λ_g is given by

$$\lambda_g = \lambda_i \left(1 - \frac{\mathbf{v}_{\mathrm{emit}} \cdot \hat{\mathbf{k}}}{c} \right) \left(1 + \frac{\mathbf{v}_{\mathrm{G}} \cdot \hat{\mathbf{k}}}{c} \right), \tag{2.7}$$

where $\mathbf{v}_{\mathrm{G}}$ is the velocity of the cell (iX, iY, iZ).

2.2.3   Journey of Photon: Optical Depth and Free Path

The generation of an initial photon is followed by the estimate of the free
optical depth τ given by

$$\tau = -\ln r, \tag{2.8}$$

where r is a uniform random number between 0 and 1. We adopt the method
in Seon (2009) to compute the free path and the next scattering position in
grid-based geometry. In this section, we provide a brief description to com-
pute the free path and determine the scattering position.
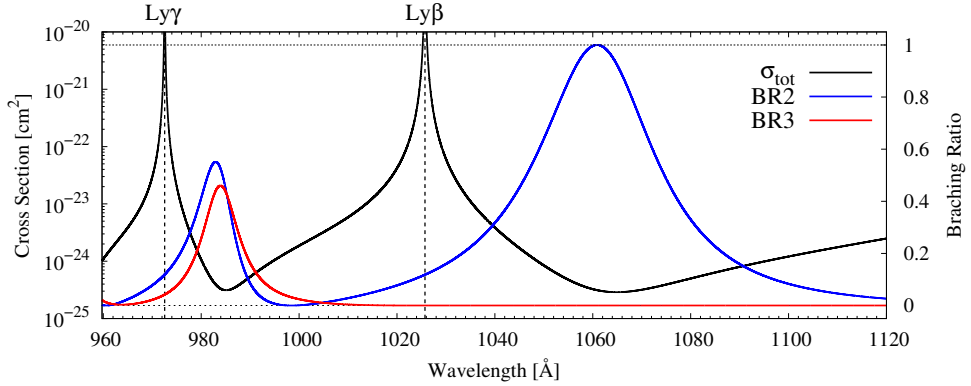
Figure 2.3: The total scattering cross section(black), the branching ratio to $n = 2$ (blue) and $n = 3$ (red) computed in Chang et al. (2015).

If the starting position $\mathbf{r}$ of the photon is in cell A, we measure the distance to the boundary of the cell d_A along the photon ray from the starting position. With d_A we define the scattering optical depth τ_A to the cell boundary by

$$\tau_A = \sigma_{\text{tot}}(\lambda_A) n_{\text{HI},A} d_A, \tag{2.9}$$

where λ_A is the wavelength in cell A. Fig. 2.3 shows the total scattering cross section $\sigma_{\text{tot}}(\lambda)$ as a function of wavelength. If $\tau_A > \tau$, then the next scattering position $\mathbf{r}'$ is found in cell A as follows

$$\mathbf{r}' = \mathbf{r} + \left(\frac{\tau}{\tau_A}\right) d_A \hat{\mathbf{k}}. \tag{2.10}$$

In the opposite case where $\tau_A < \tau$, the photon enters the neighboring cell B. In this case, the same problem is obtained if we regard the entry point $\mathbf{r}_e = \mathbf{r} + d_A \hat{\mathbf{k}}$ as the new starting point of the photon with a new free

optical path τ' reduced by τ_A, or

$$\tau' = \tau - \tau_A. \tag{2.11}$$

It should be noted that we are dealing with radiative transfer in a medium
in motion. Therefore, cell B may move with a velocity different from that of
cell A, in which case the photon wavelength along its propagation direction
may change on entering cell B from cell A. Denoting by $\mathbf{v}_{G,A}$ and $\mathbf{v}_{G,B}$ the
velocities of cells A and B, respectively, we have

$$\lambda_B = \lambda_A \left(1 - \frac{\mathbf{v}_{G,A} \cdot \hat{\mathbf{k}}}{c} \right) \left(1 + \frac{\mathbf{v}_{G,B} \cdot \hat{\mathbf{k}}}{c} \right). \tag{2.12}$$

Iterations from Eq. 2.9 are made with necessary updates $\mathbf{r} = \mathbf{r}_e$, $\tau = \tau'$,
and $\lambda_A = \lambda_B$ and new naming of cell B as cell A until we have $\tau_A > \tau$.
Fig. 2.4 shows a schematic illustration of this procedure. In cases when a
neighboring cell B may not exist and $\mathbf{r}$ is outside the geometry, the photon
is regarded as Rayleigh-escaped.

2.2.4   Rayleigh and Raman Scattering

Raman scattering with atomic hydrogen with the initial and final electronic
states being $1s$ and $2s$ shares the same the scattering phase function with
Rayleigh scattering with atomic hydrogen in $1s$ (e.g. Chang et al. 2015).
It is also notable that the scattering is sufficiently far from resonance, the
scattering phase function is the same as that of Thomson scattering. In this
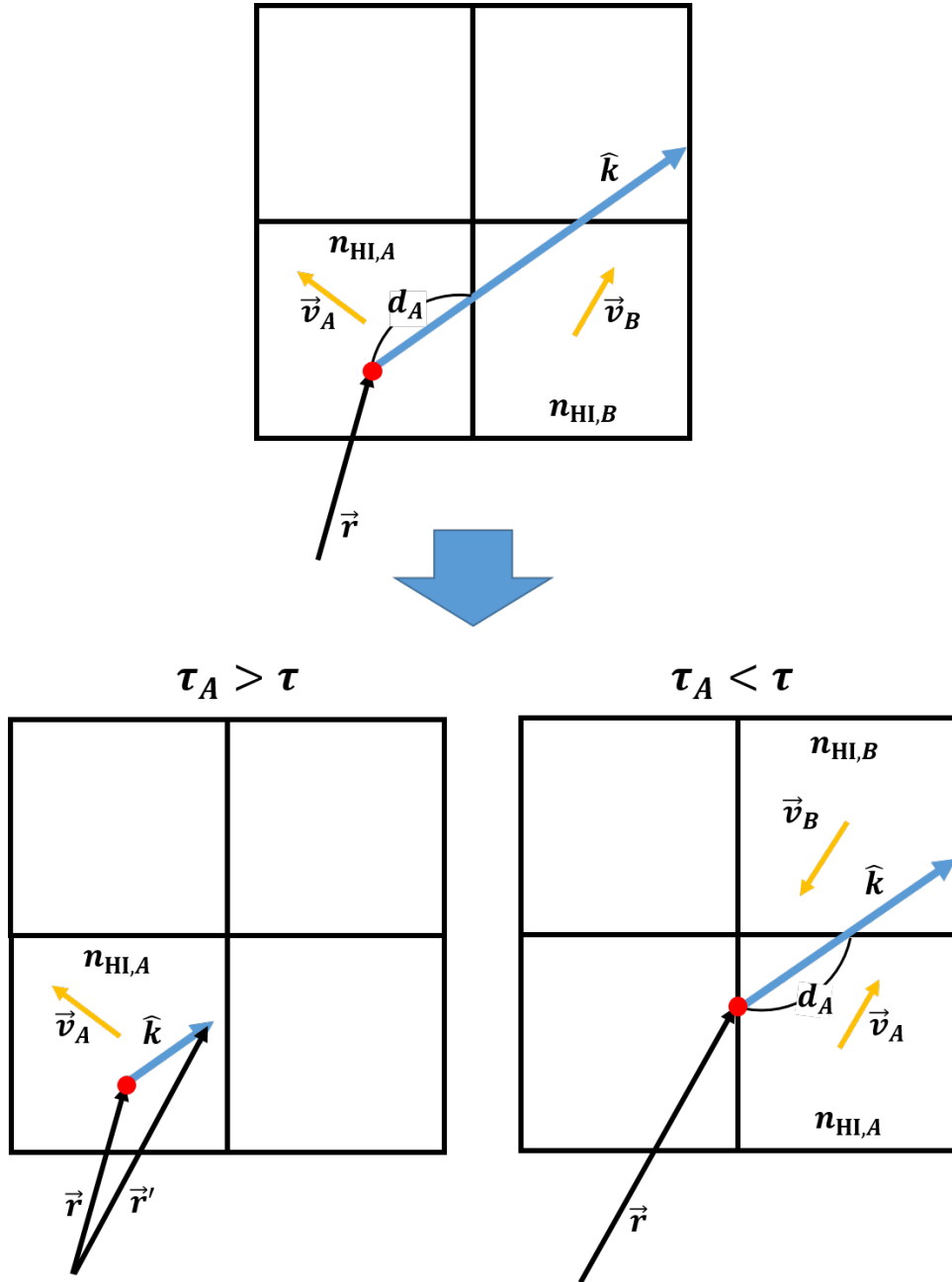
Figure 2.4: Schematic illustration of computing the next scattering position
in the grid-based simulation.

section, we describe the density matrix formalism with which the polariza-

tion and the unit wavevector $\hat{\mathbf{k}}'$ of the scattered photon is determined (Ahn

& Lee 2015; Chang et al. 2017). We also describe the wavelength conver-

sion and the line broadening associated with Raman scattering.

According to the density matrix formalism, the probability density of

the scattered wavevector $\hat{\mathbf{k}}' = (\sin\theta'\cos\phi', \sin\theta'\sin\phi', \cos\theta')$ is given by

$$I'(\hat{\mathbf{k}}') = \rho'_{11} + \rho'_{22}, \tag{2.13}$$

where ρ'_{ij} is defined by

$$\rho'_{ij} = \sum_{kl=1,2} (\hat{\epsilon}'_i \cdot \hat{\epsilon}_k)\rho_{kl}(\hat{\epsilon}_l \cdot \hat{\epsilon}_l'). \tag{2.14}$$

Here, $\hat{\epsilon}_{1,2}$ and $\hat{\epsilon}'_{1,2}$ are the polarization basis vector associated with $\hat{\mathbf{k}}$ and $\hat{\mathbf{k}}'$,

respectively. Specifically, $\hat{\epsilon}_1 = (-\sin\phi, \cos\phi, 0)$ and $\hat{\epsilon}_2 = (\cos\theta\cos\phi, \cos\theta\sin\phi, -\sin\theta)$

so that $\hat{\epsilon}_1$ represents polarization in the direction perpendicular to the plane

spanned by the photon wavevector and the $z-$axis.

The components of the density matrix associated with the scattered

radiation are related to those of incident radiation by

$$
\begin{aligned}
\rho'_{11} &= (\cos^2 \Delta\phi)\rho_{11} \\[6pt]
&\quad - (\cos\theta \sin 2\Delta\phi)\rho_{12} \\[6pt]
&\quad + (\sin^2 \Delta\phi \cos^2 \theta)\rho_{22} \\[6pt]
\rho'_{12} &= (\tfrac{1}{2}\cos\theta' \sin 2\Delta\phi)\rho_{11} \\[6pt]
&\quad + (\cos\theta \cos\theta' \cos 2\Delta\phi + \sin\theta \sin\theta' \cos\Delta\phi)\rho_{12} \\[6pt]
&\quad - \cos\theta(\sin\theta \sin\theta' \sin\Delta\phi + \tfrac{1}{2}\cos\theta \cos\theta' \sin 2\Delta\phi)\rho_{22} \\[6pt]
\rho'_{22} &= (\cos^2 \theta' \sin^2 \Delta\phi)\rho_{11} \\[6pt]
&\quad + \cos\theta'(2\sin\theta \sin\theta' \sin\Delta\phi + \cos\theta \cos\theta' \sin 2\Delta\phi)\rho_{12} \\[6pt]
&\quad + (\cos\theta \cos\theta' \cos\Delta\phi + \sin\theta \sin\theta')^2 \rho_{22},
\end{aligned}
\tag{2.15}
$$

where $\Delta\phi = \phi' - \phi$. In the code, a selection is made for $\hat{\mathbf{k}}'$ from an isotropic distribution to compute I'. A new random deviate r' is compared with I'. If $r' < I'$, then the selection of $\hat{\mathbf{k}}'$ is accepted. Otherwise, the process is iterated until the acceptance is obtained. The scattered photon now becomes a new incident photon propagating to a new scattering site. This is followed by necessary updates for the wavevector and the density matrix given by

$$
\hat{\mathbf{k}} = \hat{\mathbf{k}}' \tag{2.16}
$$

$$
\rho_{ij} = \rho'_{ij}.
$$

The scattering type is determined by the branching ratio. If an inci-

dent far UV photon is more energetic than Lyγ, the final states available

for Raman scattering include $2s$, $3s$ and $3d$ states. For photons near Lyγ,

the total cross section is given by

$$\sigma_{\text{tot}} = \sigma_{1s} + \sigma_{2s} + \sigma_{3s+3d}, \tag{2.17}$$

where σ_{1s}, σ_{2s}, and σ_{3s+3d} are the scattering cross sections corresponding

to the final states $1s$, $2s$, and $3s+3d$, respectively. Rayleigh branching ratio

$BR1$ is given by

$$BR1 = \frac{\sigma_{1s}}{\sigma_{\text{tot}}}. \tag{2.18}$$

In a similar way, Raman branching ratios corresponding to the final energy

levels $n = 2$ and 3 are

$$BR2 = \frac{\sigma_{2s}}{\sigma_{\text{tot}}}, \quad BR3 = \frac{\sigma_{3s+3d}}{\sigma_{\text{tot}}}, . \tag{2.19}$$

In Fig. 2.3, the blue and red solid lines represent $BR2$ and $BR3$, respec-

tively.

The energy difference between the incident and Raman-scattered pho-

tons is the same as that between the initial and final atomic states. This is

translated into the relation between the wavelengths λ and λ' of the Raman-

scattered and incident photons, respectively, which is given by

$$\frac{1}{\lambda} = \frac{1}{\lambda'} + \frac{1}{\lambda_{\text{res}}}, \tag{2.20}$$

where λ_{res} is the wavelength corresponding to the energy difference between

the initial and final states.

One very important aspect in Raman scattering can be found in the
conspicuous change in line width. Differentiating Eq. (2.20), we have

$$\frac{d\lambda'}{\lambda'} = \left(\frac{\lambda'}{\lambda}\right)\left(\frac{d\lambda}{\lambda}\right), \qquad (2.21)$$

from which we see immediately that the line width of Raman-scattered fea-
ture is broadened by the factor $(\lambda'/\lambda)^2$. For example, a typically observed
line width of Raman-scattered O VI at 6825 Åamounts to ~ 30 Å whereas
the far UV parent line O VI$\lambda\lambda 1032$ exhibits a line width ~ 1 Å in many
symbiotic stars.

Due to the line broadening effect, far UV radiation near Lyman series
of hydrogen will be considerably diluted and redistributed around Balmer
emission lines to appear as broad wings (e.g. Yoo et al. 2002; Chang et al.
2015, 2018). Another important consequence of the line broadening effect is
that the line profiles of Raman-scattered features mainly reflect the relative
motion between the far UV emitters and the neutral scatterers and quite
independent of the observer's line of sight (Heo et al. 2016; Choi et al.
2020).

2.3   Code Test

As a check of our code, we present our simulation results for two exem-
plary cases. The first example is a static spherical H I region surrounding a

far UV continuum source located at the center, in which Balmer wings are
formed through Raman scattering. Analytic solutions are available for this
case, against which our result obtained from STaRS is compared. The second
case is reproduction of the result of Lee & Lee (1997), who investigated
Raman scattering of O VI in symbiotic stars. In this case, the H I region is
an expanding spherical wind around the giant component. Schematic illustrations of the two cases are shown in Fig. 2.5.

2.3.1 Formation of Balmer Wings in a Static Spherical H I Region

The central point-like far UV source surrounded by a spherical H I region
with radius R is characterized by a flat continuum. The static neutral region is assumed to be of uniform H I density n_{HI}. We fix the radial column
density N_{HI} defined by

$$N_{\mathrm{HI}} = n_{\mathrm{HI}}R = 10^{23} \text{ cm}^{-2}, \qquad (2.22)$$

and vary the number of cells. We set $N_{xyz} = N_x = N_y = N_z$, so that the
total number of cells is given by N_{xyz}^3. We generate 10^7 photons for each
simulation. The initial photons are generated at the center of the H I sphere
in accordance with the emisivity j_e given by the three dimensional Dirac
delta function

$$j_e(\lambda, x, y, z) = \frac{\lambda}{\lambda_{max} - \lambda_{min}} \delta^{(3)}(\mathbf{r}), \qquad (2.23)$$

where λ_{max} and λ_{min} are the maximum and minmum wavelengths of initial

photons.

Fig. 2.6 shows optical spectra formed through Raman scattering for the

cases of $N_{xyz} = 3, 10$ and 100. The vertical axis shows the Raman conver-

sion efficiency (RCE) defined as the number ratio per unit wavelength of

incident far UV photons and Raman-scattered optical photons. The left and

right panels show Balmer wings formed through Raman scattering around

Hα and Hβ, respectively. The solid lines represent the analytic solutions and

open circles show simulation results obtained using STaRS. The analytic so-

lutions are obtained from the non-grid based simulation in Chang et al.

(2015, 2018).

Far from the line centers, the simulation results for $N_{xyz} = 3$ are slightly

higher than the analytic solutions. Other than this, the agreement is fairly

good, indicating little dependence on N_{xyz} in the case of a static H I re-

gion. The volume of the H I region with $N_{xyz} = 3$ is larger than the sphere

with the radius R as the H I density associated with a cell is determined

by the central position (X_C, Y_C, Z_C) of the cell. When $(X_C^2 + Y_C^2 + Z_C^2)^{1/2}$

is smaller than R, the H I density of the cell is assigned to be n_{HI}. Other-

wise, the density is assigned to be zero. The number ratio between Raman

scattered photons near Hα and the total initial photons near Lyβ is 20.77

% for the analytic solution, whereas the simulations give 21.17, 20.91, and

20.77 % for $N_{xyz} = 3$, 10, and 100, respectively.

In Fig. 2.7, we present the polarimetric data of Raman scattered Hα projected to the celestial sphere. The surface brightness, the degree of polarization p, and the direction of polarization are shown in the left, middle and the right panels, respectively. Here, in terms of the Stokes parameters, the degree of polarization p and the position angle ϕ_p are given by

$$p = \frac{\sqrt{Q^2 + U^2}}{I}, \quad \phi_p = \frac{1}{2} \tan^{-1}\left(\frac{U}{Q}\right). \tag{2.24}$$

In the left panels, the surface brightness is shown in logarithmic scale. With our choice of a rather large value of N_{HI}, a considerable fraction of Raman-scattered photons are formed near the source, which leads to excellent agreement between the analytic results and those obtained using STaRS. One may notice increase in smoothness of the surface brightness as N_{xyz} increases. It is also noticeable that p becomes large with increasing distance from the center. The concentric polarization pattern reflects the spherically symmetric scattering geometry. In this particular case, $N_{xyz} > 10$ appears to be sufficient to describe the the analytic result of the static medium.

2.3.2 Raman Scattering of O VI in Expanding H I Region

Lee & Lee (1997) presented their basic study of line formation of Raman O VI in a symbiotic star consisting of a white dwarf and a mass losing giant. The O VI emission region near the white dwarf component was assumed to
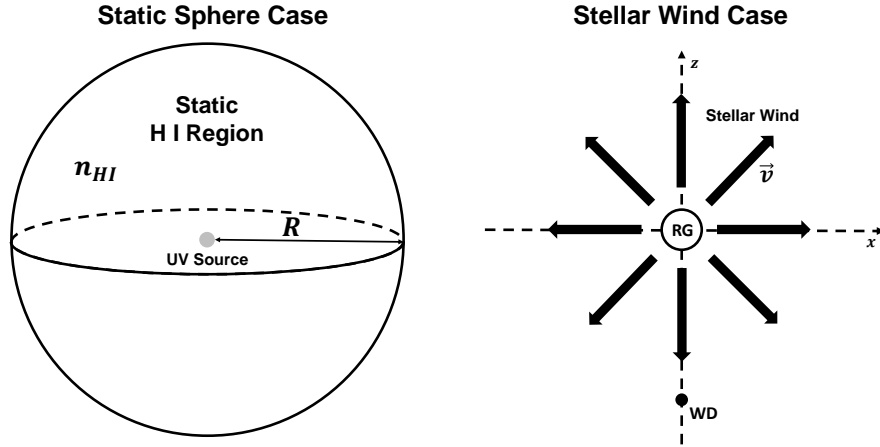
Figure 2.5: Schematic illustrations of two cases to test the code.
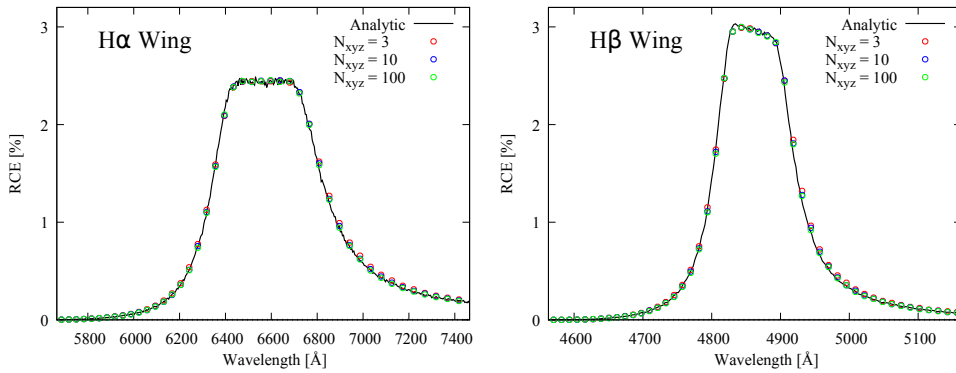
Figure 2.6: Raman conversion efficiency of Hα (left panel) and Hβ (right panel) broad wings of the static spherical case. The black solid lines are the spectra by the analytic method. The x axis is the wavelength. The red, blue, and green open circles are the spectra by STaRS for $N_{xyz} = 3$, 10, and 100.

be a point source broadened thermally with $T = 10^4 \, \text{K}$. For simplicity, the

slow stellar wind from the red giant component is assumed to be entirely

neutral ignoring the photoionization by the white dwarf. The orbital sep-

aration is $10R_*$ of which R_* is the radius of the red giant. The positions

of the white dwarf and the red giant are $(0, 0, 10R_*)$ and $(0, 0, 0)$, respec-

tively. The initial photons are generated at the position of the white dwarf

according to the emissivity j_e given by

$$j_e(\lambda, x, y, z) = \tag{2.25}$$

$$\frac{1}{\sigma_{th}\sqrt{2\pi}} \exp\left[\frac{(\lambda - \lambda_{1032})^2}{2\sigma_{th}^2}\right] \delta^{(3)}(x, y, z - 10R_*)$$

where λ_{1032} is the center wavelength of O VI λ 1032 and $\sigma_{th} \sim 0.008$ Å is

the thermal width of O VI λ 1032 with $T = 10^4 K$.

The velocity $\mathbf{v}(\mathbf{r})$ and H I number density $n(\mathbf{r})$ are the functions of the

distance from the red giant $r = |\mathbf{r}|$ are given by

$$\mathbf{v}(\mathbf{r}) = v_\infty(1 - R_*/r)\frac{\mathbf{r}}{r} \tag{2.26}$$

$$n(\mathbf{r}) = n_0(R_*/r)^2(1 - R_*/r)^{-1},$$

where n_0 is the characteristic number density defined in Eq. 2.11 of Lee &

Lee (1997) and v_∞ is the terminal velocity. As a second code test case, we

revisit Raman O VI formation illustrated in Figs. 1 and 6 of Lee & Lee

(1997). Fixing $v_\infty = 20 \, \text{km s}^{-1}$, we consider the three values of $\tau_0 = 0.5$, 1,

and 10, where $\tau_0 = n_0 R_* \sigma_{\text{tot}}$. We generate 10^9 photons for each simulation.

Fig. 2.8 shows the spectra and the Stokes parameter $P = Q/I$ for Raman scattered O VI at 6825 Å. It should be noted that the integrated U vanishes due to the axial symmetry about the z axis. Therefore, the signed ratio Q/I represents the degree and direction of polarization, where a positive and a negative Q correspond to the polarization in direction perpendicular and parallel to the z axis, respectively. The observer's line of sight lies in x-y plane. Noting that it is perpendicular to the symmetry axis, maxium polarization can be developed along this direction or the symmetry z−axis. We collecte the photons escaping toward the observer. The fraction of the collected Raman photons near 6825 Å is 0.11, 0.21, and 1.82 % for $\tau_0 = 0.5$, 1, and 10, respectively.

The line profiles obtained using STaRS differ slightly from those Lee & Lee (1997) presented. In particular, the red peaks obtained from STaRS are more enhanced than those presented by Lee & Lee (1997), which is attributed to the geometrical truncation adopted by them. The difference is in the range of 10-15 per cent with respect to the red peak. We find that the agreement gets better where the full range of the scattering region is taken into account. In the bottom panels, we find overall agreement in the polarization behaviors. The noisy features with $\Delta V > 200\,\mathrm{km\,s^{-1}}$ are attributed to the small number statistics of collected photons. Blue photons are scattered mostly in the compact and dense region between the red giant and

white dwarf, resulting in development of strong polarization in the direction perpendicular to the z axis. In contrast, red photons are scattered mainly in a quite extended region near the red giant, leading to weak polarization and enhanced line flux.

Fair agreement shown in Fig. 2.6 and 2.8 demonstrates that STaRS has been well-tested. Furthermore, as illustrated in Fig. 2.7, STaRS is capable of study of radiative transfer for spectropolarimetric imaging observations.

2.4   Summary

We have developed a 3D grid-based Monte Carlo code 'STaRS' for radiative transfer through Raman and Rayleigh scattering, which can be mainly used to investigate line formation of Raman-scattered features in a thick neutral region illuminated by a strong far UV emission source. Favorable conditions for Raman scattering with atomic hydrogen are easily met in symbiotic stars, young planetary nebulae and active galactic nuclei. Through a couple of tests, we have successfully demonstrated that 'STaRS' is a flexible code to deal with radiative transfer in a thick neutral media yielding multidimensional spectropolarimetric and imaging data. 'STaRS' is easily accessed in Github 'https://github.com/csj607/STaRS'.
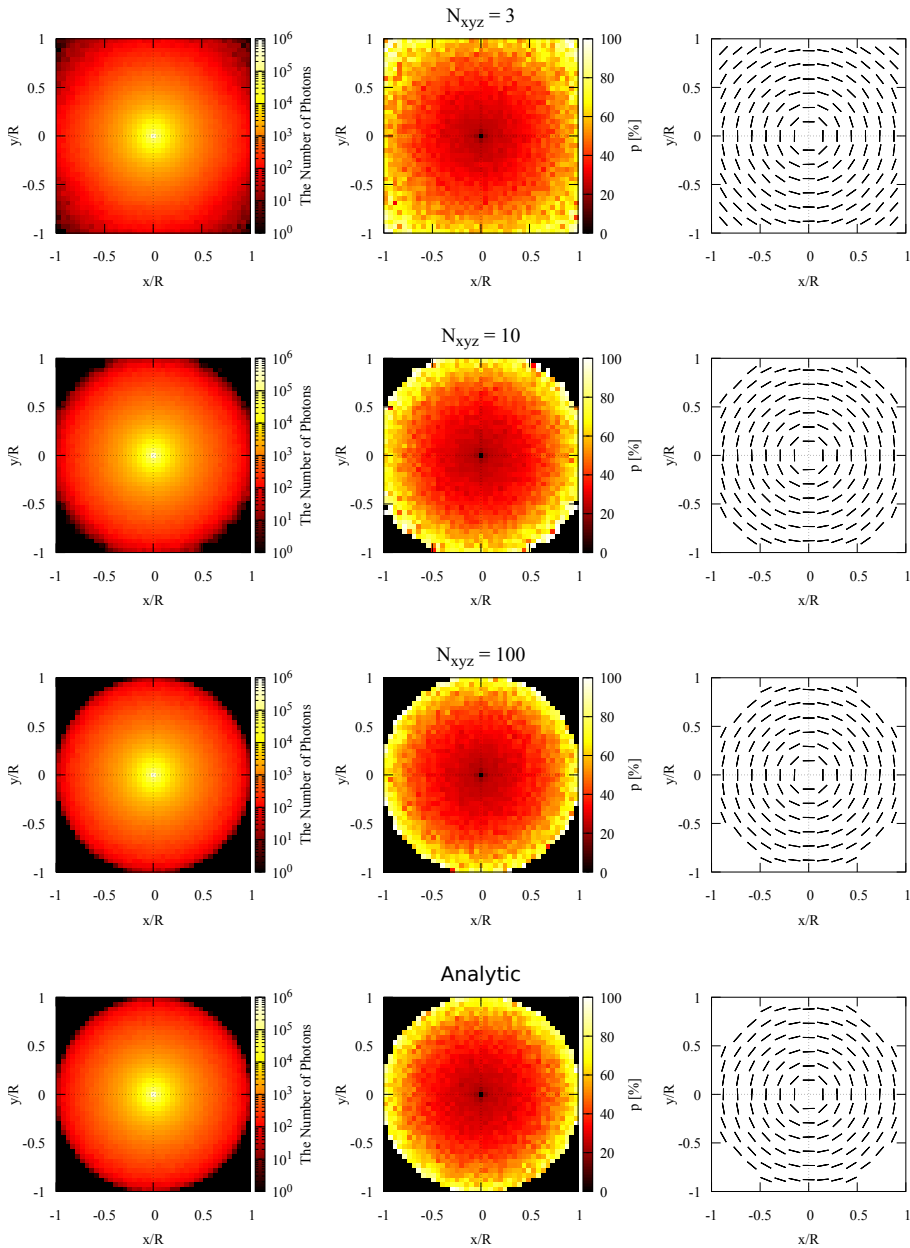
Figure 2.7: The surface brightness (left), the degree of polarization (center), and the direction of polarization (right) of the projected Hα photons. The panels in the first, second, and third rows represent the results obtained using STaRS for $N_{xyz} = 3$, 10, and 100. The bottom panels represent the result obtained using an analytic method.
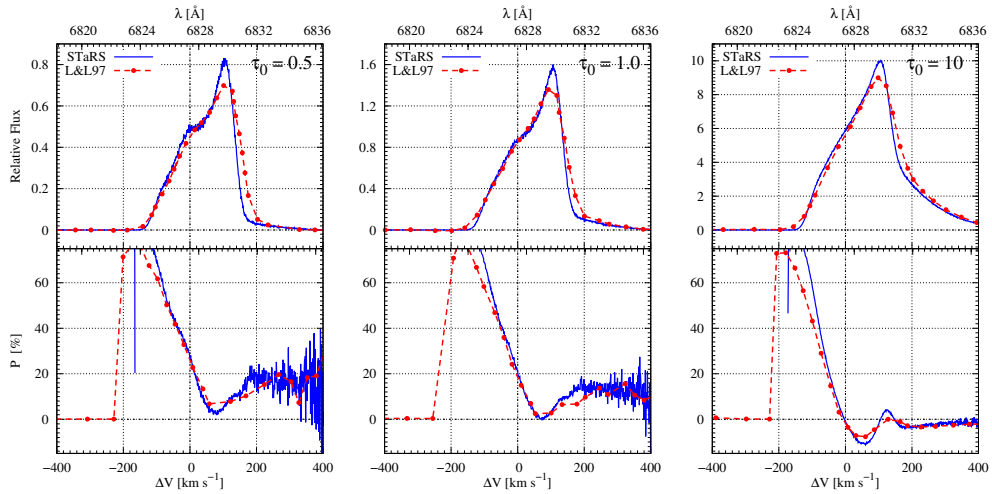
Figure 2.8: Line formation of Raman O VI 6825 features in an expanding
H I region. The blue solid lines are computed by 'STaRS'. The red dashed
lines are the results of Fig. 6 in Lee & Lee (1997).

Chapter 3

Broad Wings around Hα and Hβ in the Two S-Type Symbiotic Stars Z Andromedae and AG Draconis

3.1 Introduction

Symbiotic stars are wide binary systems of a hot white dwarf and a mass losing giant (e.g. Kenyon 2009). They are important objects for studying the mass loss and mass transfer processes. Their UV-optical spectra are characterized by prominent emission lines with a large range of ionization encom-

passing C II and O VI. Symbiotic activities including outbursts and bipolar outflows are attributed to the gravitational capture of some fraction of slow stellar wind from the giant component by the hot white dwarf (e.g., Skopal 2008; Mikołajewska 2012).

According to IR spectra, symbiotic stars are classified into 'S' type and 'D' type. 'D' type symbiotic stars exhibit an IR excess indicative of the presence of a warm dust component with $T_D \sim 10^3$ K (e.g. Angeloni et al. 2010), whereas no such features are found in the spectra of 'S' type symbiotics. The orbital properties also differ greatly between these two types of symbiotics. The orbital periods are found to be of order several hundred days for 'S' type symbiotics, implying that the binary separation is about several AU (e.g. Mikołajewska 2012). However, the orbital periods of D type symbiotic stars are notoriously difficult to measure and only poorly known (e.g. Schild & Schmid 1996; Schmid 2000).

Symbiotic stars show unique spectroscopic features at around 6825 Å and 7082 Å, which are formed through Raman scattering of far UV resonance doublet O VI $\lambda\lambda$1032 and 1038. Schmid (1989) proposed that an O VI λ1032 photon is incident on a hydrogen atom in the ground state, which subsequently de-excites into $2s$ state emitting an optical photon at 6825 Å. The 7082 feature is formed in a similar way when O VI λ1038 photons are Raman scattered by neutral hydrogen atoms. The cross section for

O VI is of order 10^{-22} cm^2 requiring the presence of a thick H I component in the vicinity of a hot emission nebula.

High resolution spectroscopy shows that most symbiotic stars exhibit broad wings around Hα, which often extend to several thousand km s^{-1} (e.g., Van Winckel et al. 1993; Ivison et al. 1994; Skopal 2006; Selvelli & Bonifacio 2000). Nussbaumer et al. (1989) proposed that Raman scattering by atomic hydrogen can give rise to broad wings around Balmer emission lines. Lee (2000) showed that the broad wings of many symbiotic stars are consistent with a profile proportional to $\Delta\lambda^{-2}$ that is expected of Raman scattering wings. Similar results for broad Hα wings in a number of planetary nebulae and symbiotic stars were obtained by Arrieta & Torres-Peimbert (2003). These objects share the common property that a thick neutral component is present in the vicinity of a hot ionizing source.

Broad wings can also be formed through Thomson scattering, where emission line photons are scattered off of fast moving electrons to get broadened (e.g. Sekerá (š & Skopal 2012). In particular, Sekerá (š & Skopal (2012) performed profile analyses of broad wings of O VI and He II emission lines and estimated the Thomson scattering optical depth and electron temperature of the symbiotic stars, AG Draconis, Z Andromedae and V1016 Cygni.

Z And is regarded as a prototypical symbiotic star with an M-type gi-

ant whose mass is ~ 2 M$_\odot$ (e.g. Mürset & Schmid 1999). The mass of the white dwarf has been reported to be 0.75 M$_\odot$. The orbital period is not accurately known and presumed to be in the range 759.0 ± 1.9 days (e.g., Fekel et al. 2000). Having a K-type giant component, AG Dra is known to be a yellow symbiotic star (e.g. Mürset & Schmid 1999). It has been reported that the masses of the white dwarf and the giant components of AG Dra are 1 M$_\odot$ and 0.5 M$_\odot$, respectively. The known binary orbital period of 550 days implies that the binary separation is ~ 0.3 AU (e.g., Fekel et al. 2000).

In this paper, we present broad wings around Hα and Hβ from high resolution spectra of the 'S' type symbiotic stars Z And and AG Dra obtained with the ESPaDOnS and the 3.6 m *Canada-France-Hawaii Telescope* (CFHT). The observed wing profiles are compared to the theoretical model wings obtained with a Monte Carlo technique. We propose that Raman scattering is consistent with the two wing features whereas other wing formation mechanisms present difficulty in reconciling with the observation.

3.2 Spectroscopic Observation and Broad Balmer Wings

In Fig. 3.1, we show the spectra around Hα and Hβ emission lines of Z And and AG Dra obtained with the 3.6 m *CFHT* and ESPaDOnS on the nights
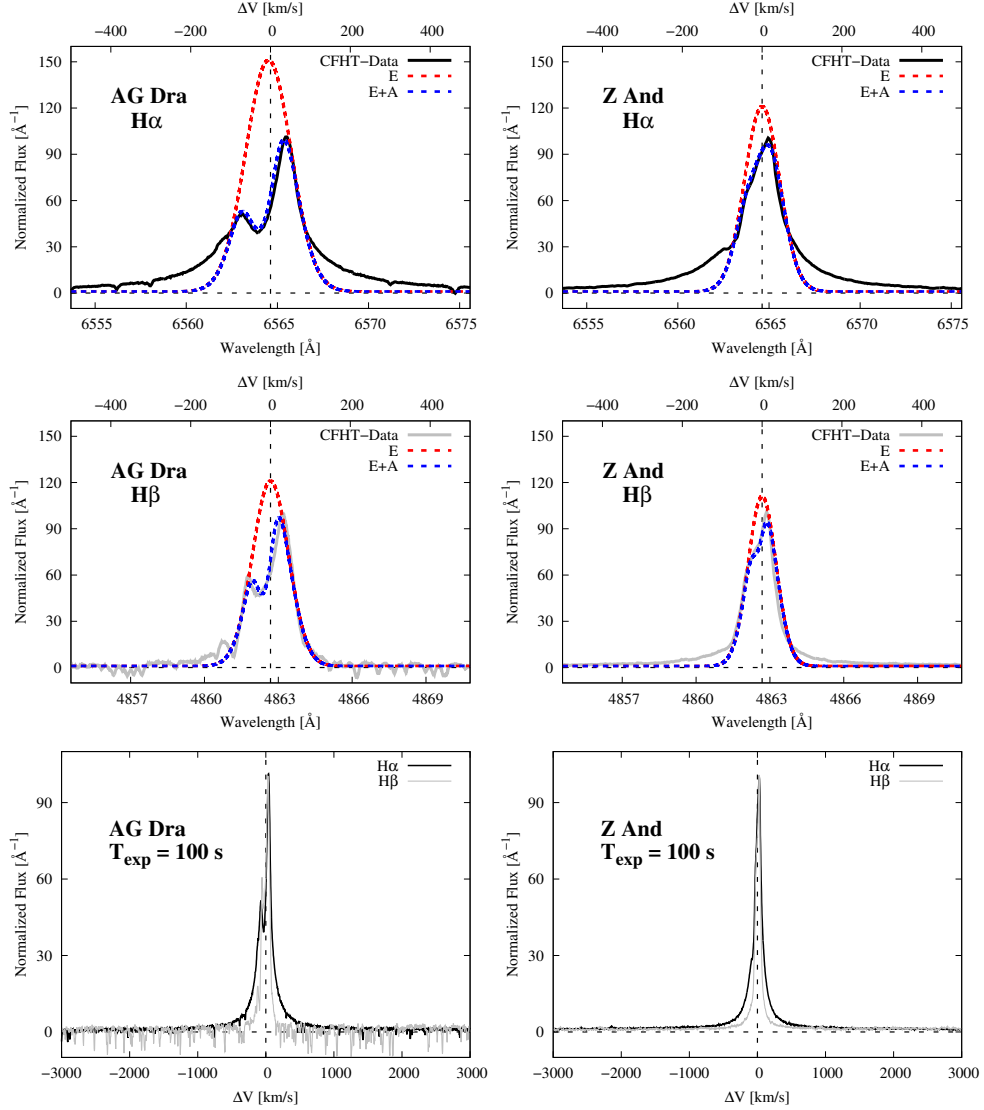
Figure 3.1: Spectra around Hα and Hβ obtained with the high resolution spectrograph ESPaDOnS and 3.6 m *CFHT* of the two 'S' type symbiotic stars AG Draconis (left panel) and Z And (right panel). The upper and lower horizontal axes show the Doppler factor from line center in units of km s^{-1} and the wavelength in units of Å, respectively. The top and middle panels show profiles of Hα and Hβ fitted with a single Gaussian emission component and an emission component with a Gaussian absorption, G_E and G_{EA}. The black dashed lines are x and y axes. In the bottom panels, we overplot Hα (black solid line) and Hβ (grey solid line) in the Doppler factor space.

of 2014 August 18 and September 6, respectively. The two symbiotic stars were observed in the "object only" spectroscopic mode with the spectral resolution of 81,000. The exposure time was 100 s. The standard procedure has been followed to reduce the observational data.

In the top and middle panels, the lower horizontal axis shows the wavelength λ and the upper horizontal axis shows the Doppler factor ΔV defined as

$$\Delta V = \left(\frac{\lambda - \lambda_c}{\lambda_c} \right) c, \tag{3.1}$$

where λ_c is the line center wavelength of either Hα or Hβ and c is the speed of light. The weak underlying continuum is set to be a unit value and the profiles are normalized so that the two emission lines have the same peak value of 101. In Appendix A, we discuss the normalization of continuum fluxes and profiles in this work and conversion into physical units.

In the bottom panels, we overplot the Hα and Hβ profiles in the Doppler factor space in order for quantitative comparisons of the profiles. It is found that the Hα profiles appear much broader than the Hβ counterparts in these two symbiotic stars. Furthermore, Hα wings are more conspicuous than Hβ wings even when they are compared in the Doppler factor space. Hereafter, for ease of profile comparisons, we describe the profiles in the Doppler factor space.

The top and middle panels of Fig. 3.1 show our fit to Hα and Hβ using

45

two functions, G_E and G_{EA} defined as follows

$$
\begin{aligned}
G_E &= A_E \exp\left(-\frac{\Delta V^2}{2\sigma_E^2}\right) \\
\tau_A &= \frac{\tau_{A0}}{\sqrt{2\pi\sigma_A^2}} \exp\left[-\frac{(\Delta V - \Delta V_A)^2}{2\sigma_A^2}\right] \\
G_{EA} &= G_E \exp(-\tau_A).
\end{aligned}
$$

$$(3.2)$$

Here, G_E represents a single Gaussian emission profile characterized by the peak A_E and width σ_E, whereas G_A represents an absorption component shifted by ΔV_A and characterized by the peak optical depth τ_{A0} and the width σ_A. The function G_{EA} describes a single Gaussian emission superimposed by a single Gaussian absorption.

Table 3.2 shows the values of the parameters that characterize G_E and G_A for Hα and Hβ of the two objects. The peaks and widths of Hα emission are larger than those of Hβ emission, and also the same behavior is found for the Hα and Hβ absorption features. In the case of AG Dra, $\Delta V_A = -22$ km s^{-1} for both Hα and Hβ and $\Delta V_A = -15$ km s^{-1} for Z And. The effect of the absorption profiles of Hα and Hβ can be seen in the shoulder parts near $\Delta V \sim 100$ km s^{-1}. It should be noted that Balmer profiles of AG Dra and Z And differ significantly even in the core parts. However, in this work, we focus on the wing profiles of these two symbiotic stars.

Table 3.1: The parameters for core profiles of Hα and Hβ in Eq. (3.2)

Object	Line	A_E	σ_E (km s^{-1})	τ_{A0}	σ_A (km s^{-1})	ΔV_A (km s^{-1})
AG Dra	Hα	150	57	90	30	-22
AG Dra	Hβ	120	45	37	18	-22
Z And	Hα	120	44	20	27	-15
Z And	Hβ	110	35	10	13	-15

3.3 Wing Formation and the Monte Carlo Approach

3.3.1 Atomic Physics of Wing Formation

In this work, we consider two physical mechanisms that may be responsible

for formation of broad wings around Balmer emission lines. One is Thomson

scattering by free electrons and the other is Raman scattering by atomic

hydrogen. In terms of the classical electron radius $r_e = e^2/(m_e c^2) = 2.82 \times$

10^{-13} cm, the Thomson scattering cross section is given as

$$\sigma_{Th} = \frac{8\pi}{3} r_e^2 = 0.665 \times 10^{-24} \text{ cm}^2.$$ (3.3)

The cross section σ_{Th} is independent of the incident photon wavelength,

which implies that line photons escape from the scattering region through

spatial diffusion in a way completely analogous to a random walk process.

Thomson scattering is regarded as the low energy limit of Compton

scattering, in which case there is fractional energy exchange $\Delta E/E \sim h\nu/(m_e c^2)$.

For a representative optical photon with $h\nu = 2$ eV it amounts to $\Delta E/E \sim$

4×10^{-6}. This is equivalent to a Doppler factor $\Delta V \sim 1.2$ km s^{-1} or a red-shift in the amount of 0.024 Å for Hα (e.g. Hummer & Mihalas 1967).

Hummer (1962) presented the redistribution function in frequency space taking into account the non-coherency of Compton scattering. However, this effect provides almost negligible contribution to broad Balmer wings having widths in excess of 10^3 km s^{-1}. In view of this fact, previous works by Laor (2006) and Kim et al. (2007) took into consideration only thermal motions of free electrons in order to to compute wing profiles of Thomson scattering.

In this work, we also consider only thermal motions of free electron in simulating Thomson scattering wings. In the rest frame of a free electron, Thomson scattering is described as an elastic scattering process where an incident photon changes its direction without any frequency shift. In the observer's frame, the scattered photon acquires a Doppler shift corresponding to the electron velocity component along the difference in wavevectors of incident and scattered radiation.

We may expect that the width and strength of Thomson wings are mainly determined by the Thomson optical depth $\tau_{Th} = N_e \sigma_{Th}$ and the electron temperature T_e, where N_e is the electron column density given by the product of the electron density n_e and the characteristic length associated with the scattering region. The electron temperature representative of an emission nebula is $\sim 10^4$ K (Osterbrock & Ferland 2006), for which the

electron thermal velocity is

$$v_{th} = \sqrt{\frac{kT_e}{m_e}} = 389 \ T_4^{1/2} \ \text{km s}^{-1}, \tag{3.4}$$

where $T_4 = T_e/10^4$ K. In terms of wavelength shift around Hα, this amounts

to $\Delta\lambda_{th} = v_{th}\lambda_{H\alpha}/c = 8.5$ Å.

Broad wing features can develop around any spectral lines through Thom-
son scattering due to wavelength independence of the cross section. In con-
strast, Raman scattering by atomic hydrogen can produce broad wings around
hydrogen emission lines except for Lyman lines, because the cross section is
sharply peaked around hydrogen emission line centers. Raman scattering is
a generic term describing an inelastic scattering process involving an inci-
dent photon and an electron bound to an atom or a molecule. In particular,
far UV radiation near Lyβ and $Ly\gamma$ may be scattered by a hydrogen atom
in the ground $1s$ state, which de-excites finally into the $2s$ state with the
emission of an optical photon around Hα and Hβ. The energy conservation
requires the relation between wavelengths λ_i and λ_o of the incident and scat-
tered radiation, respectively, given by

$$\lambda_o^{-1} = \lambda_i^{-1} - \lambda_{Ly\alpha}^{-1}, \tag{3.5}$$

where $\lambda_{Ly\alpha}$ is the wavelength of Lyα. A wavelength variation for the incident

radiation $\Delta\lambda_i$ corresponds to a much broader wavelength range $\Delta\lambda_o$ shown

as

$$\Delta\lambda_o = \left(\frac{\lambda_o}{\lambda_i}\right)^2 \Delta\lambda_i, \tag{3.6}$$

from which we recognize the broadening factors $\lambda_o/\lambda_i \simeq 6.4$ for Hα and $\lambda_o/\lambda_i \simeq 5.0$ for Hβ.

The interaction of a photon and an electron is described by the second order perturbation theory, introduced in many textbooks on quantum mechanics including Sakurai (1967) and Bethe & Salpeter (1957). The cross section for Raman scattering is known as the Kramers-Heisenberg formula

$$\begin{aligned}
\frac{d\sigma}{d\Omega} &= r_e^2 \left(\frac{\omega'}{\omega}\right) \left| \frac{1}{m_e} \sum_I \left(\frac{(\mathbf{p} \cdot \epsilon^{(\alpha')})_{BI}(\mathbf{p} \cdot \epsilon^{(\alpha)})_{IA}}{E_I - E_A - \hbar\omega} \right.\right. \\
&+ \left.\left. \frac{(\mathbf{p} \cdot \epsilon^{(\alpha)})_{BI}(\mathbf{p} \cdot \epsilon^{(\alpha')})_{IA}}{E_I - E_A + \hbar\omega'} \right) \right|^2,
\end{aligned} \tag{3.7}$$

where $\epsilon^{(\alpha)}$ and $\epsilon^{(\alpha')}$ are polarization vectors associated with the incident and scattered photons, respectively (e.g. Saslow & Mills 1969; Chang et al. 2015). Here, the initial state $A = 1s$, the final state $B = 2s$ and the intermediate state I covers all bound np states and continuum $n'p$ states.

The Wigner-Eckart theorem asserts that one can decompose the matrix elements into the radial part and the angular part, where the angular part is averaged over unpolarized incident radiation and summed over all possible polarization states to yield the Rayleigh scattering phase function

$$< |\epsilon^{(\alpha)} \cdot \epsilon^{(\alpha')}| > = \frac{8\pi}{3}. \tag{3.8}$$

The matrix element associated with the momentum operator p is simply related to the oscillator strength by

$$f_{nn'} = \frac{2}{m_e \hbar \omega_{nn'}} |p_{nn'}|^2,\tag{3.9}$$

and the Kramers-Heisenberg formula can be rearranged in terms of the oscillator strengths (e.g., Nussbaumer et al. 1989).

As far as the broad wings around Hα are concerned, the wavelength range of interest lies in off-resonance regime sufficiently far from the Lyβ line center compared to the thermal width. Near Lyβ, the cross section is dominantly contributed by the $3p$ term, in which case the cross section is excellently approximated by a Lorentzian function. According to Lee (2013),

$$\sigma^{\text{Ram}}(\omega) \simeq \frac{5}{128} \sigma_{Th} \left(\frac{\omega_{32}}{\omega - \omega_{31}} \right) f_{13} f_{2s,3p},\tag{3.10}$$

where the oscillator strengths are

$$f_{13} = 0.0791, \quad f_{2s,3p} = 0.4349\tag{3.11}$$

(see e.g. Bethe & Salpeter 1957).

In Fig. 3.2, we present the total cross section near Lyβ and Lyγ, which is characterized by the resonance behavior around line center. The figure also shows the branching ratio of Raman scattering into Balmer series, which is given as the ratio of the Raman cross section de-excited to $2s$ state divided by the total cross section. As Chang et al. (2015) pointed out, extremely
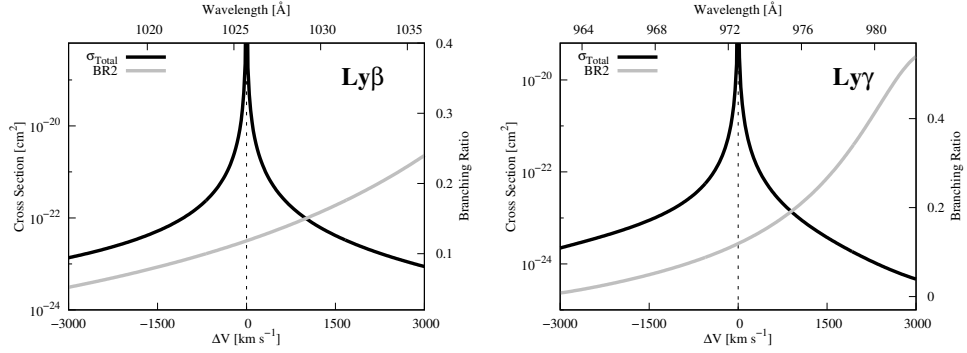
Figure 3.2: Total cross section (black solid lines) and Balmer branching ratios (grey solid lines) near Lyβ and Lyγ computed using the Kramers-Heisenberg formula.

broad Raman scattering wings of Hα and Hβ show asymmetry between red-ward and blueward. Also, a hydrogen atom in the excited $3p$ level de-excites into the level $2s$ with a probability of 0.12 and with the remaining probability of 0.88 it de-excites into the ground level.

3.3.2   Scattering Geometries for Thomson and Raman Wings

The left panel of Fig. 3.3 illustrates schematically the Thomson scattering geometry considered in this work. We adopt a static H II region in the form of a sphere with radius R and a uniform electron number density n_e, where hydrogen Balmer line photons are generated in a uniform fashion and Thomson scattered. We introduce the Thomson scattering optical depth $\tau_{Th} = n_e \sigma_{Th} R$ to characterize the H II region.

The parameter space considered in this work is described by the electron temperature $T_e \geq 10^4\,\mathrm{K}$ and the Thomson optical depth $\tau_{Th} \leq 0.1$.
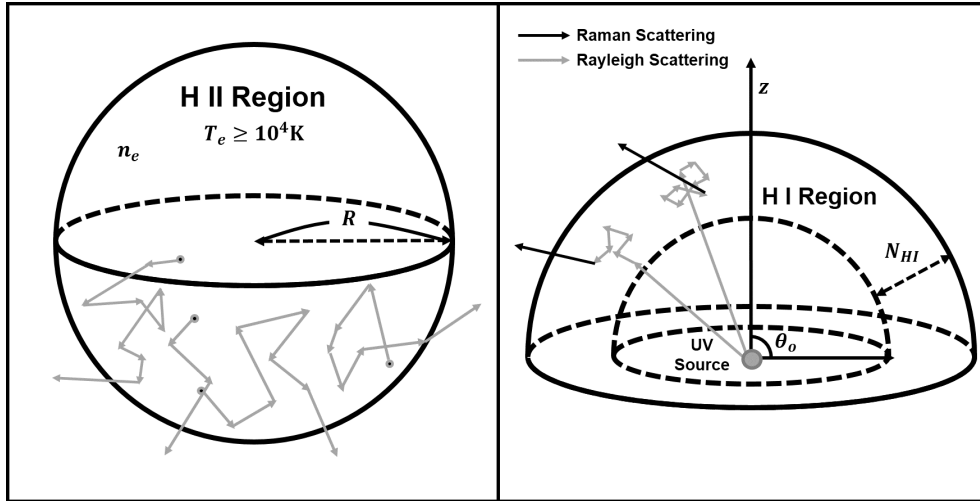
Figure 3.3: Scattering geometries of the Thomson scattering (left panel) and Raman scattering (right panel) adopted in this work. In the case of Thomson scattering, free electrons are distributed with a constant number density n_e in a sphere with radius R. The sphere is characterized by the Thomson optical depth $\tau_{Th} = n_e \sigma_{Th} R$. Hα line photons are assumed to be generated uniformly inside the sphere. In the case of Raman scattering, the scattering neutral region takes a form of a partial spherical shell with a half-opening angle θ_o. The far UV emission source coincides with the center of the partial spherical shell.

The Monte Carlo simulation for Thomson wings starts with a generation of a Balmer line photon in a random place inside the spherical H II region with an initial frequency chosen to be a Gaussian random deviate with the standard deviation of $\sigma_v = 30$ km s^{-1} in the Doppler space. It should be noted that this velocity is quite smaller than the electron thermal velocity $v_{th} \sim 390$ km s^{-1} at $T_e = 10^4$ K.

We show a scattering geometry of Raman scattering wings in the right panel of Fig. 3.3. Dumm et al. (1999) investigated an eclipsing symbiotic

star SY Muscae to measure the H I column density as a function of binary orbital phase. They found that N_{HI} varies from 10^{21} cm^{-2} to 10^{25} cm^{-2}, where an extremely high column density of 10^{25} cm^{-2} is limited to the orbital phase near $\phi_{orbit} = 1$ with the giant companion in front of the white dwarf component. From this result, we may imagine that a neutral region with $N_{HI} \sim 10^{21}$ cm^{-2} may surround the binary system quite extensively. In this work, the scattering neutral region is assumed to be a partial spherical shell with a half-opening angle θ_o which is converted to the covering factor $CF = (1 - \cos \theta_o)/2$.

We locate the far UV emission source at the center of the partial spherical shell. Treating as a point source, we consider flat and isotropic continuum around Lyman series. The partial spherical H I region is characterized by a neutral hydrogen column density N_{HI} along the radial direction.

3.3.3 Monte Carlo Approach

We adopt a Monte Carlo technique to produce simulated wings around Hα formed through Raman scattering and Thomson scattering. We generate a photon in the emission region with an initial wavevector $\hat{\mathbf{k}}$ and follow its path until escape from the scattering region. Thomson scattering is characterized by the scattering phase function given by

$$f(\mu) \propto 1 + \mu^2, \tag{3.12}$$

where $\mu = \cos\theta_s$ is the cosine of the angle θ_s between the incident and scattered wavevectors. The same phase function also describes Rayleigh and Raman scattering as long as the incident photon is off-resonant where the deviation from line center is sufficiently larger than the fine structure splitting (Stenflo 1980).

A convenient formalism incorporating the polarization information is the density matrix approach, in which a Hermitian 2×2 matrix $[\rho]$ is associated with a given photon. The density matrix elements are easily interpreted in terms of the Stokes parameters I, Q, U and V, where

$$
\begin{aligned}
I &= \rho_{11} + \rho_{22} \\
Q &= \rho_{11} - \rho_{22} \\
U &= \frac{1}{2}Re[\rho_{12}] = \frac{1}{2}Re[\rho_{21}] \\
V &= \frac{1}{2}Im[\rho_{12}] = -\frac{1}{2}Im[\rho_{21}].
\end{aligned}
\tag{3.13}
$$

For a photon propagating in the direction $\hat{\mathbf{k}} = (\sin\theta\cos\phi, \sin\theta\sin\phi, \cos\theta)$, we may choose a set $\{|\epsilon_1 >, |\epsilon_2 >\}$ of basis vectors representing the polarization states, where

$$
\begin{aligned}
|\epsilon_1 > &= (-\sin\phi, \cos\phi, 0), \\
|\epsilon_2 > &= (\cos\theta\cos\phi, \cos\theta\sin\phi, -\sin\theta).
\end{aligned}
\tag{3.14}
$$

The density matrix elements ρ'_{ij} associated with the scattered radiation with $\hat{\mathbf{k}}_f = (\sin\theta'\cos\phi', \sin\theta'\sin\phi', \cos\theta')$ are related to those for the incident pho-

55

ton

$$\rho'_{ij} = \sum_{kl} <\hat{\mathbf{e}}'_i|\hat{\mathbf{e}}_k> \rho_{kl} <\hat{\mathbf{e}}'_j|\hat{\mathbf{e}}_l>, \tag{3.15}$$

where $<\hat{\mathbf{e}}'_j|\hat{\mathbf{e}}_l>$ is an inner product between the two polarization basis vec-

tors $|\hat{\mathbf{e}}_l>$ and $|\hat{\mathbf{e}}'_i>$ associated with the incident and scattered photons,

respectively. A more detailed explanation can be found in (e.g. Lee et al.

1994; Ahn & Lee 2015).

In the Monte Carlo simulations, each scattering optical depth τ tra-

versed by a photon in the scattering region is given in a probabilistic way

as

$$\tau = -\ln X, \tag{3.16}$$

where X is a uniform random number between 0 and 1. This optical depth

τ is inverted to a physical distance in order to locate the next scattering

site. In the case of Thomson scattering, the physical distance l_{Th} is given

by

$$l_{\mathrm{Th}} = \frac{\tau}{n_e \sigma_{Th}}. \tag{3.17}$$

Using this value, we determine the next scattering position r_s by the

relation

$$r_s = r_i + l_{\mathrm{Th}}\hat{k}, \tag{3.18}$$

where r_i is the position vector of the previous scattering site. If r_s is outside

the ionized nebular region, the photon is considered to escape from the re-

gion to reach the observer. Otherwise, we iterate the process to find a new

scattering position treating r_s as starting position.

In the case of transfer of a far UV photon near Lyβ and Lyγ, the pho-

ton under study may be Rayleigh scattered several times before it becomes

an optical photon through Raman scattering. The H I region is assumed

to be optically thin for optical photons near Hα and Hβ so that a Raman

scattered photon directly escapes to reach the observer.

The physical distance l_{Ram} corresponding to a probabilistic scattering

optical depth τ,

$$l_{\mathrm{Ram}} = \frac{\tau}{n_{HI}\sigma_{tot}}, \tag{3.19}$$

and the next scattering site is

$$r_s = r_i + l_{\mathrm{Ram}}\hat{k}. \tag{3.20}$$

At the location of r_s, we generate a new wavevector k_o. Using another uni-

form random number X' and the Raman branching ratio b, decision is made

for the scattering type. If it is Raman, then the photon is regarded as an

optical photon, which directly escapes in the direction of k_o. Otherwise, the

scattering is Rayleigh and we determine the next scattering site by obtaining

a revised l_{Ram}.

In dealing with Rayleigh scattering, we fix the wavelength of a given

photon because the thermal motion of an atomic hydrogen in H I region is

negligible compared to the wing widths $> 10^3$ km s^{-1}.
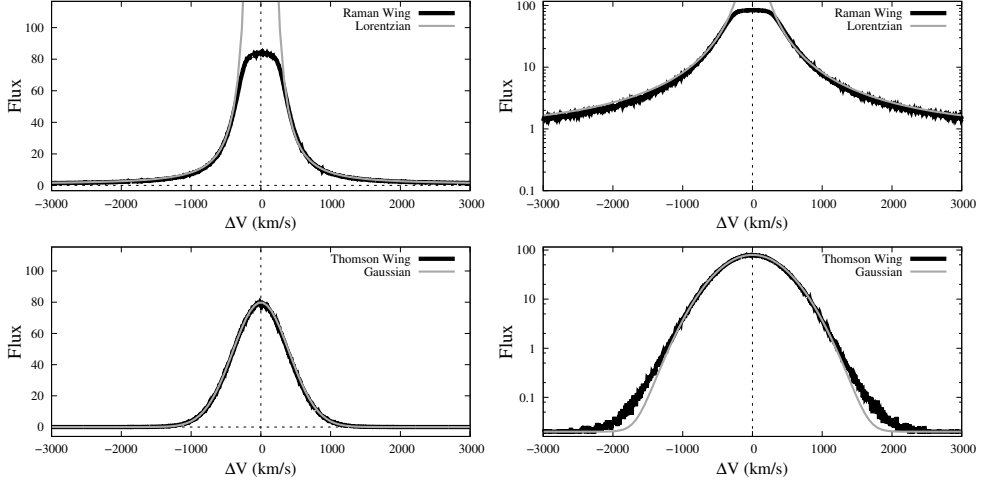
Figure 3.4: Black solid lines and grey solid lines show our Monte Carlo results and fitting functions for broad wings. The top panels and the bottom panels show Raman and Thomson scattering wings formed in scattering geometries illustrated in the right and left panels Fig 3.3, respectively. The fitting functions shown in grey solid lines are a Gaussian and a Lorentzian for Raman wings and Thomson wings, respectively.

On the other hand, Thomson scattered photons suffer diffusion in frequency space with a step corresponding to the thermal motion of free electrons. The velocity of a free electron v_{th} is selected in a probabilistic way using Gaussian random deviates. The Thomson scattering is treated as elastic in the rest frame of the scatterer. Transforming to the observer's frame, we obtain the relation between the wavelengths before and after scattering λ_i and λ_f

$$\lambda_f = \left(1 - \frac{\hat{k}_f \cdot v_{th}}{c}\right)\left(1 + \frac{\hat{k} \cdot v_{th}}{c}\right)\lambda_i. \tag{3.21}$$

58

3.4 Simulated Broad Balmer Wing Profiles

In this section, we present broad wings obtained from our Monte Carlo calculations for Raman scattering with atomic hydrogen and Thomson scattering with free electrons. Two representative wing profiles are shown in Fig. 3.4, where the top and bottom panels are for Raman and Thomson wings, respectively. The black thick solid lines show our Monte Carlo result and grey thin solid lines are fitting functions.

In the left panels, the vertical scale is linear whereas the right panels are presented in logarithmic scale in order for easy comparisons with fitting functions. In the bottom right panel, the Thomson wings show excess at $|\Delta V| > 1000$ km s^{-1} compared to the fitting Gaussian function. Multiple Thomson scattering may result in deviation of the wing profile from a pure Gaussian, because Thomson scattering involves diffusion in frequency space as well as spatial diffusion (e.g., Kim et al. 2007).

The Raman wing feature is fitted with a Lorentzian function, because the Raman cross section near Lyβ is roughly approximated by a Lorentzian function due to the proximity of resonance (e.g., Lee 2013). The Thomson wing profile is fitted with a Gaussian function because the free electron region is assumed to follow a Maxwell-Boltzmann distribution. As ΔV is increased, the Gaussian nature forces Thomson wings to decay much more rapidly than Raman wings.

3.4.1 Thomson Wings

Fig. 3.5 shows Thomson wings obtained from our Monte Carlo simulations

for various values of the electron temperature T_e and Thomson optical depth

τ_{Th}. The horizontal axis is the Doppler factor and the vertical axis is rela-

tive photon number represented in linear scale. In the Monte Carlo simula-

tions, we collect only those photons Thomson scattered at least once ignor-

ing emergent photons without being scattered at all.

In order to describe the Thomson wings in a quantitative way, we in-

troduce a parameter 'TSF (Thomson scattered fraction)' defined by

$$\text{TSF}(\Delta V)d(\Delta V) = \frac{N_{scat}(\Delta V)}{N_{init}}d(\Delta V). \qquad (3.22)$$

Here, N_{init} is the number of photons initially emitted from the uniform H II

region and $N_{scat}(\Delta V)d(\Delta V)$ represents the number of collected photons hav-

ing a Doppler factor in the interval ΔV and $\Delta V + d(\Delta V)$. For simplicity,

we take $d(\Delta V) = 100\,\text{km s}^{-1}$. In Fig. 3.5, the vertical axis shows 'TSF'.

The left panels of Fig. 3.5 show Thomson wings for $T_4 = 1, 2$ and 5 with

the Thomson optical depth fixed to $\tau_{Th} = 0.1$. Because of small Thomson

optical depth, the number of scattering averaged over all collected photons

is slightly larger than unity. In this situation, the Thomson wings follow ap-

proximately a Maxwell-Boltzmann distribution with a width proportional to

$T_e^{1/2}$. This is illustrated by the result that the total wing flux is almost con-
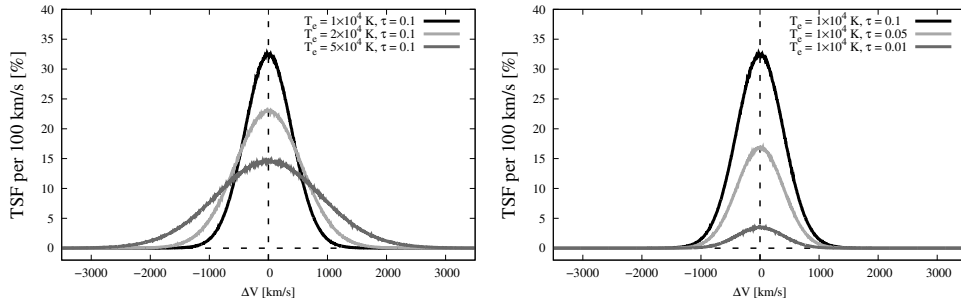
Figure 3.5: Thomson wing profiles obtained from our Monte Carlo simulations for various values of electron temperature T_e and Thomson scattering optical depth τ_{Th}. The left panel shows Thomson wings for three values of $T_e = 1 \times 10^4, 2 \times 10^4$ and 3×10^4 K with the Thomson optical depth fixed to $\tau_{Th} = 0.1$. The right panel shows Thomson wings for fixed $T_e = 10^4$ K and four values of $\tau_{Th} = 0.01, 0.05$ and 0.1.

stant while the width increases as T_e increases.

The right panels show Thomson wings for various values of the Thomson optical depth $\tau_{Th} = 0.01, 0.05$ and 0.1 at fixed $T_4 = 1$. For $\tau_{Th} < 1$, the wing flux is roughly proportional to τ_{Th} while the profile width remains unchanged.

3.4.2 Raman Wings

Fig. 3.6 shows Raman wings near Hα and Hβ obtained with our Monte Carlo code, which simulates Raman wing formation in a neutral partial spherical shell illuminated by a flat continuum around Lyβ and Lyγ. For a flat incident continuum, the Raman wing profile is identified with the Raman
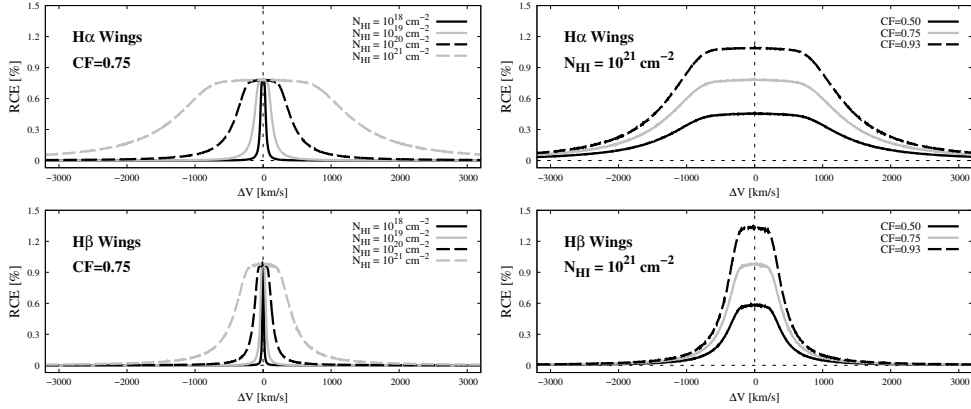
Figure 3.6: Monte Carlo simulated Raman wings around Hα (top panels) and Hβ (bottom panels) formed in a neutral partial spherical shell illustrated in the right panel of Fig. 3.3. The left panels show Raman wings for a fixed value of $CF = 0.75$ varying the neutral hydrogen column density N_{HI} in the range $10^{18} - 10^{21}$ cm^{-2}. The right panels are Raman wings for various values of θ_o and a fixed $N_{HI} = 10^{21}$ cm^{-2}.

conversion efficiency (RCE) per unit scattered wavelength λ_o, defined by

$$\text{RCE}(\lambda_o)d\lambda_o = \frac{N_{Raman}}{N_{total}}d\lambda_i. \tag{3.23}$$

Here, N_{total} is the number of incident photons from the flat and isotropic source per incident wavelength λ_i. The wavelength of Raman scattered radiation λ_o is related to λ_i by Eq. 3.5. We also denote by N_{Raman} the number of Raman scattered photons collected over all lines of sight. In Fig. 3.6, the vertical axis shows 'RCE' as a function of the Doppler factor in the observed frequency space. We consider various values of $N_{HI} = 10^{18} - 10^{21}$ cm^{-2} and $CF = 0.5 - 0.93$.

Quantitatively we obtain RCE ~ 0.01 for Hα and Hβ wings, respectively. Quite unlike the case of Thomson wings, Hα wings are much broader

than those of Hβ, which is explained by overall larger cross section around

Lyβ than Lyγ. As is shown in Fig. 3.6, the widths of Raman Hα wings are

almost three times larger than those of Hβ in the Doppler space. The small

Raman conversion efficiency is attributed to the smallness of the factor

$$A = \frac{d\lambda_i}{d\lambda_o} = \left(\frac{\lambda_i}{\lambda_o}\right)^2, \tag{3.24}$$

which gives the ratio of the one-dimensional volumes of incident frequency

space and Raman frequency space. Approximately the ratios are approxi-

mately 0.025 and 0.04 near Hα and Hβ, respectively. A close look at Fig. 3.6

reveals higher 'RCE' for Hβ than Hα near line center, where Raman scatter-

ing cross section is high. This is explained by the larger value of 'A' factor

for Hβ than that for Hα.

Chang et al. (2015) showed that Raman wings around Hα, Hβ and Paα

exhibit different widths and strengths when they are formed in a region with

high column density $N_{HI} \geq 10^{22}\,\mathrm{cm}^{-2}$ due to significant differences in the

cross section $\sigma^{Ram}(\omega)$ and branching channels. The widths of Raman wings

are roughly proportional to $N_{HI}^{1/2}$ as Chang et al. (2015) showed. In the

same work, the Raman conversion efficiency is saturated to remain flat near

the line center, where the Raman scattering optical depth exceeds unity.

The right panels in Fig. 3.6 show our Monte Carlo results for three

values of the covering factor 'CF' at fixed N_{HI}. In the case of high CF,

Rayleigh escaping far UV photons may reenter the scattering region to pro-
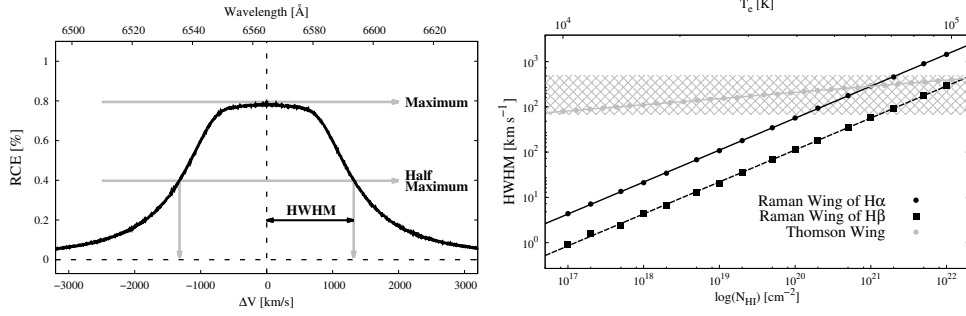
Figure 3.7: Half width at half maximum (HWHM) of Thomson and Raman
wings computed with a Monte Carlo technique. HWHM of Thomson wings
is presented with grey dots as a function of T_e shown in the upper hori-
zontal axis with a fixed $\tau_{Th} = 0.1$. Data for Raman Hα and Hβ wings are
shown by black circle and square marks, respectively, as a function of N_{HI}
corresponding to the lower horizontal axis.

vide an additional contribution to the final 'RCE'. The effect of reentry is

considered in this work, which results in nonlinear response of Raman wing

flux as a function of 'CF'.

3.4.3   Comparison of Simulated Raman and Thomson Wings

In this subsection, we compare Raman wings around Hα and Hβ and Thom-

son wings produced in our Monte Carlo simulations. Fig. 3.7 shows the HWHM

of Raman wings around Hα (black dots) and Hβ (black squares) obtained

for various values of $N_{HI} = 10^{17} - 10^{22}\,\mathrm{cm}^{-2}$. The lower horizontal axis shows

N_{HI} in logarithmic scale. Note that the vertical scale is also logarithmic. We

also plot the HWHM of Thomson wings with grey dots for various values of

the electron temperature $T_4 = 1 - 10$. The upper horizontal axis represents

T_e in logarithmic scale. It should be noted that in the Doppler factor space

64

Thomson wings of Hα are identical with those of Hβ due to the indepen-
dence of Thomson cross section on wavelength.

The linear relations shown in logarithmic scales in Fig. 3.7 imply that
the HWHMs of Raman and Thomson wings are related to N_{HI} or T_e by a
power law. We provide the fitting relations as follows

$$
\begin{aligned}
\mathrm{HWHM_{Raman\,H\alpha}} &= 418\ N_{20}^{0.49}\ \mathrm{km\ s^{-1}} \\
\mathrm{HWHM_{Raman\,H\beta}} &= 135\ N_{20}^{0.49}\ \mathrm{km\ s^{-1}} \\
\mathrm{HWHM_{Thomson}} &= 532\ T_4^{0.49}\ \mathrm{km\ s^{-1}}, \quad\quad (3.25)
\end{aligned}
$$

where $N_{20} = N_{HI}/[10^{20}\ \mathrm{cm^{-2}}]$ is the H I column density divided by $10^{20}\ \mathrm{cm^{-2}}$.

The Raman wing widths are approximately proportional to $N_{HI}^{1/2}$, which
is attributed to the fact that the total scattering cross sections around Ly-
man series are approximately proportional to $\Delta\lambda^{-2}$. On the other hand, the
Thomson wing widths are proportional to $T_e^{1/2}$, which reflects the fact that
the electron thermal speed $v_{th} \propto T_e^{1/2}$.

From Eq. (3.25), one may notice that the HWHMs of Raman Hα wings
are approximately three times as large as those for Hβ . In the range of
electron temperature $T_4 = 1 - 10$, the HWHM of Thomson wings lies in
the narrow range of $1,080 \pm 550$ km s^{-1}, reflecting the fact that the width
of Thomson wings is mainly determined by the thermal electron speed v_{th}.
Based on this result, it may be argued that Thomson scattering is inade-

quate to explain broad wings observed to exhibit HWHM < 530 km s^{-1}, noting that an ionized region is hardly colder than 10^4 K (e.g. Osterbrock & Ferland 2006). The same argument can be made for wings that may exceed several 10^3 km s^{-1} often reported in the planetary nebula M2-9, for which Balick (1989) reported the presence of broad Hα wings with a width $> 10^3$ km s^{-1}.

For $N_{HI} = 10^{20-21}$ cm^{-2} and $T_e = 10^{4-5}$ K, the widths of Raman Hα wings and Thomson wings are comparable. In the case of Raman wings, Hα wings are much broader than Hβ counterparts by a factor of three, as stated earlier. The observational clear signature for Raman origin is the unambiguous disparity of the wing widths of Hα and Hβ. However, observationally Hβ is weaker than Hα rendering Hβ wings often poorly measured. In contrast to simulations, no unequivocal isolation of wing photons or scattered photons from the entire Balmer emission flux is apparent with the observed spectra, preventing one from measuring the HWHMs of the observed Balmer wings.

3.4.4 Comparison with the Observed Spectra of AG Dra and Z And

In this subsection, we compare our simulated wing profiles with the observed data in the Doppler factor space. Hα and Hβ profiles are normalized so that their peaks coincide with the numerical value of 101 and the underlying con-
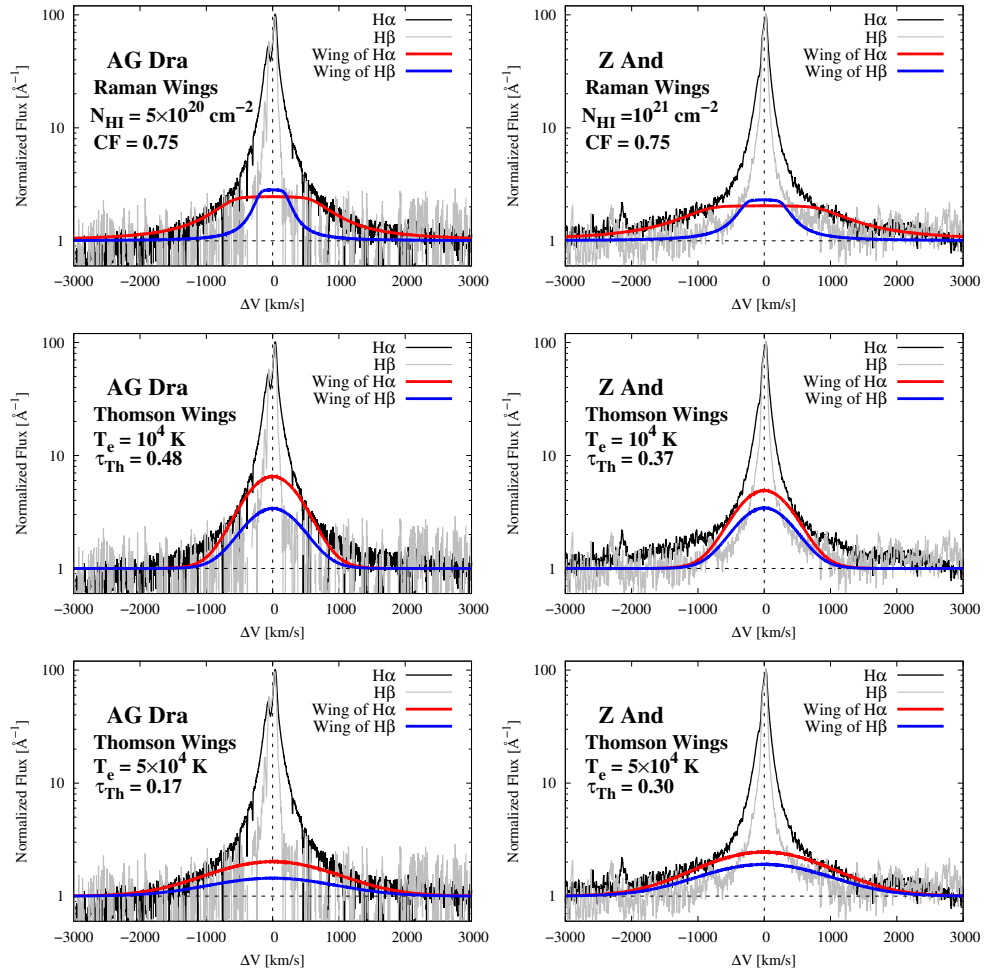
Figure 3.8: Comparison of our Monte Carlo wing profiles and the *CFHT* spectrum around Hα and Hβ of AG Dra (left panels) and Z And (right panels) obtained with *CFHT*. The horizontal axis is the Doppler factor in units of km s^{-1}. The vertical scale is logarithmic normalized flux.

tinuum has the value of 1. In Fig. 3.8, all the vertical axes are given in logarithmic scale.

The top two panels of Fig. 3.8 show our simulated Raman Hα and Hβ wings in red and blue lines, respectively, which provide our best fit to the *CFHT* spectra of AG Dra and Z And. The best fit profiles are selected by eye. The H I column densities adopted for the simulation are $N_{HI} = 5 \times 10^{20}$ cm^{-2} and 10^{21} cm^{-2} for AG Dra and Z And, respectively, with $CF = 0.75$ for both objects. The contribution of the Raman wings to the observed Hα and Hβ is 15.5% and 14.7% for AG Dra and 16.3% and 12.2% for Z And.

We present a conversion between the relative flux scale in Fig. 3.1 and physical scale for a typical symbiotic star characterized by the white dwarf mass $M_* = 0.6$ M$_\odot$ and a radius $R_* = 0.01$ R$_\odot$ (Mürset et al. 1991). An accretion rate of $\dot{M} = 10^{-7}$ M$_\odot$ yr^{-1} (Tomov & Tomova 2002; Tomov et al. 2008) gives rise to the accretion luminosity

$$L_{acc} = \frac{GM_* \dot{M}}{R_*} \sim 200 \ L_\odot.$$

$$(3.26)$$

According to Mürset et al. (1991) the luminosities of AG Dra and Z And are $10 \, L_\odot$ and $600 \, L_\odot$, respectively, whereas the temperature of the hot component is about 10^5 K for both the objects.

High ionization lines including O VI$\lambda\lambda$1032 and 1038 are common in many symbiotic stars indicating a hot ionizing source with $T_h \sim 10^5$ K (Mürset et al. 1991; Birriel et al. 2000). The specific luminosity at around Lyβ from

a black body with a temperature $T_h = 1.5 \times 10^5$ K and luminosity L_{acc} is

$$L_\lambda^{acc} \sim 8 \times 10^{33} \text{ erg s}^{-1} \text{ Å}^{-1}. \qquad (3.27)$$

The distances to AG Dra and Z And are poorly known and, for example,
according to Tomov & Tomova (2002) and Tomov et al. (2008) they are
1.7 kpc for AG Dra and 1.1 kpc for Z And, respectively. In terms of the
distance D, the flux density F_λ^{acc} near Lyβ associated with the accretion
specific luminosity in Eq. (3.27) is

$$F_\lambda^{acc} \sim 8.4 \times 10^{-10} \left(\frac{D}{1 \text{ kpc}} \right)^{-2} \text{ erg cm}^{-2} \text{ s}^{-1} \text{ Å}^{-1}. \qquad (3.28)$$

In order to simulate the Raman wings around Hα and Hβ shown in the
top panels of Fig. 3.8, continuum photons around Lyβ and Lyγ are gener-
ated in the far UV emission source in Fig 3.3. In our simulation, we consider
the incident continuum flux ($ICF_{Ly\beta}$) near Lyβ that is locally flat. The in-
cident continuum flux is measured in unit of Å^{-1} for which the physical
conversion of the unit value of $ICF_{Ly\beta} = 1$ Å^{-1} is discussed in Appendix
B.

For the Raman wings of Hα in Fig. 3.8, we find $ICF_{Ly\beta} = 3.3$ Å^{-1}
and 4.5 Å^{-1} for AG Dra and Z And, respectively. If the Hα line flux is 2×10^{-10} erg cm^{-2} s^{-1}, then these values are converted into 2.7×10^{-10} and
3.4×10^{-10} erg cm^{-2} s^{-1} Å^{-1} for AG Dra and Z And, respectively.

A similar procedure is taken for $ICF_{Ly\gamma}$ near Lyγ for Raman wings around Hβ. In the simulations, we use $ICF_{Ly\gamma} = 7.4\,\text{Å}^{-1}$ and $5.4\,\text{Å}^{-1}$ for AG Dra and Z And, respectively, which are transformed to 1.3×10^{-11} and 2.0×10^{-11} erg cm^{-2} s^{-1} Å^{-1}, respectively. In Appendix B, the conversion of ICF from our parametrization into physical units is discussed.

The middle and bottom panels Fig. 3.8 show Thomson wings simulated with two different values of $T_e = 10^4$ K and $T_e = 5 \times 10^4$ K for comparisons with the observed data. In each panel, the Thomson Hα profile is stronger than Thomson Hβ counterpart, simply because we injected more Hα photons than Hβ photons. We compute the total number flux $TF_{H\alpha}$ of Hα defined by

$$TF_{H\alpha} = \int_{\lambda(\Delta V = -500\,\text{km/s})}^{\lambda(\Delta V = +500\,\text{km/s})} NF_{H\alpha}(\lambda)d\lambda, \tag{3.29}$$

where $NF_{H\alpha}(\lambda)$ is the observed flux normalized to have the peak value of 101. In a similar way, $TF_{H\beta}$ is computed to yield the ratio of $TF_{H\alpha}/TF_{H\beta} = 2.0$ and 1.6 for AG Dra and Z And, respectively.

These observed ratios are used to show Thomson Hα and Hβ wings in Fig. 3.8. In the middle panels ($T_e = 10^4$ K), the Thomson optical depths are $\tau_{Th} = 0.48$ and 0.37 for AG Dra and Z And. In the bottom panels ($T_e = 5 \times 10^4$ K), smaller values of $\tau_{Th} = 0.17$ and 0.30 are used for AG Dra and Z And, respectively.

In the middle panel, the near wing parts $|\Delta V| < 500$ km s^{-1} are well

fit whereas the quality of fit becomes poor in the far wing parts. An opposite behavior is seen in the bottom panel, where good fit is obtained in the far wing parts. It should be noted that the electron temperature $T_e = 5 \times 10^4$ K is significantly higher than the values considered in the work of Sekerá (š & Skopal (2012) who analyzed the Thomson wing profiles of O VI and He II emission lines.

3.5 Conclusion and Discussion

In this article, we used a Monte Carlo technique to produce broad wings around Hα and Hβ. The adopted physical mechanisms include Thomson scattering of Hα and Hβ by free electrons and Raman scattering of Lyβ and Lyγ by atomic hydrogen. In the case of Thomson wings, the wing profiles are well-approximated by a Gaussian function whose width is mainly determined by the temperature of the free electron region. The Thomson scattering optical depth determines the resultant Thomson wing flux.

On the other hand, Raman wing profiles follow the Lorentzian function, which also describes the cross section. In the case of Raman wings, the wing flux is mainly affected by the H I column density and the covering factor of the neutral region. The cross section near Lyβ is much larger than that near Lyγ, which leads to Raman Hα wings much stronger than Hβ counterpart. When Balmer lines are overplotted in the Doppler factor space, Raman Hα

wings are expected to appear stronger and broader than Hβ wings.

We also presented high resolution spectra of the two S type symbiotic stars AG Dra and Z And obtained with the *CFHT* in 2014 in order to make quantitative comparisons with simulated Thomson and Raman wings. The observational data and simulated data were shown in logarithmic scale, from which we notice that Raman wings provide better fit than Thomson wings.

Sekerá (š & Skopal (2012) presented a convincing argument that the broad wings around O VI and He II lines are formed through Thomson scattering. It may be that Balmer emission lines are formed in a more extended region than O VI and He II, having higher ionization potential than H I. In this case, it is expected that the fraction of Thomson scattered flux is much smaller for Balmer lines than for O VI and He II.

Considering the difficulty of explaining far wings with $\Delta V > 10^3$ km s^{-1} through Thomson scattering, it remains as an interesting possibility that near wing parts are significantly contributed by Thomson scattering whereas Raman scattering is the main contributor to the far wing parts. This possibility may imply complicated polarization behavior in the wing parts due to different scattering geometries for Thomson and Raman processes.

Broad wings can also be formed from a hot tenuous wind around the compact component with a high speed (e.g., Skopal 2006). Because the flux ratio of Hα and Hβ in the fast wind will be given by the recombination

rate, it is expected that the flux ratio in the wing part will be similar to that in the emission core part. This strongly implies that Hα and Hβ will show similar profiles in the Doppler factor space. In consideration of this, the disparity of wing widths in Hα and Hβ may indicate substantial contribution of Raman scattering to the Balmer wing formation.

Balmer wings formed through scattering are expected to develop significant linear polarization, implying that spectropolarimetry will shed much light on the physical origin. According to Kim et al. (2007), Thomson wings may exhibit a complicated polarization structure because multiply scattered photons tend to contribute more to the far wing parts than to the near wing parts. Kim et al. (2007) proposed that far wings are less strongly polarized than near wing regions.

In the case of Raman scattering, wings may also be strongly polarized depending on the scattering geometry and the location of far UV emission source. Yoo et al. (2002) investigated linear polarization and profiles of Raman scattered Hα profiles. They proposed that the degree of linear polarization may increase as ΔV where single scattering dominates. Ikeda et al. (2004) carried out spectropolarimetry of AG Dra and Z And to propose that the polarization behavior of Raman O VIλ 6825 is similar to that of Hα wings lending support to the Raman scattering origin. However, their analysis of Hα was limited to a relatively narrow region $|\Delta V| < 500$ km s^{-1},

which is insufficient to rule out the formation through Thomson scattering.

Broad Hα wings are also found in young planetary nebulae including IC5117 and IC4997 (e.g Lee & Hyung 2000; Arrieta & Torres-Peimbert 2002). Van de Steene et al. (2000) also reported that some post-AGB stars show broad Hα wings. The operation of Raman scattering by atomic hydrogen is also known for far UV He II lines near H I Lyman series in symbiotic stars and a few planetary nebulae including NGC 7027, NGC 6790, IC 5117 and NGC 6302 (e.g. Kang et al. 2009; Lee et al. 2006; Péquignot et al. 1997; Groves et al. 2002). Raman scattered He II features are formed in the blue wing parts of Balmer emission lines. Raman scattering cross section of He II λ1025 is $\sigma \sim 7.2 \times 10^{21}$ cm^2, from which a broad scattered feature is formed at 6545 Å. The planetary nebulae with Raman He II are known to exhibit broad Hα wings, which may be regarded as circumstantial evidence of contribution to Balmer wings from Raman scattering.

3.6   Appendix for Chapter 3

A1 Normalization of CFHT data

In Fig. 3.9, we show the spectra of AG Dra and Z And obtained with the *CFHT*. The spectra not being flux calibrated, the vertical axis shows the relative flux (*RF*) in an arbitrary scale per Å. In turn, Table 3.2 shows the
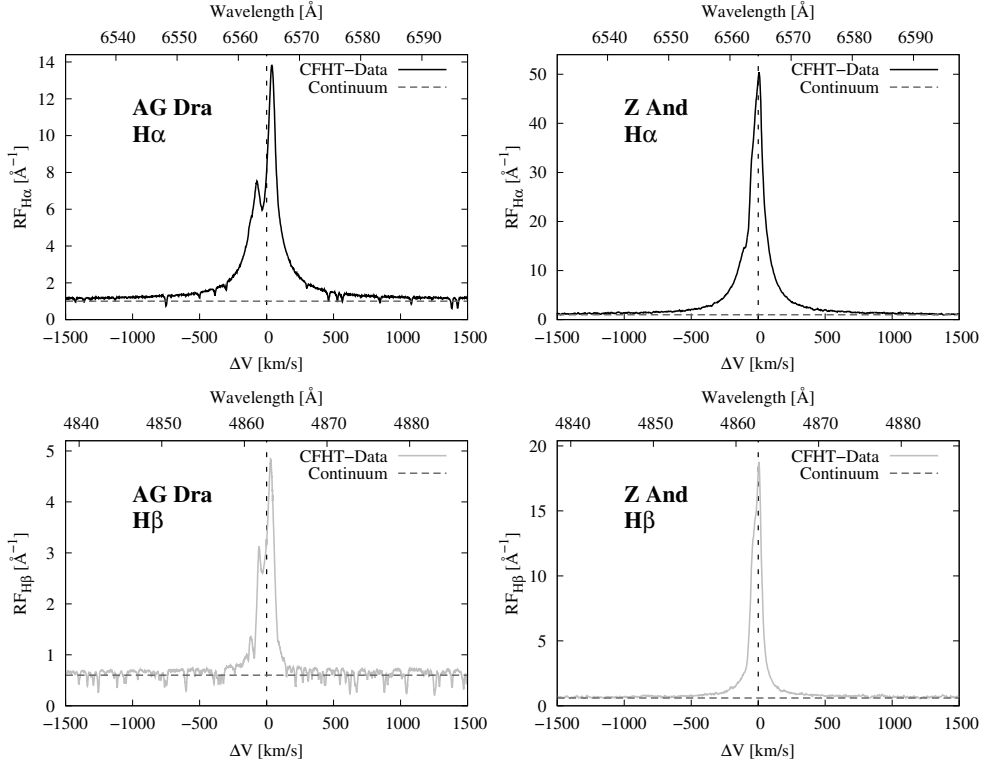
Figure 3.9: Comparison of our Monte Carlo wing profiles and the *CFHT*
spectra around Hα and Hβ of AG Dra (left panels) and Z And (right panels)
obtained with *CFHT*. The horizontal axises are the wavelength in units of
Å and the Doppler factor from line center in units of km s^{-1}. The vertical
axis is the relative flux.

Table 3.2: Parameters for the observed profiles of Hα and Hβ in Fig 3.9

Object	Line	*PV*	*CL*	*EW*
AG Dra	Hα	13.82 Å^{-1}	1.000 Å^{-1}	106.7 Å
AG Dra	Hβ	4.839 Å^{-1}	0.600 Å^{-1}	47.15 Å
Z And	Hα	50.44 Å^{-1}	1.000 Å^{-1}	238.8 Å
Z And	Hβ	18.77 Å^{-1}	0.600 Å^{-1}	88.70 Å

measured values of the peak value (PV), continuum level (CL) and equiva-

lent width (EW) for the Hα and Hβ emission lines. Transformation of the

relative flux into a physical unit can be facilitated once the total line flux of

an emission line is fixed. For example, Tomov & Tomova (2002) reported

the total line flux of Hα $F_{H\alpha} = 2 \times 10^{-10}$ erg cm^{-2} s^{-1} for AG Dra and a

similar value was also reported for Z And by Tomov et al. (2008). In this

case, the unit relative flux $(RF = 1$ Å$^{-1})$ in the spectra of Fig. 3.9 corre-

sponds to

$$RF = 1 \text{ Å}^{-1} \iff \frac{F_{H\alpha}}{EW} \left(\frac{CL}{1 \text{ Å}^{-1}} \right) = 2 \times 10^{-12} \left(\frac{100 \text{ Å}}{EW} \right) \left(\frac{CL}{1 \text{ Å}^{-1}} \right) \text{ erg cm}^{-2} \text{ s}^{-1} \text{ Å}^{-1}.$$

(3.30)

Also it should be noted that the equivalent width (EW) is independent of

the scale.

In Figs. 3.1 and 3.8, the normalized flux (NF) was introduced for pro-

file comparisons of Hα and Hβ, where the normalized flux (NF) is related

to RF by the following relation

$$NF = (RF - CL) \left[\frac{100 \text{ Å}^{-1}}{PV - CL} \right] + (1 \text{ Å}^{-1}).$$

(3.31)

With this relation, the normalized flux has the peak value to be 101 Å^{-1}

of NF for both Hα and Hβ. Because PV and CL of Hα differ from those

of Hβ, different conversion into a physical unit is applied for $NF_{H\alpha}$ around

Hα and $NF_{H\beta}$ around Hβ.

Around Hα, the unit value $NF_{H\alpha} = 1$ Å^{-1} of the normalized flux corresponds to

$$NF_{H\alpha} = 1 \text{ Å}^{-1} \iff \left(\frac{F_{H\alpha}}{EW}\right) \left(\frac{CL}{1 \text{ Å}^{-1}}\right) \left(\frac{PV - CL}{100 \text{ Å}^{-1}}\right), \qquad (3.32)$$

where PV, CL and EW are measured values for Hα. With the fiducial value of $F_{H\alpha} = 2 \times 10^{-10}$ erg s^{-1} cm^{-2}, we have

$$NF_{H\alpha} = 1 \text{ Å}^{-1} \iff 2\times10^{-12} \left[\frac{PV - CL}{100 \text{ Å}^{-1}}\right] \left[\frac{CL}{1 \text{ Å}^{-1}}\right] \left[\frac{100 \text{ Å}}{EW}\right] \text{ erg cm}^{-2} \text{s}^{-1} \text{Å}^{-1}.$$
$$(3.33)$$

The ratios $F_{H\alpha}/F_{H\beta}$ measured from our *CFHT* spectra are 3.77 and 4.49 for AG Dra and Z And, respectively. Using these mesaured ratios, the normalized flux $NF_{H\beta}$ around Hβ is converted into

$$NF_{H\beta} = 1 \text{ Å}^{-1} \iff \frac{F_{H\beta}}{EW} \frac{CL}{1 \text{ Å}^{-1}} \frac{PV - CL}{100 \text{ Å}^{-1}}. \qquad (3.34)$$

Adopting the ratio $F_{H\alpha}/F_{H\beta}$, NF in unit of Å^{-1} in the simulation is converted to

$$NF_{H\beta} = 1 \text{ Å}^{-1} \iff 2\times10^{-12} \left[\frac{F_{H\beta}}{F_{H\alpha}}\right] \left[\frac{PV - CL}{100 \text{ Å}^{-1}}\right] \left[\frac{CL}{1 \text{ Å}^{-1}}\right] \left[\frac{100 \text{ Å}}{EW}\right] \text{ erg cm}^{-2} \text{s}^{-1} \text{Å}^{-1}.$$
$$(3.35)$$

A2 Converting from UV radiation to Raman scattering wing

In our simulations, far UV continuum photons around Lyβ and Lyγ are generated and subsequently injected into neutral region to investigate the formation of Raman wings around Hα and Hβ. Because the incident far UV continuum level in the simulation is also presented in unit of Å^{-1} just like the normalized flux around Hα and Hβ discussed above, we discuss the conversion of the continuum level into the physical unit of $\text{erg cm}^{-2} \text{ s}^{-1} \text{ Å}^{-1}$.

Raman scattering relocates a far UV continuum photon into a Balmer wing region. The relocation involves the factor $(\lambda_o/\lambda_i)^2 \simeq 40$ between the wavelength space near Lyβ and that near Hα. That is, a continuum interval of size $d\lambda_i$ around Lyβ is *"Raman-transformed"* onto an interval around Hα of size $d\lambda_o \simeq 40 \ d\lambda_i$. In addition, another factor of λ_o/λ_i should be considered because an Hα photon is less energetic than a Lyβ photon by the same factor.

Therefore, the incident continuum flux (ICF) around Lyβ in unit of Å^{-1} (i.e., $ICF_{Ly\beta} = 1 \ \text{Å}^{-1}$) is amplified by the factor $(\lambda_o/\lambda_i)^3 \simeq 250$ compared to $NF_{H\alpha}$ in Eq. 3.33. In the case of $F_{H\alpha} = 2 \times 10^{-10} \text{ erg s}^{-1} \text{ cm}^{-2}$, the unit value of ICF around Lyβ is converted into a physical unit of $\text{erg cm}^{-2} \text{s}^{-1} \text{Å}^{-1}$

as follows

$$ICF_{Ly\beta} = 1 \text{ Å}^{-1} \iff 5\times10^{-10} \left[\frac{PV-CL}{100 \text{ Å}^{-1}}\right] \left[\frac{CL}{1 \text{ Å}^{-1}}\right] \left[\frac{100 \text{ Å}}{EW}\right] \text{ erg cm}^{-2}\text{ s}^{-1}\text{ Å}^{-1}.$$

(3.36)

Here, PV, CL and EW are the parameters of the Hα line presented in Table 3.2.

Similarly the factor of $(4850/972)^3 \sim 100$ is involved in the wavelength space near Lyγ and that around Hβ. Adopting Eq. (3.35), $ICF_{Ly\gamma}$ is

$$ICF_{Ly\gamma} = 1 \text{ Å}^{-1} \iff 2\times10^{-10} \left[\frac{PV-CL}{100 \text{ Å}^{-1}}\right] \left[\frac{CL}{1 \text{ Å}^{-1}}\right] \left[\frac{100 \text{ Å}}{EW}\right] \text{ erg cm}^{-2}\text{ s}^{-1}\text{ Å}^{-1}.$$

(3.37)

The Raman wings around Hα shown in Fig. 3.8 are generated with the incident continuum flux $ICF_{Ly\beta} = 3.3 \text{ Å}^{-1}$ and 4.5 Å^{-1} for AG Dra and Z And, respectively. With the normalization of $F_{H\alpha} = 2 \times 10^{-10}$ erg cm^{-2} s^{-1}, the corresponding far UV continuum around Lyβ would be 2.7×10^{-10} erg cm^{-2} s^{-1} Å^{-1} and 3.4×10^{-10} erg cm^{-2} s^{-1} Å^{-1} for AG Dra and Z And, respectively. Similarly for the Raman wings around Hβ shown in Fig. 3.8, $ICF_{Ly\gamma} = 7.4 \text{ Å}^{-1}$ and 5.4 Å^{-1} for AG Dra and Z And, respectively, which are converted into 1.3×10^{-11} erg cm^{-2} s^{-1} Å^{-1} and 2.0×10^{-11} erg cm^{-2} s^{-1} Å^{-1}.

Chapter 4

Formation of Raman

Scattering Wings around Hα,

Hβ and Paα in Active Galactic

Nuclei

4.1   Introduction

Active galactic nuclei (AGNs) are known to be powered by a supermassive
black hole with an accretion disk. The spectra of AGNs are characterized by
a nonthermal featureless continuum with prominent emission lines exhibiting
a large range of ionization and excitation (e.g., Peterson 1997). One classi-

fication of AGNs can be made based on the width of emission lines. Type 1 AGNs show broad permitted lines and semi-forbidden lines with a typical width of $5,000$ km s^{-1}. In addition to these broad emission lines they also show narrow forbidden lines with a width ~ 500 km s^{-1}. In contrast to this, type 2 AGNs exhibit only narrow emission lines encompassing both permitted and forbidden lines.

Blandford & McKee (1982) proposed that the location of the broad line region can be observationally constrained by monitoring the flux of emission lines that vary in response to the changes of continuum flux. The time delay is directly translated into the size of the broad emission line region, which is also used to estimate the mass of the black hole (e.g., Bentz et al. 2009; Park et al. 2012). The reverberation mapping shows that the broad emission line region is located within ~ 0.1 pc from the central engine, whereas the narrow emission lines do not exhibit flux variations correlated with the neighboring continuum (e.g., Peterson & Brandley 1993; Dietrich et al. 2012). A typical AGN unification model proposes that an optically and geometrically thick component resides between the broad emission line region and the narrow emission line region, hindering the observers in the equatorial direction from viewing the broad line region.

Spectropolarimetry can be an efficient tool to verify this unification scheme, because we expect the broad emission lines may be seen in the po-

larized spectra in the presence of a scattering medium in the polar direction (e.g., Antonucci 1993). The prototypical type 2 Seyfert galaxy, NGC 1068, shows broad Balmer lines in the polarized flux (e.g., Antonucci & Miller 1985). A similar observation was made for the narrow line radio galaxy Cyg A by Ogle et al. (1997), in which an extremely broad Hα line was found in the polarized flux.

Broad absorption line quasars (BALQs), constituting about 10 percent of quasars, exhibit broad absorption troughs in the blue part of permitted broad lines. The exact nature of the absorbing media being controversial, one suggestion is that broad absorption lines are formed in the equatorial outflow that is driven radiatively by quasar luminosity (e.g., Murray & Chiang 1995). In this case the broad troughs will not be completely black but filled partially by photons resonantly scattered in other lines of sight (e.q., Lee & Blandford 1997). Spectropolarimetry is also applied to find polarized residual fluxes in the broad absorption troughs in a number of BALQs (e.g., Cohen et al. 1995).

In the presence of an optically thick component, it is expected that far UV radiation can be inelastically scattered by neutral hydrogen, which may result in scattered radiation in the visible and IR regions. Raman scattering by atomic hydrogen was first introduced by Schmid (1989), when he identified the broad features around 6825 Å and 7082 Å. These mysterious broad

features are found in about half of symbiotic stars, wide binary systems consisting of an active white dwarf and a mass losing giant (e.q., Kenyon 1986). The broad 6825 and 7082 emission features are formed through Raman scattering of O VI$\lambda\lambda$1032 and 1038, when the scattering hydrogen atom in the ground state before incidence finally de-excites to the $2s$ state.

The cross sections of Raman scattering for O VI$\lambda\lambda$1032 and 1038 are $6.6\sigma_{Th}$ and $2.0\sigma_{Th}$, respectively, where $\sigma_{Th} = 0.665\times10^{-24}$ cm^2 is the Thomson scattering cross section. Due to the small scattering cross section, the operation of Raman scattering by atomic hydrogen requires a large amount of neutral hydrogen that is illuminated by the far UV emission source. However, the cross section increases sharply as the incident wavelength approaches those of Lyman series transition of hydrogen due to resonance.

The energy conservation requires the wavelength λ_o of the Raman scattered radiation to be related to the incident wavelength λ_i by

$$\lambda_o^{-1} = \lambda_i^{-1} - \lambda_\alpha^{-1}, \tag{4.1}$$

where λ_α is the wavelength of Lyα. This relation immediately leads to the following

$$\frac{\Delta\lambda_o}{\lambda_o} = \frac{\lambda_o}{\lambda_i}\frac{\Delta\lambda_i}{\lambda_i}, \tag{4.2}$$

which dictates that the Raman features have a large width broadened by the factor λ_o/λ_i. In the case of Raman scattering of O VIλ1032, $\lambda_o/\lambda_i \simeq 6.6$

which explains the abnormally broad width exhibited in the Raman O VIλ6825 feature.

In a similar way, Raman scattering of continuum photons in the vicinity of Lyβ may form broad features around Hα. This mechanism has been invoked to explain broad Hα wings prevalent in symbiotic stars (Lee 2000; Yoo et al. 2002). Lee & Yun (1998) also discussed polarized Hα through Raman scattering in active galactic nuclei, where neutral regions may be thicker than those found in symbiotic stars.

The next section provides summary of the atomic physics involving Raman scattering by atomic hydrogen. Subsequently we provide our model for computation of broad Balmer and Paschen wings with our simulated results. A brief discussion is provided before conclusion.

4.2 Atomic Physics of Raman Scattering by H I

The exact nature of the thick absorbing component surrounding the broad emission line region in AGNs is still controversial. X-ray observation can be an excellent tool to probe the physical properties of the intrinsic absorber in AGNs. One such study performed using *Suzaku* by Chiang et al. (2013) reported the column density of hydrogen $N_{\mathrm{HI}} \sim 5 \times 10^{23}$ cm^{-2} in the type 2 quasar IRAS 09104+4109. In the presence of this thick neutral hydrogen, the Rayleigh and Raman scattering optical depth for radiation in the vicinity

Lyman series can be quite significant.

The scattering of light by an atomic electron is described by the second order time dependent perturbation theory. We consider an incident photon with angular frequency ω with the polarization vector $\boldsymbol{\epsilon}^{\alpha}$ scattered by an electron in the initial state A, which subsequently de-excites to the final state B accompanied by the emission of an outgoing photon with angular frequency ω' with polarization vector $\boldsymbol{\epsilon}^{\alpha'}$. The energy conservation requires that the difference of the photon energy

$$\hbar(\omega - \omega') = E_B - E_A, \tag{4.3}$$

where E_A and E_B are the energy of the initial and final states A and B, respectively.

Depending on the sign of $E_B - E_A$, the emergent Raman lines are classified into Stokes and anti-Stokes lines. When $E_B - E_A > 0$, we have a Stokes line, which is less energetic than the incident radiation. If $E_B - E_A < 0$, then the transition corresponds to an anti-Stokes line. In this work, all the transitions correspond to Stokes lines.

In this work, no consideration is made of the polarization of Raman wings, which is deferred to a future work.

The cross section for this interaction is given by the Kramers-Heisenberg

formula

$$
\begin{aligned}
\frac{d\sigma}{d\Omega} \;=\;\; & r_0^2 \left(\frac{\omega'}{\omega} \right) \Big| \delta_{AB} \boldsymbol{\epsilon}^{\alpha} \cdot \boldsymbol{\epsilon}^{\alpha'} \\
& - \frac{1}{m_e \hbar} \sum_I \left(\frac{(\mathbf{p} \cdot \boldsymbol{\epsilon}^{(\alpha')})_{BI}(\mathbf{p} \cdot \boldsymbol{\epsilon}^{(\alpha)})_{IA}}{\omega_{IA} - \omega} \right. \\
& \left. \left. - \frac{(\mathbf{p} \cdot \boldsymbol{\epsilon}^{(\alpha)})_{BI}(\mathbf{p} \cdot \boldsymbol{\epsilon}^{(\alpha')})_{IA}}{\omega_{IA} + \omega'} \right) \right|^2 ,
\end{aligned}
\tag{4.4}
$$

where $\omega_{IA} = \omega_I - \omega_A = (E_I - E_A)/\hbar$ is the angular frequency corresponding to the intermediate state I and the initial state A (e.g. Sakurai 1967). The intermediate state I covers all the bound states np and free states $n'p$, where n' is the positive real number. Here, $r_0 = e^2/(m_e c^2) = 2.82 \times 10^{-13}$ cm is the classical electron radius with m_e and e being the electron mass and charge. Note that the summation in the formula consists of a summation over infinitely many np states and an integral over continuous free states $n'p$. Adopting the atomic units where $\hbar = e = m_e = 1$, we note that

$$
E_n = \omega_n = -\frac{1}{2n^2}
\tag{4.5}
$$

for a bound state np and

$$
E'_n = \omega_{n'} = \frac{1}{2n'^2}
\tag{4.6}
$$

for a free state $n'p$.

In this work, we make no consideration on the polarization of Raman wings, which is deferred to a future work. The averaging over the solid angle and polarization states yields a numerical factor of $8\pi/3$, leading to the

Thomson cross section $\sigma_{Th} = 8\pi r_0^2/3$. In the case of Rayleigh scattering, for which the initial and the final states are the same, the cross section can be re-written as

$$
\begin{aligned}
\sigma_{Ray}(\omega) \quad = \quad & \sigma_{Th} \left| \sum_I \left(\frac{\omega <p>_{IA}<p>_{AI}}{\omega_{IA} - \omega} \right. \right. \\
& \left. \left. - \frac{\omega <p>_{IA}<p>_{AI}}{\omega_{IA} + \omega} \right) \right|^2
\end{aligned} \tag{4.7}
$$

(e.g. Sakurai 1967, Bach & Lee 2014).

The bound state radial wavefunction is written as

$$
\begin{aligned}
R_{nl}(r) \quad = \quad & \frac{2}{n^{l+2}(2l+1)!} \left[\frac{(n+l)!}{(n-l-1)!} \right]^{1/2} (2r)^l e^{-r/n} \\
& \times F(-n+l+1, 2l+2, 2r/n),
\end{aligned} \tag{4.8}
$$

where $F(\alpha, \beta, z)$ is the hypergeometric function defined by

$$
F(\alpha, \beta, z) = 1 + \frac{\alpha}{\beta} \frac{z}{1!} + \frac{\alpha(\alpha+1)}{\beta(\beta+1)} \frac{z^2}{2!} + \cdots . \tag{4.9}
$$

For a free state $|n'l>$, the radial wavefunction is written as

$$
\begin{aligned}
R_{n'l}(r) = & \frac{2n'^{1/2}}{[1 - e^{-2\pi n'}]^{1/2} (2l+1)!} \prod_{s=1}^{l} \left(1 + \frac{s^2}{n'^2} \right)^{1/2} \\
& \times (2r)^l e^{-ir/n'} F(in'+l+1, 2l+2, 2ir/n')
\end{aligned} \tag{4.10}
$$

with the normalization condition

$$
\int_0^\infty R_{n'l}(r) R_{n''l}(r) r^2 dr = \delta(n' - n'') \tag{4.11}
$$

(e.g. Bethe & Salpeter 1957, Saslow & Mills 1969).

Table 4.1: Matrix elements of the momentum operator p in atomic units.

Matrix	Element
$<2s\|p\|np> \ =$	$-i32\sqrt{2}n^{3/2}(n^2-1)^{1/2}(n^2-4)^{-2}[(n-2)/(n+2)]^n$
$<2s\|p\|n'p> \ =$	$-i32\sqrt{2}n'^{3/2}(n'^2+1)^{1/2}(n'^2+4)^{-2}(1-e^{-2\pi n'})^{-1/2}e^{-2n'\tan^{-1}(2/n')}$
$<3s\|p\|np> \ =$	$-i24\sqrt{3}n^{3/2}(n^2-1)^{1/2}(17n^2-27)(n^2-9)^{-3}[(n-3)/(n+3)]^n$
$<3s\|p\|n'p> \ =$	$-i24\sqrt{3}n'^{3/2}(1+n'^2)^{1/2}(7n'^2+27)(1-e^{-2\pi n'})^{-1/2}(n'^2+9)^{-3}e^{-2n'\tan^{-1}(3/n')}$
$<3d\|p\|np> \ =$	$-i96\sqrt{3}n^{11/2}(n^2-1)^{1/2}(n^2-9)^{-3}[(n-3)/(n+3)]^n$
$<3d\|p\|n'p> \ =$	$-i96\sqrt{3}n'^{11/2}(1+n'^2)^{1/2}(1-e^{-2\pi n'})^{-1/2}(n'^2+9)^{-3}e^{-2n'\tan^{-1}(3/n')}$

With these expressions of the radial wavefunctions the explicit expression for relevant matrix elements between the $1s$ state and an np bound state is given by

$$<np|p|1s> = -i\left[\frac{2^6n^3(n-1)^{2n-3}}{(n+1)^{2n+3}}\right]^{1/2}. \qquad (4.12)$$

Between a free $n'p$ state and the ground $1s$ state the matrix element is given by

$$<n'p|p|1s> = -i\left[\frac{2^6n'^3(1-e^{-2\pi n'})^{1/2}}{(n'^2+1)^3e^{2n'\tan^{-1}(1/n')}}\right]^{1/2}. \qquad (4.13)$$

In the case of Raman scattering where $A \neq B$, the Kronecker delta term vanishes in Eq.(4.4) leaving the two summation terms which contribute to the cross section. The relevant matrix elements are $<np|p|2s>, <np|p|3s>$ and $<np|p|3d>$ and their free state counterparts, which are listed in Table 1.

The total scattering cross section σ_{tot} is given by the sum of the Rayleigh and Raman scattering cross sections. The number of Raman scattering branching channels differs depending on the frequency of the incident photon. For
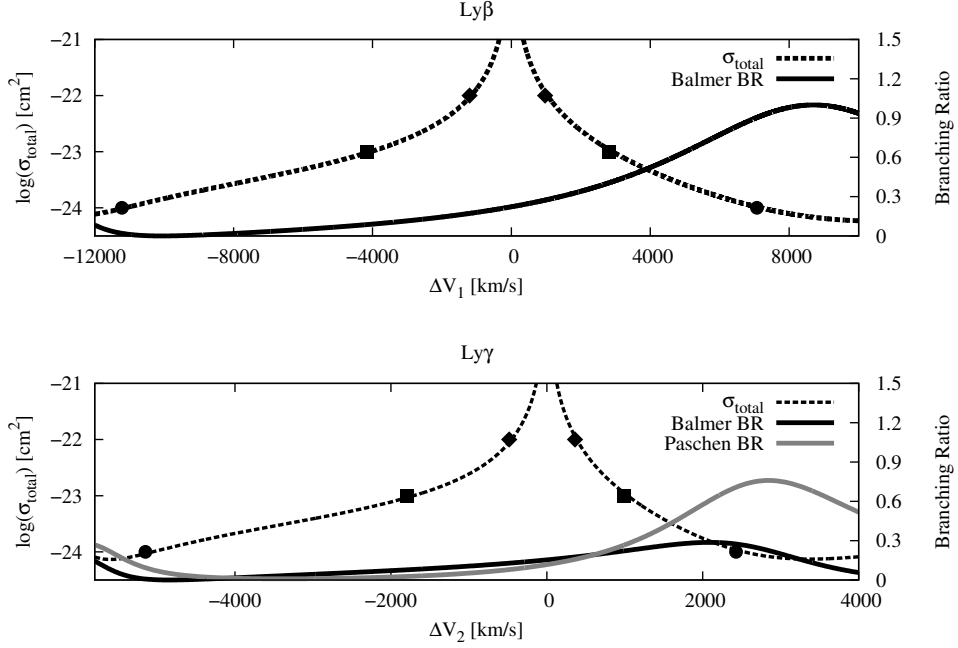
Figure 4.1: Total scattering cross section and branching ratios around $Ly\beta$ (upper panel) and $Ly\gamma$ (lower panel). The solid lines are the sum of cross sections of Rayleigh scattering and Raman scattering. The dotted lines are the branching ratio of scattering into the $2s$ state and the thin gray line shows the branching ratio into the $n = 3$ levels. Note that for $\lambda \geq 974.48$ Å the branching ratio into $n = 3$ is larger than that into $n = 2$.

example, the final states of H I for incident photons blueward of $Ly\beta$ may include $1s$, $2s$, $3s$ and $3d$ states, whereas only $1s$ and $2s$ states can be the final state for those redward of $Ly\beta$ and blueward of $Ly\alpha$.

In Fig. 4.1, we show the total scattering cross section σ_{tot} by a dotted line. We also show the branching ratio into $2s$ by a thick solid line and the branching ratio into $n = 3$ states yielding $Pa\alpha$ wings by a thin gray line.

We define the Doppler velocity factor ΔV_1 around Lyβ by

$$\Delta V_1 = \frac{\lambda - \lambda_\beta}{\lambda_\beta} c \qquad (4.14)$$

where λ_β is the wavelength of Lyβ. In terms of ΔV_1 we find the total scattering cross section exceeding 10^{-22} cm^2 in the range $-1,264$ km s$^{-1} < \Delta V_1 < +930$ km s^{-1}. As Lee (2013) pointed out the total cross section is stronger in the blue side than the red side around Lyβ. The range of ΔV_1 corresponding to $\sigma_{\text{tot}} \geq 10^{-23}$ cm^2 is $-4,162$ km s$^{-1} < \Delta V_1 < +2,805$ km s^{-1}.

In a similar way, we introduce the Doppler factor ΔV_2 defined as

$$\Delta V_2 = \frac{\lambda - \lambda_\gamma}{\lambda_\gamma} c \qquad (4.15)$$

where λ_γ is the wavelength of Lyγ. For radiation in the vicinity of Lyγ the velocity range for $\sigma_{\text{tot}} \geq 10^{-22}$ cm^2 is given by -553 km s$^{-1} < \Delta V_2 < 281$ km s^{-1}. When we increase the column density to $N_{\text{HI}} = 10^{23}$ cm^{-2}, the velocity range corresponding to the total optical depths exceeding unity is $-1,809$ km s$^{-1} < \Delta V_2 < +934$ km s^{-1}. In the vicinity of Lyγ, the total cross sections are also asymmetric showing larger values in the blue part than in the red part. This trend is similar to that around Lyβ. Furthermore, the branching ratio of scattering into the $2s$ state is also increasing as a function of the wavelength. In particular, the branching ratio into $n = 3$ in Fig. 4.1 is larger than that into $n = 2$ for $\lambda \geq 974.48$ Å. This implies that in

the red part of Lyγ with incident wavelength $\lambda \geq 974.48$ Å we expect more Raman scattered photons redward of Paα than those redward of Hβ.

In Table 2 we summarize these values for neutral column densities ranging from 10^{22} cm^{-2} to 10^{24} cm^{-2}. As is shown in the table, the velocity widths are significantly larger around Lyβ than around Lyγ. The Raman wing width is obtained roughly from this width in the parent wavelength space multiplied by the numerical factor $(\lambda_o/\lambda_i)^2$ due to the inelasticity of scattering. The latter factor is the largest for Paα wings and smallest for Hβ wings. From this we may expect that the extent of Hβ wings will be much smaller than that of Paα wings. The branching ratio into $n = 3$ states being comparable to that into $n = 2$ around Lyγ, the Paα wings will be much broader but shallower than the Hβ counterparts.

The total scattering optical depth of unity for $N_{\mathrm{HI}} = 10^{23}$ cm^{-2} is obtained for incident radiation with wavelengths $\lambda_{\beta 1} = 1011.83$ Å, $\lambda_{\beta 2} = 1035.69$ Å around Lyβ. These photons are Raman scattered to appear at 6047 Å, and 7012 Å around Hα.

In a similar way, we have the total scattering optical depth of unity at $\lambda_{\gamma 1} = 966.99$ Å, $\lambda_{\gamma 2} = 975.90$ Å around Lyγ, for which Raman scattered features reappear at 4735 Å and 4956 Å around Hβ and at 16890 Å and 20090 Å around Paα.

N_{HI}	λ_1	ΔV_1	λ_2	ΔV_2
[cm^{-2}]	[Å]	[km s^{-1}]	[Å]	[km s^{-1}]
10^{22}	1021.75, 1029.27	-1264, $+930$	971.07, 973.78	-553, $+281$
$10^{22.5}$	1018.37, 1031.76	-2253, $+1657$	969.74, 974.62	-960, $+539$
10^{23}	1011.83, 1035.69	-4162, $+2805$	966.99, 975.90	-1809, $+934$
$10^{23.5}$	1000.30, 1041.51	-7530, $+4506$	961.69, 977.75	-3443, $+1505$
10^{24}	987.68, 1050.29	-11218, $+7069$	956.14, 980.74	-5151, $+2427$

Table 4.2: Wavelengths and the corresponding Doppler factors having a unit total scattering optical depth for various values of neutral hydrogen column density N_{HI}. The two values of λ_1 and those of λ_2 are wavelengths around Lyβ and Lyγ, respectively. The Doppler factors ΔV_1 and ΔV_2 are defined by Eq. (4.14) and Eq. (4.15), respectively.

4.3 Monte Carlo Radiative Transfer

We consider a neutral scattering region as a finite cylinder characterized by the thickness and the height. The symmetry axis is chosen to be z axis and the AGN continuum source is assumed to reside at the center of the coordinate system.

The AGN continuum is known to be nonthermal and typically approximated by a power law (e.g., Zheng al. 1997; Vanden Berk et al. 2001). It also appears that far UV continuum spectrum around Lyβ and Lyγ is almost flat in many AGNs. In this respect the continuum considered in this work is described by

$$\lambda F_\lambda = \lambda_0 F_0 \left(\frac{\lambda}{\lambda_0}\right)^\alpha,\qquad(4.16)$$

where the spectral index α is set to zero in this work, and λ_0 is a characteristic wavelength in this spectral region.

CHAPTER 4. FORMATION OF RAMAN WINGS IN AGN

Spectropolarimetry of the prototypical Seyfert 2 galaxy NGC 1068 performed by **?** shows that Hβ appears broad in the polarized flux. This implies that NGC 1068 possesses the broad line region that is hidden from the observer's line of sight by an optically thick torus-like region. Almost constant position angle in the polarized flux is consistent with the scattering region located in the polar direction with respect to the central engine.

In performing our simulations it is assumed that the far UV incident radiation does not affect the physical and chemical conditions of the neutral scattering region. With this assumption, the Rayleigh-Raman radiative transfer of far UV continuum can be divided coceptually into radiative transfer of each individual photon with a definite frequency that constitutes the whole far UV continuum.

Compared with usual Raman spectroscopy performed in a lab with a monochromatic laser with a definite polarization state, our simulation of Raman scattering by atomic hydrogen in AGN differs mainly in our neglect of polarization. As far as no measurement is made of the polarization of the final emergent photon, the radiative transfer using Eq. (7) for unpolarized light is equivalent to obtaining the total number flux of Raman scattered radiation from simulations that take a full consideration of polarization. With these limitations noted, we simulate the Raman wing formation by injecting an unpolarized individual photon with a definite frequency. The number of
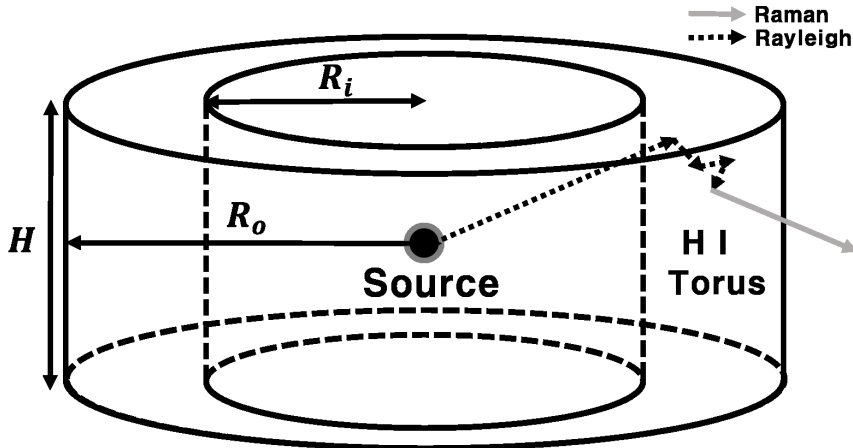
Figure 4.2: Scattering geometry of AGNs, where the neutral scattering region is considered to be a cylindrical torus with R_i, R_o and H being the inner radius, outer radius and the height.

these photons is determined in an accordance of AGN comtinuum spectrum.

Additional information regarding the existence of the optically thick component can be obtained from studies of X-ray hardness of AGNs. Because soft X-rays suffer more severe extinction than hard X-rays, type 2 AGNs tend to exhibit larger X-ray hardness than type 1 AGNs. X-ray studies show that the optically thick component is characterized by a hydrogen column density ranging 10^{22-24} cm^{-2}.

In this work we place an optically thick component in the form of a cylindrical torus with a finite height, which is schematically shown in Fig. 4.2. This torus is specified by the inner radius R_i, the outer radius R_o and the height H. For the sake of simplicity, we fix the thickness of the torus $\Delta R = R_o - R_i = 10\,\mathrm{pc}$ and we assume that the number density of neutral hydro-

gen n_{HI} is uniform in the scattering region. In this case, the scattering region can be specified by the lateral column density $N_{\text{HI}} = n_{\text{HI}}\Delta R$. The height H is parameterized by $A = H/\Delta R$, the ratio of the height and the thickness ΔR. In this work, we vary A between 0.5 and 2 and also consider N_{HI} in the range 10^{22-24} cm^{-2}.

The Monte Carlo simulation starts with the generation of a far UV continuum photon from the central engine, which subsequently enters the scattering region. The wavelength of the incident photon is determined in accordance with the power law of the AGN continuum given in Eq. (4.16). For this wavelength we rescale the scattering geometry in terms of the total scattering optical depths $\tau_R = \sigma(\lambda)n_{\text{HI}}\Delta R$ and $\tau_H = \sigma(\lambda)n_{\text{HI}}H$.

To determine the first scattering site we compute the optical depth τ for this photon given by

$$\tau = -\ln R, \qquad\qquad (4.17)$$

where R is a random number uniformly distributed in the interval [0,1].

According to the branching ratio we determine the scattering type. If the scattering is Rayleigh, then we look for the next scattering site by taking another step given by Eq. (4.17). If the branching is into $n = 2$ or $n = 3$ states, then we have a Raman scattered photon which is supposed to escape from the region immediately. Both Rayleigh scattering and Raman scattering share the scattering phase function which is also identical with that of

the Thomson scattering and therefore we choose the direction of the scattered photon in accordance with the Thomson phase function (e.g., Yoo et al. 2002; Schmid 1989; Nussbaumer et al. 1989).

The collection of Raman scattered photons emergent from the neutral region is made by taking into consideration the difference between the observed wavelength space and the parent far UV wavelength space. The Raman wavelength interval $\Delta\lambda_o$ corresponding to a fixed wavelength interval $\Delta\lambda_i$ of the incident radiation varies with λ_i in accordance with Eq. (4.2). In terms of λ_i this relation can be recast in the form

$$w_{\lambda_o}(\lambda_i) = \frac{\Delta\lambda_i}{\Delta\lambda_o} = \left(1 - \frac{\lambda_i}{\lambda_\alpha}\right)^2. \qquad (4.18)$$

This is the factor that relates the number flux per unit wavelength in the parent wavelength space to that in the observed (Raman scattered) wavelength space, which is multiplied to the Monte Carlo simulated flux for proper normalization.

4.4 Monte Carlo Simulated Raman Wings

4.4.1 Balmer and Paschen Wings Formed through Raman Scattering

In Fig. 4.3, we show the Monte Carlo simulated wings around Hα, Hβ and Paα formed through Raman scattering of far UV radiation from the cen-
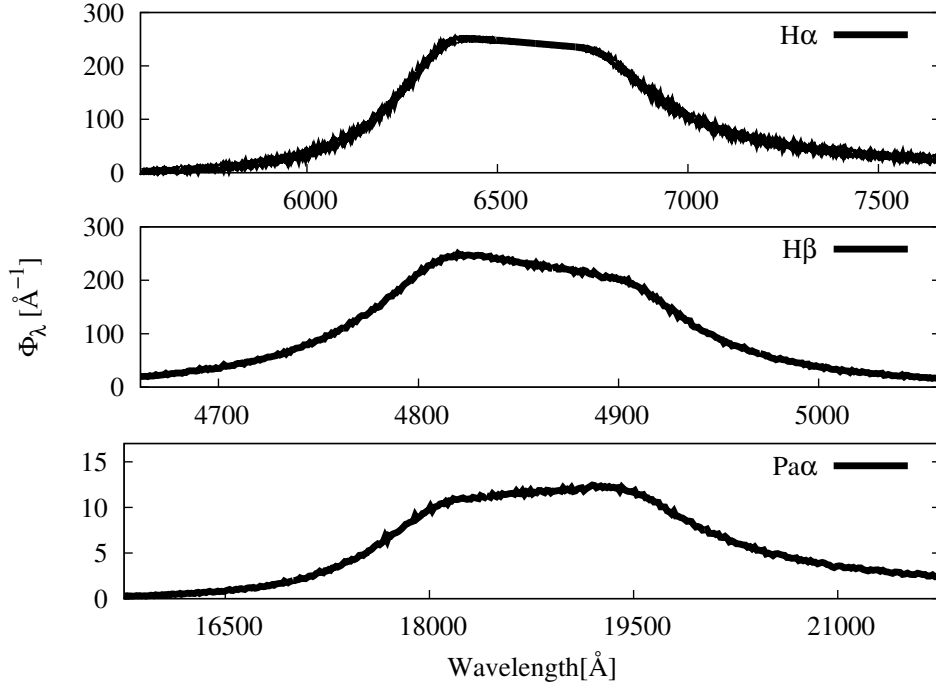
Figure 4.3: Monte Carlo simulated profiles of Raman scattered radiation. The upper panel show the Raman scattering wings around Hα, Hβ and Paα (upper, middle and bottom panel, respectively). The neutral scattering region is assumed to be a slab with finite thickness and infinite lateral dimensions. The far UV source is located in the midplane.

tral engine. The parameters associated with the scattering region are $\Delta R = 10$ pc and $H = \infty$, so that the far UV source is immersed at the center of a cylinder with an infinite height. This choice of $H = \infty$ allows us to study the basic properties of Raman wings without complicating effects due to finite covering factors.

We set the neutral hydrogen column density $N_{HI} = n_{HI}\Delta R = 10^{23}$ cm^{-2} in this figure. In this simulation, 10^4 photons are generated per parent wavelength interval of 1 Å. The horizontal axis represents the observed wave-

length. The vertical axis represents the number of photons obtained in the simulation per unit observed wavelength interval $\Delta\lambda_o$.

The profiles of Raman scattered radiation are characterized by the inclined central core part and extended wing part that declines to zero. The inclined central part is formed from far UV photons with the total scattering optical depth exceeding ~ 10. Roughly speaking, all the far UV photons within these ranges undergo multiple Rayleigh scattering processes before being converted to optical photons around the Balmer emission centers or IR photons around Paα. The Raman number flux near Hα core decreases redward due to the wavelength space factor given in Eq. (4.18), which is a decreasing function of λ_i. The Raman flux around Hβ shows more steeply inclined core part than that around Hα. This is explained by the fact that as λ_i increases the number of photons channeled into the Paα branch increases very steeply reducing the Hβ flux.

However, far UV photons outside these ranges will be scattered at most once to escape from the scattering region either as far UV photons or as Raman scattered photons. For incident far UV radiation with small scattering optical depths the resultant wing profile will be approximately proportional to the product of the total optical depth and the branching ratio, which is in turn approximately given by the Lorentzian. As Lee (2013) pointed out, the cross section and the branching ratios are complicated functions of wave-

length, for which a quantitative investigation can be effectively performed adapting a Monte Carlo technique.

In Fig. 4.4, we transform the same Monte Carlo data given in Fig. 4.3 to the parent wavelength space in order to check easily the fraction of Raman scattered photons with respect to the incident radiation. The horizontal dotted line show the incident flux taken to be 10^4 photons per unit wavelength interval. The top panel shows the number of Raman scattered radiation around Hα. The core part is flat and coincides with the incident flux, which verifies that the Raman conversion is almost complete.

The mid panel shows Raman scattered Hβ and Paα wings by a black solid line and a gray solid line, respectively. The bottom panel shows the sum of Raman scattered Hβ and Paα, where we recover the flat core part coinciding with the incident radiation. This fact provides confirmation that the Raman conversion is also complete in the vicinity of the Lyγ core. In this figure, it can be seen that more Paα wing photons are obtained than Hβ wing photons for incident wavelength $\lambda > 974.48$ Å, where the branching ratio into $n = 3$ states exceeds that into the $2s$ state.

4.4.2 Asymmetry of Raman Scattering Wings

In this subsection, we quantify the asymmetry in the wing profiles formed through Raman scattering around Hα, Hβ and Paα. One way to do this is
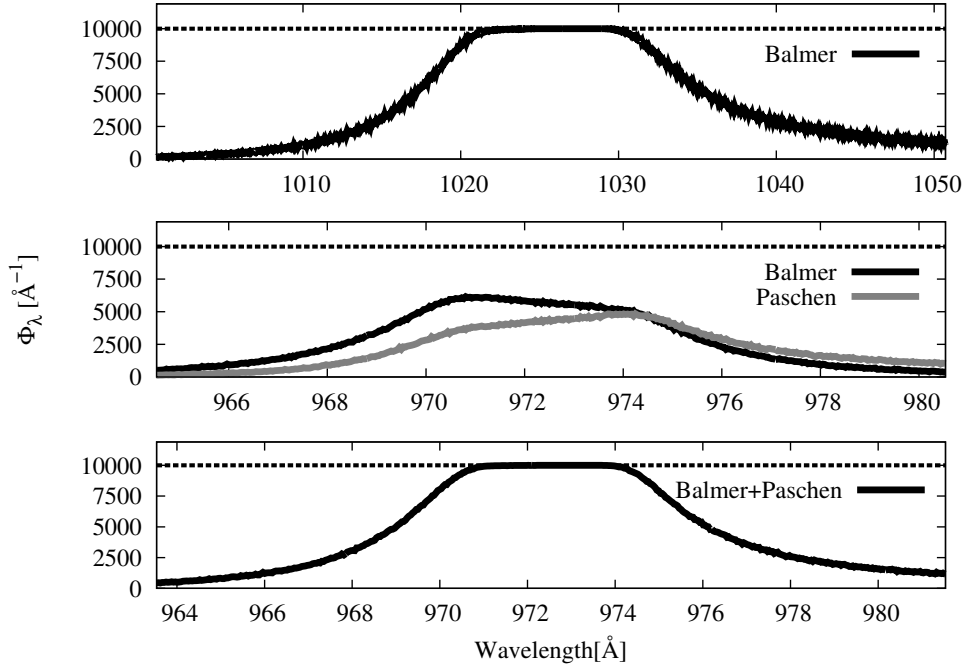
Figure 4.4: Monte Carlo simulated profiles of Raman scattered radiation in the parent wavelength space. The horizontal dotted line shows the incident flux taken to be 10^4 photons per unit wavelength interval. The top panel shows the Raman scattered radiation around Lyβ which shows flat core part because of the complete Raman conversion of the flat incident radiation. The mid panel shows the Raman scattered profiles that appear near Hβ (black lines) and near Paα (gray lines) from the flat UV radiation near Lyγ. The bottom panel shows the sum of Raman scattered fluxes around Hβ and Paα transformed into the parent wavelength space .

N_{HI} cm^{-2}	$\eta_{\mathrm{H}\alpha}$	$\eta_{\mathrm{H}\beta}$	$\eta_{\mathrm{Pa}\alpha}$
10^{22}	0.86	1.13	0.86
$10^{22.5}$	0.81	1.21	0.79
10^{23}	0.73	1.35	0.69
$10^{23.5}$	0.59	1.57	0.55
10^{24}	0.36	1.76	0.37

Table 4.3: The ratio η of the Raman photon number flux blueward of line center to that redward of line center in Fig. 4.3.

to compute the ratio η of the number of Raman photons blueward of line center to that redward of line center. In Table 3 we show our result.

In the case of Hα, the red wing part extends further away from the Hα center than the blue wing, which is clearly seen by the fact that $\eta_{\mathrm{H}\alpha}$ is less than 1. This phenomenon is mainly due to the higher branching ratio for photons redward of Lyβ than their blue counterparts. A similar behavior is also observed for the Paα wings due to increasing branching ratio redward of Lyγ.

However, in the case of Hβ we note that $\eta_{\mathrm{H}\beta}$ exceeds unity implying that the blue wing is stronger than the red part. This behavior is attributed to the much stronger total cross section in the blue part than in the red part near Lyγ, despite the slow increase of the branching ratio as wavelength.

Another way of investigating asymmetry is to identify the half-value locations from a reference Raman flux value. Taking the simulated Raman flux per unit wavelength at the Hα line center as a reference value, the half values appear at $-11,900$ km s^{-1} and $+12,800$ km s^{-1}. A similar analysis for Hβ wings shows that the corresponding Doppler factors are $-4,330$ km s^{-1} and $+3,500$ km s^{-1}. Paα wings are much wider and the Doppler factors corresponding to the half-core values are $-13,500$ km s^{-1} and $+17,000$ km s^{-1}.
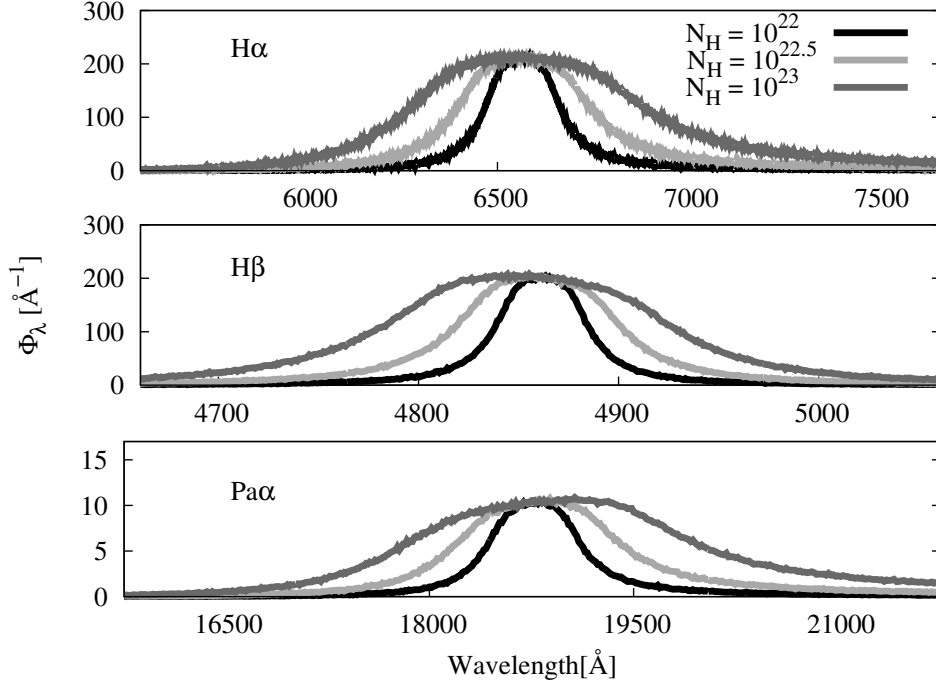
Figure 4.5: Monte Carlo simulated profiles of Raman scattered radiation around Hα, Hβ and Paα (upper, middle and bottom panel, respectively) for various column densities N_{HI} ranging from 10^{22} cm^{-2} to 10^{23} cm^{-2}. As N_{HI} increases, the wing profile broadens in roughly proportional to $N_{HI}^{1/2}$.

4.4.3 Dependence on the Scattering Geometry

In Fig. 4.5, we investigate the Balmer and Paschen wings that are simulated for various values of N_{HI}. In this figure, we set $R_i = 10$ pc and $H = R_o = 20$ pc. We vary the number density of H I in such a way that the neutral column density N_{HI} in the lateral direction becomes 10^{22}, $10^{22.5}$ and 10^{23} cm^{-2}.

Because the covering factor of the neutral scattering region is fixed and the total scattering optical depth is very large near line core, the Raman
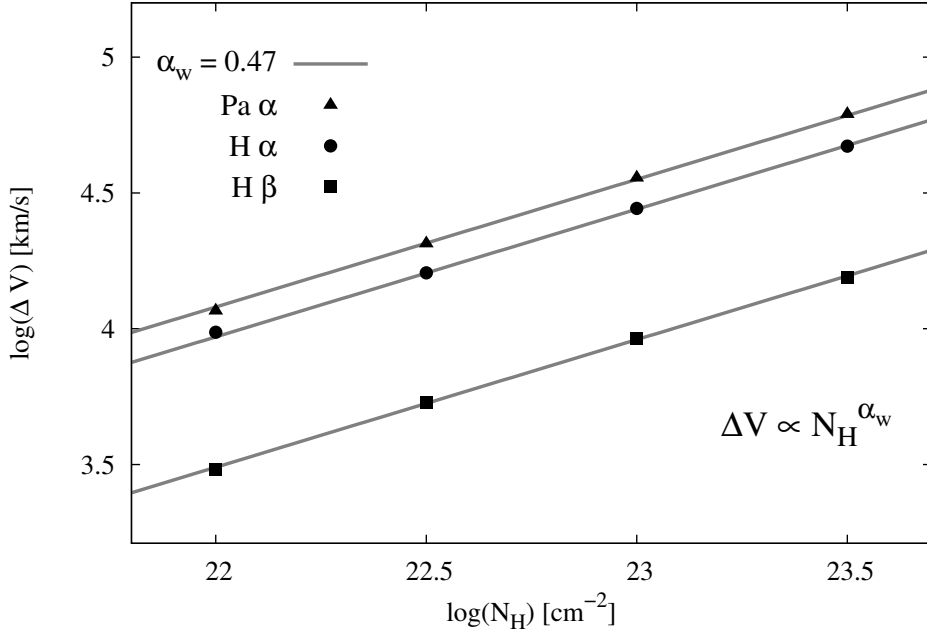
Figure 4.6: Widths of Monte Carlo simulated Raman wings around Hα, Hβ and Paα considered in Fig. 4.5. The horizontal and vertical axes represent the column density and the wing width, respectively. Both axes are in logarithm scale. The dots are measured values from the Monte Carlo simulation and the fitting lines have a slope of 0.47.

flux at line center remains the same for various values of N_{HI}. The primary effect of varying N_{HI} is the width of the Raman wings, in that the width is roughly proportional to $N_{\mathrm{HI}}^{1/2}$. As N_{HI} increases, the saturated part also extends further away from the line center.

We define the width of Raman wings as the difference of the two Doppler factors that correspond to the half values of the Raman flux at line center. Using this definition, we plot the Raman wing widths for various column densities in Fig. 4.6. Note that both the vertical and the horizontal scales

are logarithmic. The Monte Carlo simulated data are shown by the dots that are fitted by lines having a slope of 0.47. In terms of the parameter $N_{23} = N_{\text{HI}}/(10^{23} \text{ cm}^{-2})$ the fitting lines are explicitly written as

$$\Delta V_{\text{H}\alpha} = 2.75 \times 10^4 \ N_{23}^{0.47} \text{ km s}^{-1}$$

$$\Delta V_{\text{H}\beta} = 9.12 \times 10^3 \ N_{23}^{0.47} \text{ km s}^{-1}$$

$$\Delta V_{\text{Pa}\alpha} = 3.55 \times 10^4 \ N_{23}^{0.47} \text{ km s}^{-1}. \tag{4.19}$$

In order to investigate the effect of the covering factor of the scattering region, we vary the height H of the scattering region with the parameters $R_i = 10$ pc, $R_o = 20$ pc and $N_{\text{HI}} = 10^{23} \text{ cm}^{-2}$ fixed. We show our result in Fig. 4.8 for values of $A = 0.5, 1, 2$ and ∞.

With $A \leq 2$ the wing profiles are smooth. Even though not shown in the figure, we checked that there appears an inclined plateau around line center in each Raman wing for $A \geq 4$, implying the saturation behavior.

As the covering factor increases, more far UV photons are incident into the scattering region leading to stronger Raman scattering wings. When A is small, the Raman wing strength is approximately linearly proportional to A. However if A exceeds 2, the wing strength increases very slowly and approaches a limiting value. Given A we normalize the Hα Raman wing strengths by dividing the total number of Raman Hα wing photons by that for $A = \infty$. The wing strengths for Hβ and Paα are normalized in a simi-
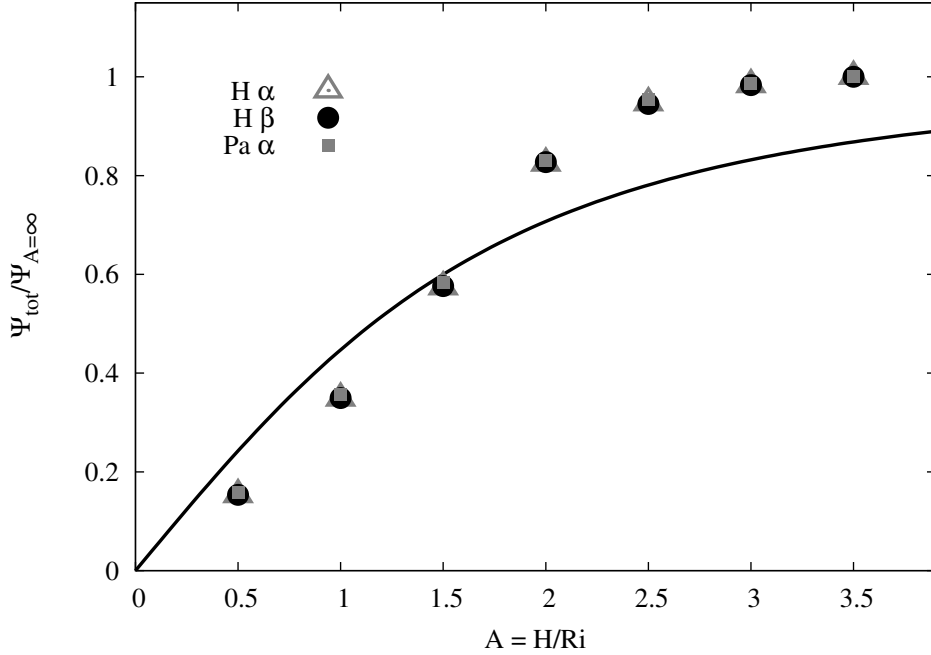
Figure 4.7: Relative strengths of Monte Carlo simulated Raman wings around Hα, Hβ and Paα considered in Fig. 4.8. The vertical axis represents the wing strengths normalized with the Raman wing strength for $A = \infty$. The solid curve shows the covering factor $f(A) = \frac{A}{\sqrt{4+A^2}}$ of the scattering region, whose behavior is also characterized by linearity for small A and approaching unity as $A \to \infty$.

lar way. In Fig. 4.7, we plot the normalized wing strengths for Hα, Hβ and Paα by triangles, circles and squares, respectively. Given A and N_{HI}, the normalized strengths are almost equal to each other for Hα, Hβ and Paα wings. For reference, we add the solid curve to show the covering factor of the scattering region given by

$$f(A) = \frac{A}{\sqrt{4 + A^2}}. \tag{4.20}$$

The covering factor also shows a similar behavior of linearity for small A and
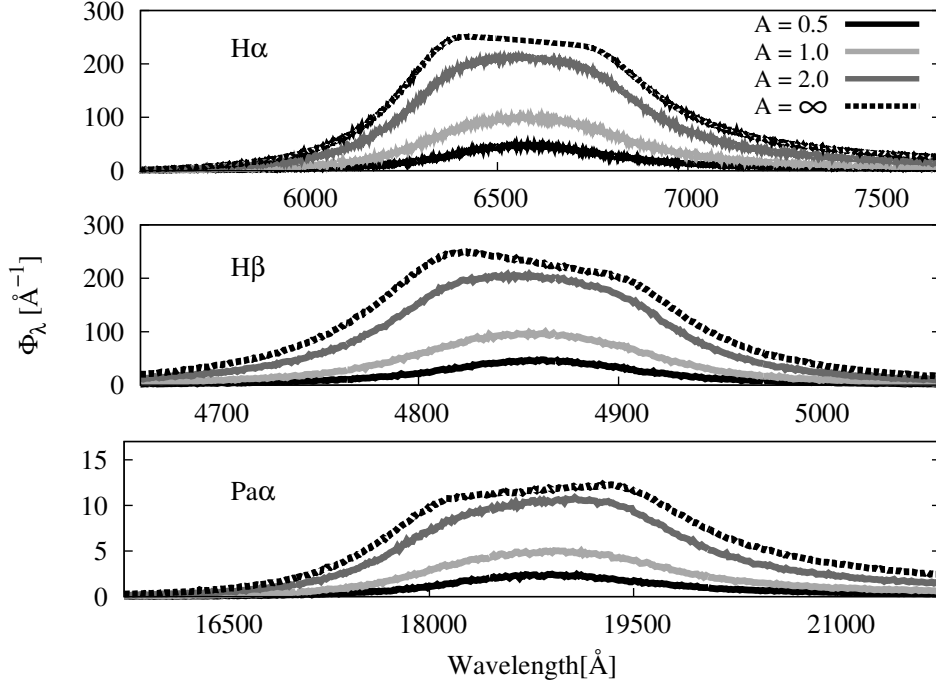
Figure 4.8: Monte Carlo simulated profiles of Raman scattered radiation around Hα, Hβ and Paα (upper, middle and bottom panel, respectively) for various covering factors. $A = H/\Delta R$ is the ratio of the height and the thickness of the cylindrical shell.

approaching unity for large A. Significant deviations between the normalized Raman wing strengths and the covering factor are attributed to complicated effects of multiple scattering and branching channels associated with the formation of Raman wings.

4.4.4 Mock Spectrum around Balmer Lines

In order to assess the observational feasibility we produce a mock spectrum around Balmer lines by superposing the wing profiles onto artificially produced Hα and Hβ broad emission lines. In Fig. 4.9, we show our result.
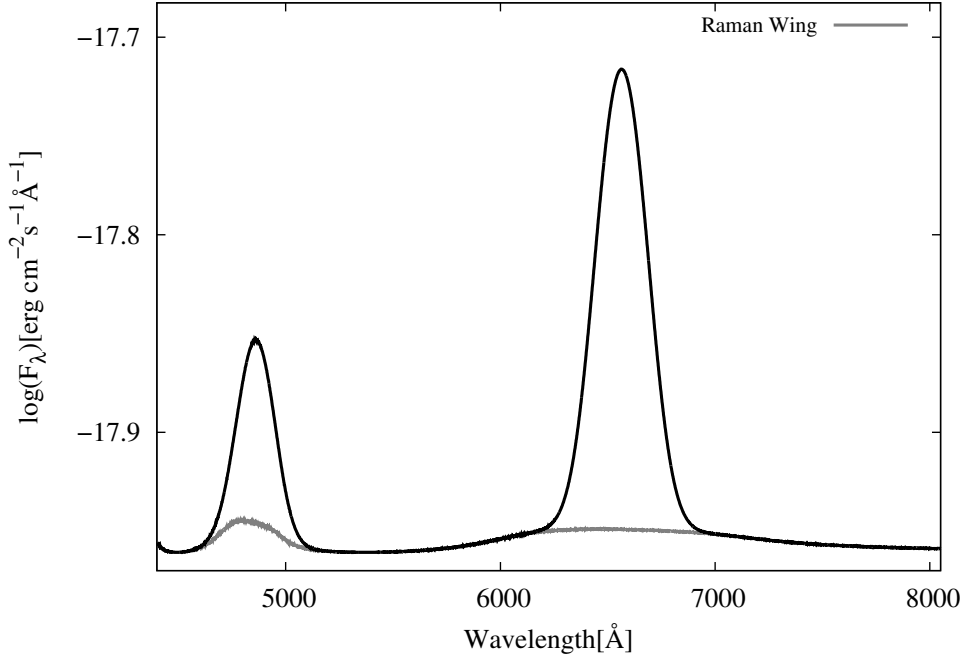
Figure 4.9: Mock composite spectrum around Hα and Hβ with Raman scattering wings. The gray line shows Raman wings generated through a Monte Carlo simulation. The vertical scale is logarithmic for clear view of Raman wings against prominent emission lines.

In the production of the mock spectrum we assumed that the continuum level around Lyβ and Lyγ is given by the fixed value of $\lambda L_\lambda = 10^{44}$ erg s^{-1} and that the continuum between Hβ and Hα is given in such a way that $L_\lambda = 10^{40}$ erg s^{-1}Å^{-1}. We also set the luminosity distance $D_L = 0.3$ Gpc.

With no established line profiles of the Balmer emission lines in AGNs, we take a Gaussian profile of width $5,000$ km s^{-1} for Hα and Hβ emission lines. We set the equivalent widths of Hα and Hβ broad emission lines to be 200 Å and 50 Å, respectively. The scattering geometry is taken so that

$R_i = 10 \, \text{pc}, R_o = 20 \, \text{pc}$ and $H = 20 \, \text{pc}$ with $N_{\text{HI}} = 5 \times 10^{23} \, \text{cm}^{-2}$.

In the figure the vertical scale is logarithmic and the Raman wings are shown by gray solid lines. In the case of Hβ, the Raman wings are inconspicuous because the broad emission component dominates the relatively narrow Raman Hβ wings. However, the Raman Hα wings are sufficiently wide to be observationally detectable. It is an interesting possibility that type 2 AGNs may also show detectable Raman Hβ wings, which will be seen outside of the narrow Hβ emission line.

4.5 Summary and Discussion

In this article we produced Raman wing profiles expected around Hα, Hβ and Paα that are formed by far UV continuum radiation scattered in a thick neutral region surrounding the central engine. The strengths of Raman wings are mainly determined by the product of the covering factor and the neutral column density of the scattering region. The wing width is approximately proportional to $N_{\text{HI}}^{1/2}$. We also provide a mock spectrum by superposing simulated Raman wings onto artificially generated broad emission lines of Hα and Hβ.

Observationally the Raman wings are difficult to discern from the underlying continuum because of their large width. Another issue may be that broad wings can also be formed from Thomson scattering or hot tenuous fast

wind that emits Balmer and Paschen line photons (Kim et al. (2007)). One distinguishing aspect of the Raman wings is the differing widths and profiles exhibited by Hα, Hβ and Paα because of the complicated atomic physics. If the wings are formed in an emission region moving very fast, then all the wings are expected to show similar widths and profiles.

Another important characteristic is the linear polarization because the scattering mechanism is exactly the E-1 process, which also characterizes the Thomson scattering (Trippe (2014)). Ogle et al. (1997) performed spectropolarimetry of the prototypical narrow line radio galaxy Cyg A using the Keck II Telescope, in which they discovered extremely broad Hα in the polarized flux. The full width at half-maximum of polarized Hα is $26,000$ km s^{-1}. If this huge width is attributed to dust scattering or free electron scattering, one may need to assume that the velocity scale of the hidden broad line region is roughly the same value of $26,000$ km s^{-1}. In this case, the relativistic beaming inevitably leads to very asymmetric profiles with the blue part much stronger than the red part.

On the other hand, very broad features around Hα are naturally formed through Raman scattering of far UV radiation without invoking extreme kinematics in the broad emission line region. For example, if we assume that the central engine of Cyg A is surrounded by a cold thick region with $N_{\mathrm{HI}} \sim 10^{23}$ cm^{-2} the width of $26,000$ km s^{-1} can be explained. In this case, we

have to assume that the continuum around Lyγ is relatively weak compared to that around Lyβ in order to explain no detection of the polarized broad features around Hβ. In particular, it is highly noticeable that Reynolds et al. (2015) proposed a neutral column density of $\sim 1.6 \times 10^{23}$ cm^{-2} from their observations of *NUSTAR* of Cyg A. Despite the difficulty in identifying the broad wings around H I emission lines from the local continuum, they will provide important clues to the unification model of AGNs.

Chapter 5

Polarization of Rayleigh Scattered Lyα in Active Galactic Nuclei

5.1 Introduction

The spectra of active galactic nuclei (AGNs) are characterized by a nonthermal continuum with prominent emission lines. A huge range of ionization is apparent in the emission line spectra encompassing low ionization species such as Mg IIλ2800 and high ionization lines like O VIλ1034. AGNs are powered by the accretion process around a supermassive black hole forming a geometrically thin but optically thick disk (Blandford et al. 1990). The

emission lines are classified according to their widths where broad lines exhibit a typical width of 10^4 km s^{-1} and narrow emission lines show an order of magnitude smaller width of 500 km s^{-1}.

AGNs are usually classified into two types according to the widths of emission lines. Type 1 AGNs show both broad and narrow emission lines whereas type 2 AGNs exhibit only narrow emission lines. According to unification models of AGNs all AGNs possess a highly thick molecular torus outside the broad emission line region (e.g. Netzer 2015). In these models, the two types of AGNs are interpreted as an orientation effect toward the observer's line of sight. Type I AGNs are those viewed by the observers with the line of sight near the polar direction whereas to the observers near the equatorial direction AGNs are classified as Type 2.

Spectropolarimetry is an important tool in testing the unification models (e.g. Antonucci 1993). In the case of the prototypical Seyfert 2 galaxy NGC 1068, Antonucci & Miller (1985) found the broad Hβ emission in the polarized flux spectrum (see also e.g. Miller & Goodrich 1990, Tran et al. 1999). They interpreted this broad Hβ by assuming the presence of an electron scattering medium in the polar direction that reveals the broad emission line region through Thomson scattering.

Another important test of the unification models is provided by X-ray observations, which reveal that the hardness ratio tends to be systematically

higher for type 2 AGNs than type 1 AGNs. In particular, type 2 AGNs typically show severe extinction in the soft X-ray region, indicating the presence of an absorbing component with hydrogen column density of the order of $N_H \sim 10^{23}$ cm^{-2} (e.g. Ricci et al. 2014). Hard X-ray observations of AGNs also show that Compton thick material with column densities $> 10^{24}$ cm^{-2} may obscure the AGN engines. Compton scattering from high column components is proposed to be an important contributor to the cosmic X-ray background that is characterized by a broad bump at $\sim$ 30 keV (e.g. see Comastri et al. 2015 and Magdziarz et al. 1995). However, the existence and detailed physical conditions of the molecular torus component are only poorly constrained.

As pointed out by Chang et al. (2015), a significant amount of neutral hydrogen that may exist in the hypothetical molecular torus can act as a Rayleigh and Raman scattering medium. The cross section for Rayleigh scattering increases sharply near Lyα due to resonance. This implies that far UV radiation near Lyα can be strongly polarized due to Rayleigh scattering depending on the covering factor and the H I column density of the molecular torus. This leads to an interesting possibility of polarized Lyα to put meaningful constraints on the unification models of AGNs.

Recent detections of polarized Lyα emission from a giant Lyα nebula opens a new window to probe the physical environment of the intergalac-

tic medium illuminated by starbursting galaxies and active galactic nuclei in the early universe. Lyα nebulae, or "blobs," are rare, extended sources at $z = 2$–6 with typical Lyα sizes of 10 ($\sim$100 kpc) and line luminosities of $L_{\mathrm{Ly}\alpha} \sim 10^{44}$ erg s^{-1} (e.g., Steidel et al. 2000; Francis et al. 2001; Matduda et al. 2004; Dey et al. 2005; Nilsson et al. 2006; **?**; **?**; Matsuda et al. 2011; Prescott et al. 2012). Recently, Hayes et al. (2011) discovered a polarization pattern of concentric rings within a Lyα nebula at $z = 3.1$, which supports a central powering mechanism within the nebula. While the physical scale of Lyα nebulae ($\sim$100 kpc) is much larger than that of AGN central engines (~ 1 pc), the basic pictures are the same: Lyα or continuum photons from the central source are resonantly or Rayleigh scattered by the surrounding neutral H I medium. However, theoretical modeling of the Lyα polarization is still in its infancy (Dijkstra & Loeb 2008), and therefore a detailed modeling of Lyα polarization in diverse geometry is required.

We compute, in this paper, the polarization of the far UV radiation around Lyα that is Rayleigh scattered in a thick neutral hydrogen region. The paper is composed as follows. In section 2, we discuss the atomic physics of Rayleigh scattering around Lyα. In the following section, the scattering geometry and our Monte Carlo code are described. The main result is presented in section 3. In section 4 we discuss the observational implications of polarized Lyα in an AGN.
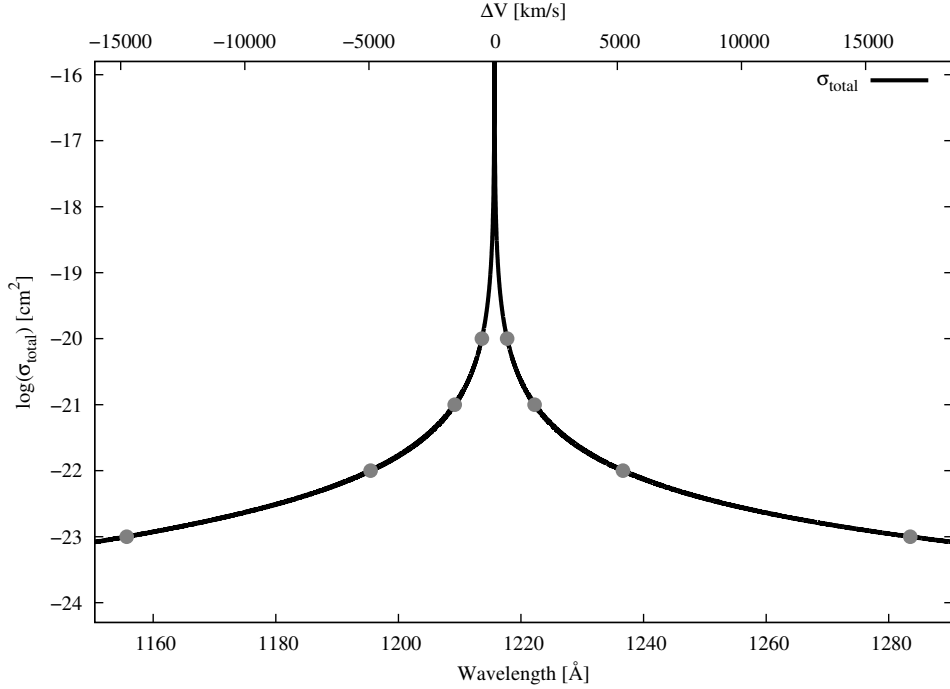
Figure 5.1: Cross section for Rayleigh scattering by atomic hydrogen. The vertical scale is logarithmic, whereas the horizontal axis is wavelength in units of Å. The dots mark the wavelengths having the cross section values of $10^{-20}, 10^{-21}, 10^{-22}, 10^{-23}$ cm^2. The cross section exhibits redward asymmetry as pointed out by Lee (2013).

5.2 Atomic Physics of Rayleigh Scattering

There have been many basic research works on the Rayleigh scattering processes (e.g. Isliker et al. 1989, Gavrila 1967, Sadeghpour & Dalgarno 1992, Lee 2013). The time-dependent second order perturbation theory is used to describe the Rayleigh scattering process. The scattering cross section is given by the Kramers-Heisenberg formula, which can be written as

$$\frac{d\sigma_{Ray}}{d\Omega} = r_0^2 \left| (\epsilon^\alpha \cdot \epsilon^{\alpha'}) \left(\sum_n M^b(n) + \int_0^\infty dn' M^c(n') \right) \right|^2. \qquad (5.1)$$

Here, ϵ^{α} and $\epsilon^{\alpha'}$ are the polarization vectors associated with the incident and outgoing photons, respectively, and r_0 is the classical electron radius. The angular integral over the two polarization states for an incident unpolarized radiation results in the factor of $8\pi/3$, which is in turn multiplied by r_0^2 to yield the Thomson scattering cross section $\sigma_T = 0.665 \times 10^{-24}$ cm^2. In the formula, the matrix elements between the ground $1s$ state and the bound np states are given by

$$M^b(n) = \frac{m\omega^2}{3\hbar}| < 1s \parallel r \parallel np > |^2 \frac{2\omega_{n1}}{\omega_{n1}^2 - \omega^2}, \qquad (5.2)$$

and those between $1s$ and continuum $n'p$ states are given by

$$M^c(n') = \frac{m\omega^2}{3\hbar}| < 1s \parallel r \parallel n'p > |^2 \frac{2\omega_{n'1}}{\omega_{n'1}^2 - \omega^2}. \qquad (5.3)$$

The explicit expressions of the reduced matrix elements can be found in many text books on quantum mechanics (e.g. Berestetskii et al. 1971, Saslow & Mills 1969). —The Rayleigh scattering cross section is shown in Fig. 5.1, where the horizontal axis is wavelength in units of Å and the vertical scale is the logarithm of the cross section in units of cm^2. A useful approximation to the Rayleigh scattering cross section can be also found in Lykins et al. (2015).

In particular, near Lyα, the cross section is dominantly contributed by the first term in the summation leading to an approximation

$$\sigma_{Ray}(\lambda) \simeq \sigma_T \left[\frac{f_\alpha}{(\lambda/\lambda_\alpha) - 1} \right]^2, \qquad (5.4)$$

where $f_\alpha = 0.4162$ is the oscillator strength for the Lyα transition and $\lambda_\alpha = 1215.67\,\text{Å}$ is the Lyα wavelength.

Given a neutral column density N_{HI}, we may consider the scattering band width $\Delta\lambda_R(N_{HI} = \lambda - \lambda_\alpha$ by the wavelength width around Lyα, for which the Rayleigh scattering optical depth exceeds unity. Corresponding to $\Delta\lambda_R(N_{HI}$, we have the Doppler velocity width $\Delta V = c(\lambda - \lambda_\alpha)/\lambda_\alpha$. The requirement $\sigma_{Ray}(\lambda)N_{HI} = 1$ leads to

$$\left(\frac{\Delta V}{c}\right)^2 \simeq \sigma_T N_{HI} c^2 f_{12}^2, \tag{5.5}$$

or numerically

$$\frac{\Delta V}{10^4 \text{ km s}^{-1}} \simeq \left[\frac{N_{HI}}{3 \times 10^{22} \text{ cm}^{-2}}\right]^{1/2}. \tag{5.6}$$

Because the dynamical velocity scale of the broad line region of a typical AGN is about 10^4 km s^{-1}, most of the broad Lyα line photons can be Rayleigh scattered under the assumption that $N_{HI} \geq 3 \times 10^{22}$ cm^{-2}. This velocity scale is much larger than the thermal speed of typically photoionized emission nebulae, no consideration is made of resonance scattering of Lyα in this work (e.g. Dijkstra & Loeb 2008).

The dots in Fig. 5.1 correspond to those wavelengths with Rayleigh scattering optical thickness τ_s from 0.1 to 100 for H I column density of $N_{HI} = 10^{21}$ cm^{-2}. As is noted in these values, the asymmetry in the Rayleigh cross section is quite significant (see also Totani et al. 2016 and Bach & Lee

2014). Therefore we expect that the effect of asymmetry in scattering cross section will be apparent in the flux profile and polarization of Rayleigh scattered radiation.

In this work, we consider far UV radiation in the fixed wavelength range $\lambda_\alpha - 70$ Å $< \lambda < \lambda_\alpha + 70$ Å, and the cross section at the lower and upper wavelength limits is $\sim 10^{-25}$ cm^2.

5.3 Monte Carlo Simulations of Rayleigh Scattering

5.3.1 Scattering Geometry

In this section, we illustrate the scattering geometry adopted in this work. We consider a neutral hydrogen region in the shape of a slab with a finite thickness and infinite lateral extension. The slab geometry is a convenient model to study the fundamental properties of the polarization of Rayleigh scattered radiation and verify the Monte Carlo code as well. In this case, the H I column density N_{HI} along the normal direction completely specifies the scattering geometry.

The other scattering geometry considered in this work is a finite cylindrical shell which is characterized by the height H and the inner and outer radii R_i and R_o, respectively. In this work, we set the parameters $R_o = 2R_i$
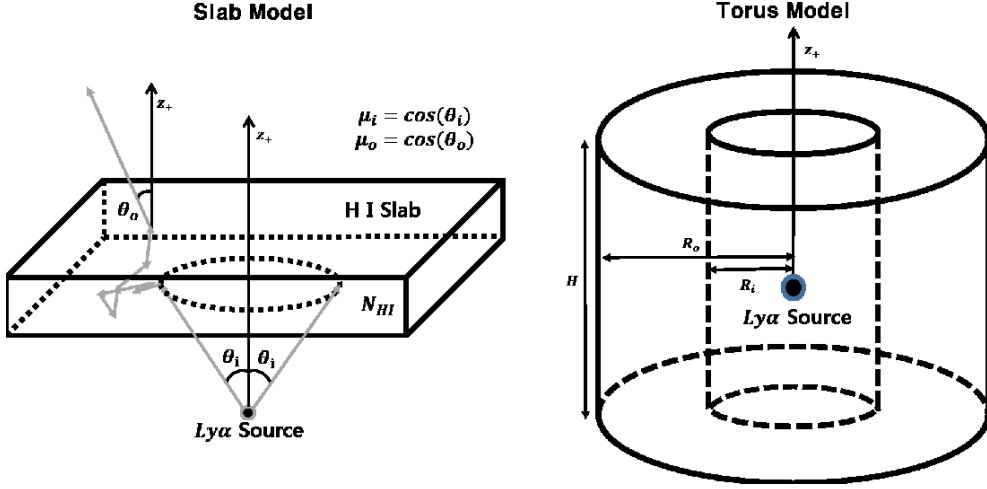
Figure 5.2: Schematic illustration of the scattering geometry adopted in this work. The Lyα emission source is located at the center of the coordinate system. In the case of the slab geometry, hydrogen atoms are uniformly distributed between $z = z_0 > 0$ and $z = z_0 + H$, where H is the thickness of the slab. The column density N_{HI} is measured along the z-direction in the slab geometry. In the torus geometry, hydrogen atoms are uniformly distributed inside a cylinder shell characterized by the inner and outer radii R_i and $R_o = 2R_i$ and the height $H = AR_i$.

so that the inner radius is the same as the lateral width of the shell. There

are two controlling parameters for this geometry. One is the H I column den-

sity $N_{HI} = n_{HI}(R_o - R_i)$ in the lateral direction and the other is the shape

parameter given by the ratio $A = H/R_i$.

A schematic illustration of our scattering geometry is shown in Fig. 5.2.

We set the coordinate system so that z-axis coincides with the symmetry

axis and that the Lyα emission source is located at the origin. In our Monte

Carlo simulations we collect emergent photons according to the z component

$\mu_o = \cos\theta_o$ of the unit wavevector $\hat{\mathbf{k}}$ with the bin size of $\Delta\mu_o = 0.1$. In the

slab case, the Lyα emission source is located on the negative z-axis, so that we will refer emergent photons with negative and positive μ_o to Rayleigh reflected and transmitted photons, respectively.

In this work, we consider two types of incident radiation, one consisting of pure flat continuum and the other with an additional contribution of broad Lyα emission with a triangular profile. The triangular profile is chosen for simplicity of interpretation. The equivalent width of the Lyα emission is set to be 90 Å and the FWHM (full width at half maximum) of that is 20 Å, $\simeq 5000$ km/s in the scale of speed, which appears to be typical in many AGNs (Vanden Berk et al. 2001).

The density matrix formalism is adopted in our Monte Carlo code to describe the polarization information. A 2×2 density matrix ρ is defined by

$$\rho = \begin{pmatrix} (I+Q)/2 & (U+iV)/2 \\ (U-iV)/2 & (I-Q)/2 \end{pmatrix} \tag{5.7}$$

in terms of the Stokes parameters I, Q, U and V (see e.g. Ahn & Lee 2015).

In this simulation the two polarization basis vectors associated with the unit wavevector $\hat{\mathbf{k}} = (\sin\theta\cos\phi, \sin\theta\sin\phi, \cos\theta)$ are chosen as

$$\begin{aligned} \epsilon_1 &= (-\sin\phi, \cos\phi, 0) \\ \epsilon_2 &= (\cos\theta\cos\phi, \cos\theta\sin\phi, -\sin\theta) \end{aligned} \tag{5.8}$$

so that the ϵ_1 and ϵ_2 represent the polarization in the direction perpendic-

ular and parallel to the symmetry axis, respectively.

For each photon generated in the simulation, a density matrix with a unit trace is assigned and followed until escape. Being characterized by the density matrix elements $\rho_{11} = \rho_{22} = 0.5, \rho_{12} = \rho_{21} = 0$, the initial photon from the source is assumed to be completely unpolarized.

According to Schmid (1995) the polarization of Rayleigh scattered radiation is characterized by the same phase function as that of Thomson scattering. The unnormalized density matrix ρ'_p associated with the scattered photon with a new unit wavevector $\hat{\mathbf{k}} = (\sin\theta'\cos\phi', \sin\theta'\sin\phi', \cos\theta')$ is computed using the equation

$$(\rho'_p)_{ij} = \sum_{kl=1,2} (\epsilon'_i \cdot \epsilon_k)\rho_{kl}(\epsilon_l \cdot \epsilon'_j). \tag{5.9}$$

CHAPTER 5. RAYLEIGH SCATTERED Lyα IN AGN

The components are explicitly written as

$$
\begin{aligned}
(\rho_p')_{11} &= (\cos^2 \Delta\phi)\rho_{11} \\
&- (\cos\theta \sin 2\Delta\phi)\rho_{12} \\
&+ (\sin^2 \Delta\phi \cos^2 \theta)\rho_{22} \\
(\rho_p')_{12} &= (\frac{1}{2}\cos\theta' \sin 2\Delta\phi)\rho_{11} \\
&+ (\cos\theta \cos\theta' \cos 2\Delta\phi + \sin\theta \sin\theta' \cos\Delta\phi)\rho_{12} \\
&- \cos\theta(\sin\theta \sin\theta' \sin\Delta\phi + \frac{1}{2}\cos\theta \cos\theta' \sin 2\Delta\phi)\rho_{22} \\
(\rho_p')_{22} &= (\cos^2 \theta' \sin^2 \Delta\phi)\rho_{11} \\
&+ \cos\theta'(2\sin\theta \sin\theta' \sin\Delta\phi + \cos\theta \cos\theta' \sin 2\Delta\phi)\rho_{12} \\
&+ (\cos\theta \cos\theta' \cos\Delta\phi + \sin\theta \sin\theta')^2 \rho_{22} \qquad (5.10)
\end{aligned}
$$

The trace of the unnormalized density matrix represents the angular distribution of the scattered radiation, from which we select θ' and ϕ' in a probabilistic way (Lee et al. 1994). Once the selection is made, the density matrix is normalized to have a unit trace. In the density matrix formalism adopted in this work, the off diagonal element ρ_{12} remains real because Rayleigh scattering induces no circular polarization for an incident radiation with no circular polarization. In other words, the density matrix in this work is a 2×2 real symmetric matrix. Furthermore, due to the axial symmetry of the scattering geometry considered in this work, linear polarization can develop only in the direction parallel or perpendicular to the symmetry axis

122

when spatially averaged, leading to the vanishing average of ρ_{12}. The resultant linear polarization Q is represented by the difference of the two diagonal elements of ρ with a unit trace,

$$Q = \rho_{11} - \rho_{22}. \tag{5.11}$$

Here, a positive Q implies that the polarization develops in the direction perpendicular to the symmetry axis, whereas a negative Q shows polarization in the parallel direction. The scattering geometries considered in this work possess axis-symmetry and our choice of the Stokes parameter Q to represent polarization along the symmetry axis makes the Stokes parameter U vanish.

5.3.2   Rayleigh Scattering in a Slab Region

In this section, we present our Monte Carlo results for Rayleigh scattering in a slab. Note that in sections 3.2.1 and 3.2.2 of this chapter, we only collect photons that are scattered at least once and neglect optically thin photons that pass through the slab without any interaction because our goal is to investigate the polarization properties of the Rayleigh scattered photons depending on the μ_o, μ_i, and N_{HI}.

In section 3.2.3 of this chapter, we integrate over all μ_i to investigate the flux and polarization of radiation originated from an isotropic source.
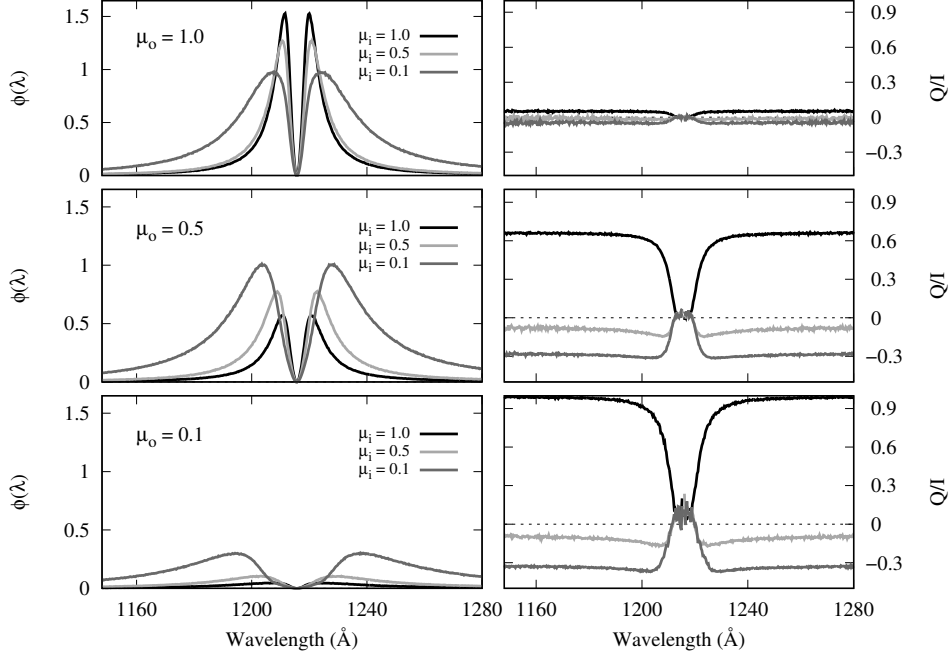
Figure 5.3: Degree of linear polarization (right panels) and flux (left panels) of far UV flat continuum around Lyα that are Rayleigh transmitted from a slab with the H I column density $N_{HI} = 10^{21}$ cm^{-2} in the normal direction. The upper, middle and bottom panels are for those photons emergent with μ_o in the interval $(0.9, 1)$, $(0.4, 0.5)$ and $(0, 0.1)$, respectively. In the right panels, a positive Q/I implies polarization in the direction perpendicular to the slab normal.

We also generate mock spectra using a flat continuum source and a emission source with a triangular profile.

5.3.2.1 Spectra of Reflected and Transmitted Radiation

In Fig. 5.3, we show the flux (left panels) and polarization degree (right panels) for Rayleigh transmitted radiation from a slab with the H I column density of $N_{HI} = 10^{22}$ cm^{-2} in the normal direction. The far UV incident
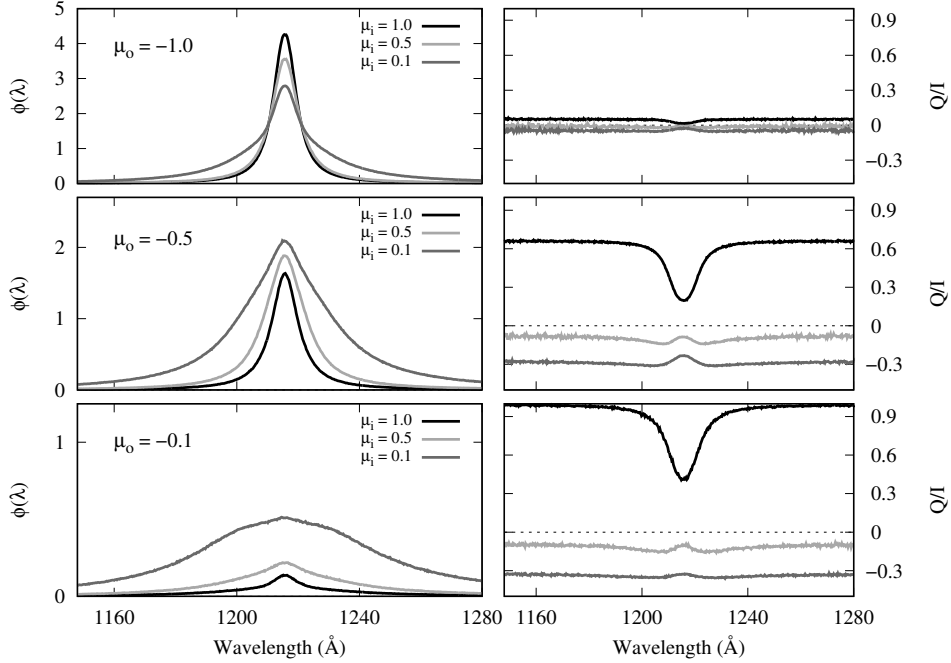
Figure 5.4: Polarization and flux of far UV flat continuum around Lyα Rayleigh reflected from the same slab considered in Fig. 5.3. The upper, middle and bottom panels are for those photons emergent with μ_o in the interval $(-1, -0.9)$, $(-0.5, -0.4)$ and $(-0.1, 0)$, respectively.

radiation is to be taken as a flat continuum, characterized by the same number of photons emitted with specified μ_i per unit wavelength interval. Here μ_i represent the z-component of the unit vector in the direction of the incident photons. The upper panels are flux and degree of polarization of photons emergent with μ_o between 0.9 and 1.0. The middle and bottom panels show the same information for μ_o in the intervals $(0.4, 0.5)$ and $(0, 0.1)$, respectively.

The left panels show the flux profiles for various μ_i and μ_o. All the

transmitted profiles are characterized by the central dip of which the width increases as μ_o decreases from 1 to 0. This implies that the central dip reflects the H I column density of the slab in the direction of incidence. On the other hand, the much extended wing features delineate the scattering cross section that is approximated by a Lorentzian. Being optically thin, most far UV radiation in this wavelength regime will pass through the slab without any interaction with atomic hydrogen.

When $\mu_o \sim 1$, the degree of polarization is nearly zero due to the axial symmetry. This is illustrated in the right top panel, where irrespective of μ_i, Q/I is negligibly small. This case may serve as a check of our code.

An opposite case can be seen in the right bottom panel. For $\mu_i \sim 1$ and $\mu_o \sim 0.1$ corresponding to the normal incidence and emergence in the grazing direction, the degree of polarization in the wing region is nearly 1 in the direction perpendicular to the slab normal (z axis in Fig.5.2). However, near line center the polarization becomes quite weak due to the sharp increase of scattering optical depth.

It is interesting to observe that $\mu_i \simeq 0.1$ and $\mu_o \sim 0.1$ the polarization develops in the direction parallel to the symmetry axis with a typical degree of polarization about 30 % in the wing part. This is because most photons are singly scattered at the large distance from the origin, thus strongly polarized in a direction parallel to the symmetry axis given that the wavevec-

tors of the incident and transmitted photons are located within $z \sim 0$ plane.

In this case also the polarization becomes rapidly weak as the scattering optical depth increases toward the line center. For $\mu_i \simeq 0.5$ and $\mu_o \simeq 0.1$, the polarization is very weak because it corresponds to an intermediate case of the two cases of the normal and grazing incidences. The middle panels show the intermediate behavior between that of the case $\mu_o = 1$ shown in the top panels and that for $\mu_o = 0.1$.

In Fig. 5.4, we show our results for Rayleigh reflected radiation near Lyα from the same slab considered in Fig. 5.3. In the left panels showing the flux as a function of wavelength, we immediately note that all the profiles are characterized by a single broad peak of which the width is dependent on the incident and emergent directions. The photons constituting the central peak are optically so thick that they rarely penetrate to contribute to the transmitted flux considered in Fig. 5.3.

In the right panels, we show the degree of linear polarization of the Rayleigh reflected radiation. In the top panel, the radiation is negligibly polarized because the observer's line of sight nearly coincide with the symmetry axis. An interesting point can be noted in the middle and bottom panels for $\mu_i = 1$. In these cases the center part is the most weakly polarized but still exhibits fairly high degree of linear polarization in excess in 10 per cent. This is highly contrasted with the negligibly polarized cases of the transmit-

ted flux shown in the middle and bottom panels of Fig. 5.3.

This contrasting behavior can be understood by considering the fact that the reflected flux is quite significantly contributed by the singly Rayleigh scattered near the point of entry. These singly scattered photons are highly polarized in the direction perpendicular to the symmetry axis. However, near the Lyα center in the transmitted flux we expect no such singly scattered photons due to the huge scattering optical depths. This leads to negligibly polarized dip in the transmitted flux.

Another interesting point to be noted is the fact that we have a fairly constant degree of linear polarization for the cases of oblique and grazing incidence where $\mu_i \leq 0.5$. This phenomenon is also attributed to the fact that most contribution is made by photons scattered only a few times irrespective of wavelength.

5.3.2.2 Effects of H I Column Density

In Fig. 5.5, we show the polarization behavior as a function of emergent direction for two values of $N_{HI} = 10^{21}$ cm^{-2} (top panels) and 10^{23} cm^{-2}(bottom panels). The horizontal axis shows μ_0, where $\mu_o < 0$ is for Rayleigh reflected radiation and $\mu_o > 0$ for Rayleigh transmitted radiation. The different symbols represent various values of μ_i.

We also divide the incident radiation into two parts depending on the
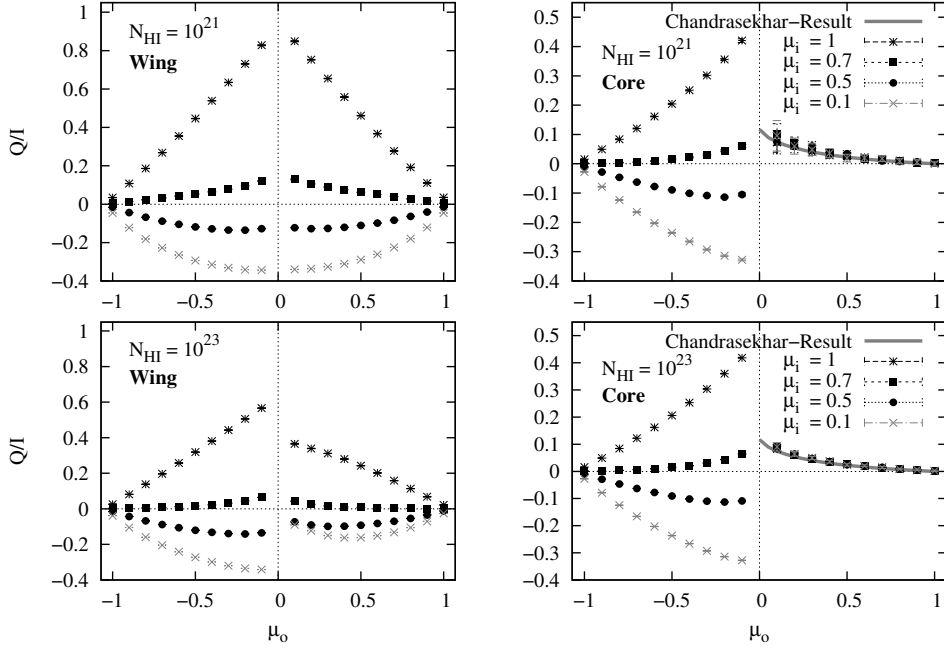
Figure 5.5: Polarization behaviors for wing photons $\tau_s < 10$ Rayleigh scattered from a slab (left panels) and for core photons $\tau_s > 10$ (right panels). In order to find the dependence on H I density, we consider two cases of $N_{HI} = 10^{21}$ cm^{-2} (top panels) and $N_{HI} = 10^{23}$ cm^{-2}. The horizontal axis shows μ_0, where $\mu_o < 0$ is for Rayleigh reflected radiation and $\mu_o > 0$ for Rayleigh transmitted radiation.

scattering optical thickness so that the left panels show the emergent photons for $\tau_s < 10$ (wing) and the right panels for $\tau_s > 10$ (core). The wavelengths corresponding to $\tau_s = 10$ for $N_{HI} = 10^{21}$ cm^{-2} are $\lambda_1 = 1213.61$ Å and $\lambda_2 = 1217.74$ Å. For $N_{HI} = 10^{23}$ cm^{-2} the corresponding wavelengths are $\lambda_3 = 1195.45$ Å and $\lambda_4 = 1236.62$ Å.

Because the incident radiation is prepared in the wavelength range $\lambda_\alpha - 70$ Å$< \lambda < \lambda_\alpha + 70$ Å throughout all the Monte Carlo simulations presented

in this work, the larger wavelength range for $\tau_s < 10$ for $N_{HI} = 10^{21}$ cm^{-2}

than for $N_{HI} = 10^{23}$ cm^{-2} implies that the slab in the case of top left panel

is optically thin to more incident photons than in the case of bottom left.

The Rayleigh scattering phase function is forward and backward symmet-

ric so that an optically thin slab shows the same polarization behavior for

transmitted and reflected components. This is illustrated in the symmetric

polarization with respect to $\mu_o = 0$ in the top left panel. In the bottom left

panel for $N_{HI} = 10^{23}$ cm^{-2} symmetry is significantly broken due to more

contribution from photons with optical depths exceeding unity. These pho-

tons with optical depths greater than unity will be scattered many times

to become quite weakly polarized. This tendency becomes more severe for

photons emergent near the grazing direction ($\mu_o = 0$). Therefore, optically

thin Rayleigh reflected radiation is maximally polarized in the grazing di-

rection, whereas it is no longer the case for Rayleigh transmitted radiation

from grazing incidence ($\mu_i = 0$).

This observation is confirmed in the behaviors shown in the right pan-

els, where all the photons are characterized by $\tau_s > 10$. Rayleigh reflected

components are significantly contributed by photons with a small number of

scatterings leading to strong polarization. Maximal asymmetry is obtained

for photons emergent in the grazing direction, which leads to maximum de-

gree of polarization. This also explains again the stronger polarization shown

in the spectra of Rayleigh reflected radiation than in those of Rayleigh transmitted radiation illustrated in Figs. 5.3 and 5.4.

A very interesting behavior of Rayleigh transmitted radiation is recognized in the right panels, where the scattering optical depths are very large. The polarization develops in the direction perpendicular to the slab normal independent of μ_i. Furthermore, the degree of polarization increases as μ_o approaches 0 from 1. The limit value is 11.7 %, which was obtained by Chandrasekhar (1960) in the polarized transfer of Thomson scattered radiation in an infinitely thick slab (see also Angel 1969). A similar result was obtained by Ahn & Lee (2015) in their study of the polarized transfer of resonantly scattered Lyα.

5.3.2.3 Polarized Lyα from an Isotropic Source

In previous sections, we considered photons only scattered at least once by hydrogen atoms, in which case non-scattered radiation would reduce the observed polarization significantly. In contrast in this section we consider an isotropic source and collect all the photons including those without being Rayleigh scattered. In Figs. 5.6 and 5.7, we show the polarization of Rayleigh scattered radiation in a slab illuminated by an isotropic source for 4 different values of N_{HI}. The input spectrum is the sum of a flat continuum and a broad Lyα emission line flux with a triangular profile described in sec-
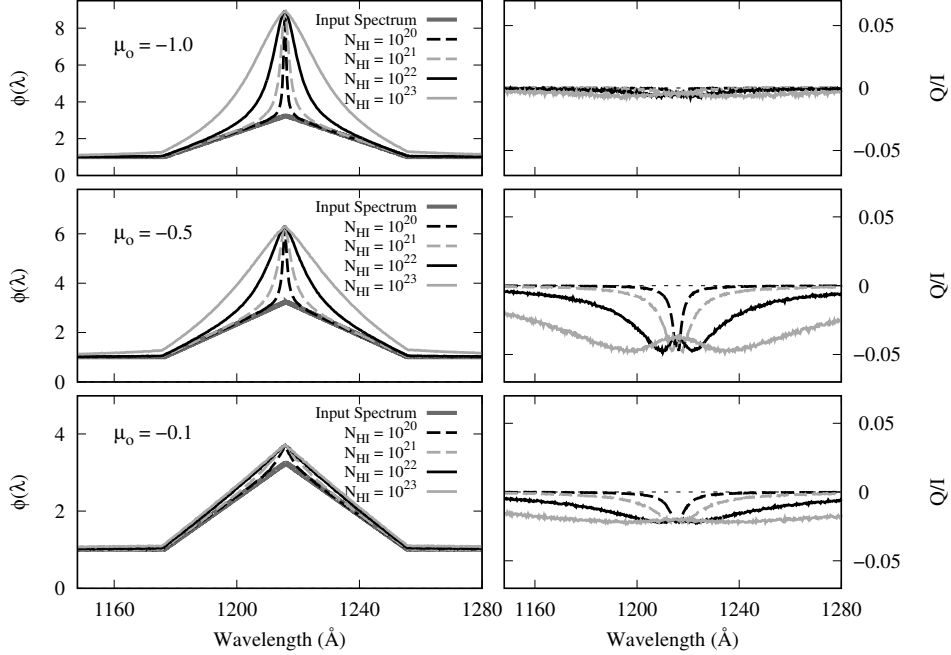
Figure 5.6: Rayleigh reflected degree of polarization(right panel) and flux(left panel) of the isotropic source composed the flat continuum and broad emission. The various lines are shown by H I column densities N_{HI} of slab model.

tion 3.1. The top panel of Fig. 5.6 shows the Rayleigh reflected component emergent in the normal direction, which is negligibly polarized due to symmetry.

Because the covering factor of the scattering region with respect to the emission source is 50 %, the emergent flux is significantly distorted in the wavelength region with $\tau_s > 10$ leading to the formation of the sharp central feature for low values of N_{HI}. As shown in the bottom left panel, the Rayleigh reflected in the grazing direction shows almost the same profile as the incident radiation. This is due to large τ_s in this direction, giving rise
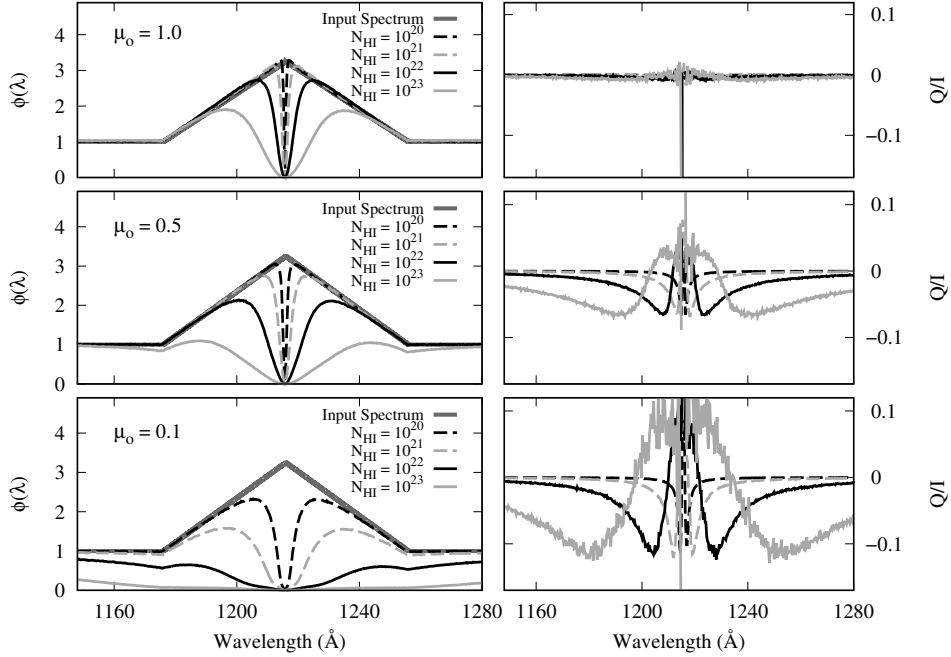
Figure 5.7: Transmitted component of same model as Fig. 5.6.

to full reflection of the incident radiation.

Rayleigh reflected radiation in a slab is polarized in the direction paral-lel to the symmetry axis, which is illustrated by the negative degree of linear polarization in the right panels of Fig. 5.6. Strong polarization is obtained in the case of $\mu_o = -0.5$ and weak polarization is seen for the Rayleigh re-flected radiation emergent in the grazing direction. In the far wing region where the scattering optical thickness is very small, we obtain very weak polarization. It is notable that there exist local maxima in the degree of linear polarization (minima in Q/I value) around the shoulder region for $\mu_o = -0.5$. Here, the term 'shoulder region' is meant to indicate the inter-

mediate region between the core and wing parts. This is explained by the fact that the line center is contributed more significantly by photons scattered many times and hence polarized very weakly than the shoulder region is.

The left panels of Fig. 5.7 show the spectra of Rayleigh transmitted radiation from an isotropic source with a triangular broad Lyα emission. As is previously pointed out, the spectra are characterized by the central dip that depends on the emergent direction and N_{HI}. In the middle right panel and the bottom right panel, the degree of polarization exhibits a complicated behavior. The degree of polarization is positive near line center and negative from the shoulder and wing regions.

This complicated behavior can be understood as follows. For a very optically thick photon the radiative transfer through a thick slab must involve a diffusive propagation along the vertical $z-$ direction until it reaches a slab boundary before escape. The diffusive propagation along $z-$direction induces development of polarization in the direction perpendicular to $z-$ axis. For photons emergent in the grazing direction, the degree of polarization can reach 11.7 per cent, which was shown by Chandrasekhar (1960) and illustrated in the bottom right panel of Fig. 5.7. However, in the far wing regions where photons are optically thin, scattering plane nearly coincides with the slab plane leading to polarization in the direction parallel to $z-$ axis. An
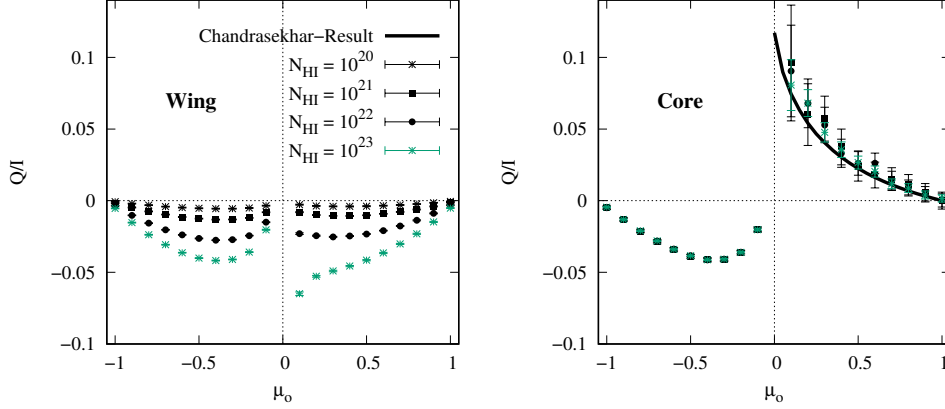
Figure 5.8: Degree of polarization for wing photons(left panel) and core photons(right panel). $\mu_o < 0$ is for reflected component and $\mu_o > 0$ is for transmitted component.

analogous phenomenon can be found in the case of Thomson scattering investigated by Phillips & Meszaros (1986). We point out that the polarization flip around Lyα can be an important signature of Rayleigh transmitted Lyα in a thick neutral slab and that the wavelength at which the flip occurs indicates the characteristic neutral column density of the slab.

The left and right panels of Fig. 5.8 show the polarization behaviors of radiation with low and high Rayleigh scattering optical depths, respectively. In this figure, the simulation parameters are the same as in Figs. 5.6 and 5.7.

In the left panel, the wing photons both Rayleigh reflected and transmitted are polarized in the direction parallel to the symmetry axis. For small values of $N_{HI} \leq 10^{21}$ cm^{-2} the polarization behaviors are similar for Rayleigh reflected and transmitted components. However, for a very thick $N_{HI} = 10^{23}$ cm^{-2} the degree of polarization peaks at $\mu_o \simeq 0$ for Rayleigh transmitted radiation, because they are significantly contributed by singly scattered photons.

In the right panel we notice that the Rayleigh reflected radiation is always polarized in the direction parallel to the symmetry axis irrespective of the Rayleigh scattering optical depth. However, Rayleigh transmitted radiation can be polarized in the direction perpendicular to the symmetry axis only when the Rayleigh scattering optical depth is very high.

In Fig. 5.9, we schematically illustrate polarization behaviors of Rayleigh scattered photons in optically thin and thick cases. Multiply scattered photons tend to be polarized in the direction perpendicular to the symmetry axis as a result of diffusive propagation along $z-$axis, whereas singly scattered photons are polarized in the direction parallel to $z-$axis.

5.3.3 Rayleigh Scattering in a Torus Region

In this section, we consider Rayleigh scattered radiation in a cylindrical shell region, which approximates the torus geometry that is invoked in the uni-
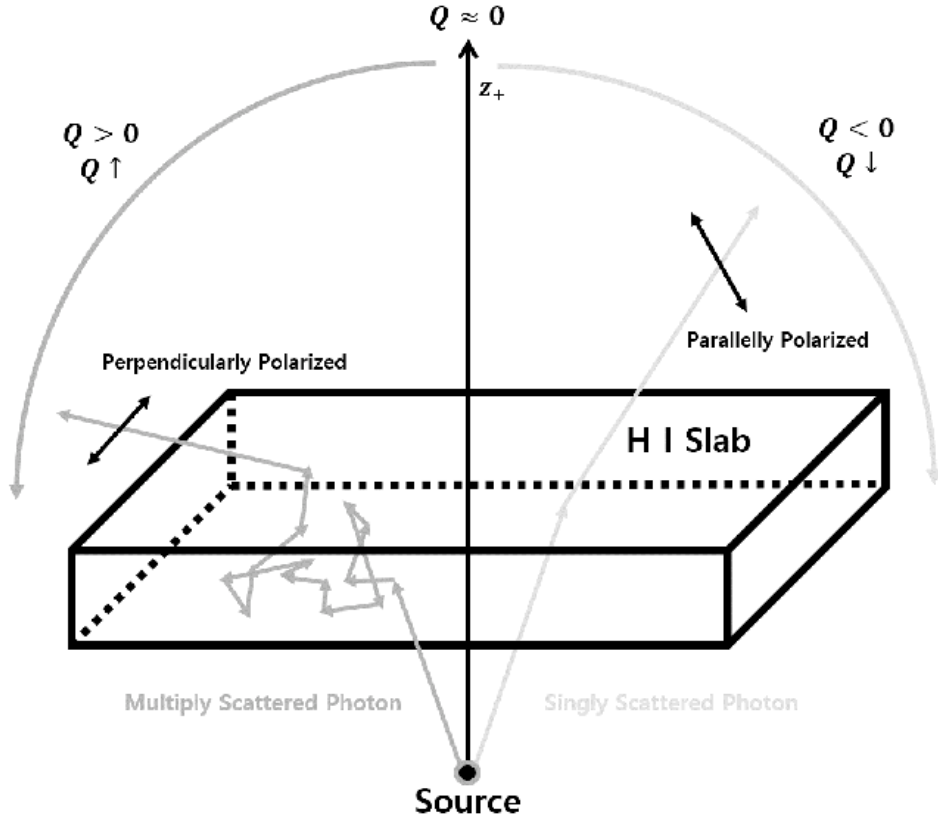
Figure 5.9: Description of degree of polarization for optically thin and thick cases in the slab model.

fication model of AGNs. The torus geometry is symmetric with respect to the plane $z = 0$, and hence the discussion is limited to radiation emergent with $\mu_o > 0$. In this work, the shape of the cylindrical shell is described by the parameter $A = H/R_i$ defined as the ratio of the height and the inner radius.

137
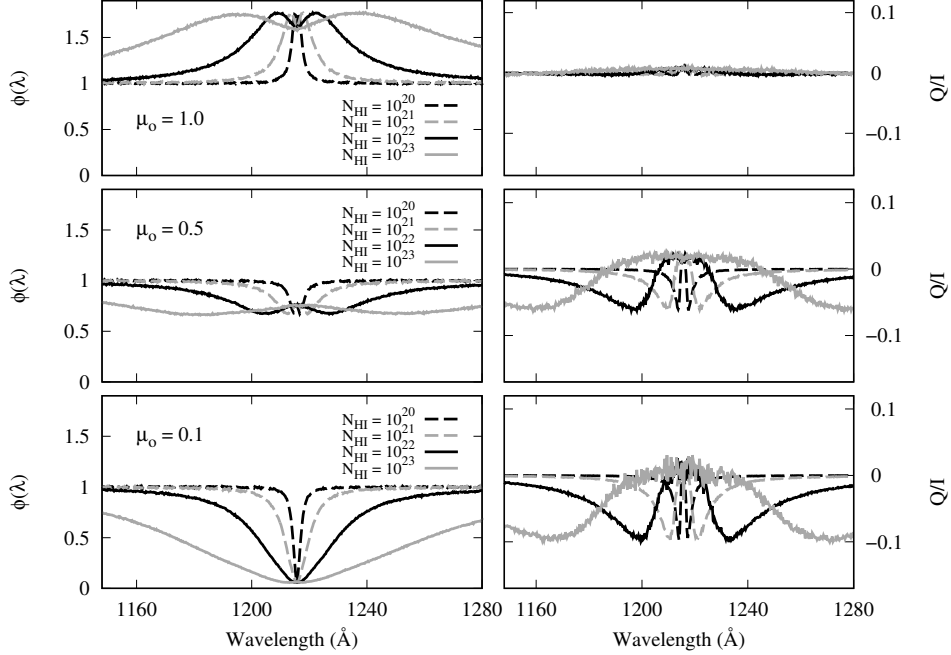
Figure 5.10: Flux and degree of polarization of flat continuum incident on and Rayleigh scattered in a torus with the shape parameter $A = 2$.

5.3.3.1 Spectra and Polarization of Flat Continuum

In Fig. 5.10 we show the flux and polarization of Rayleigh scattered radiation emergent from a torus with $A = 1$ for 4 different values of the H I column density. The incident radiation is pure flat continuum. The top panels show the spectra and degree of polarization emerging along the symmetry axis (analogous to type 1 AGNs). Because of symmetry the emergent radiation is nearly unpolarized. The flux profile exhibits local blue and red maxima. In particular, for $N_{HI} = 10^{23}$ cm^{-2} the maxima are seen at $\lambda = 1187$ Å and $\lambda = 1242$ Å. At these wavelengths the scattering optical depth is near
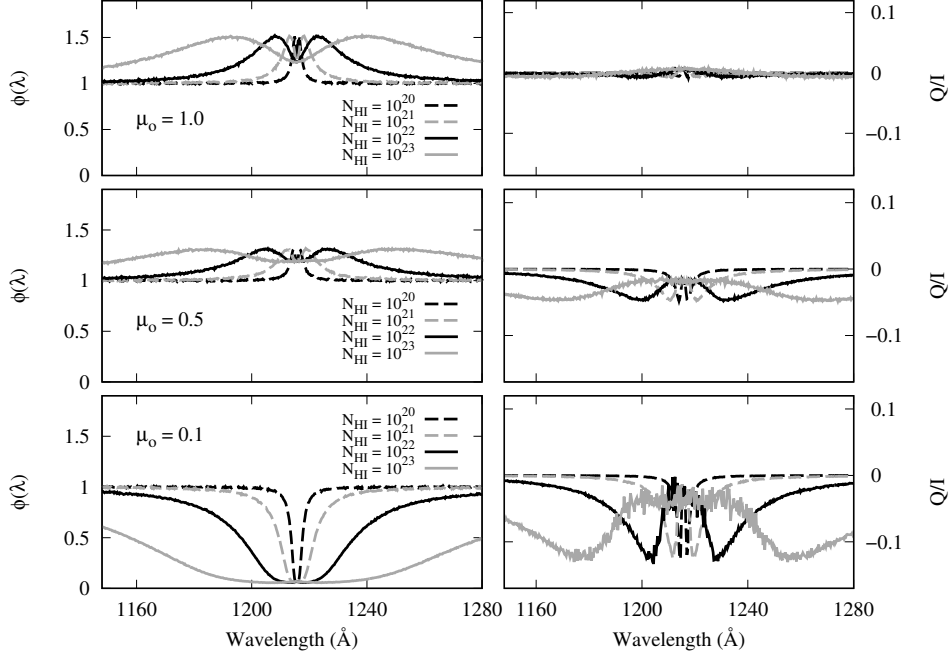
Figure 5.11: Same data as in Fig.5.10 except for $A = 1$. No polarization flip occurs in this case.

unity and the whole scattering region contributes to the flux emergent in the direction near $z-$axis.

The middle panels show the simulated data collected for photons emerging with $\mu_o = 0.5$. As is seen in the left panel, the central part is absorbed because the observer's line of sight is blocked by the cylindrical shell. At the line center we notice a small mound of Rayleigh scattered flux so that the flux minima are found at positions shifted redward and blueward of the line center. The formation of the central mound is attributed to a large number of bouncing near the inner surface of the cylindrical shell by those pho-

tons with huge scattering optical depth τ_s. Through repeated bouncings they climb up the inner cylindrical shell until they reach the upper part where direct escape to the line of sight with $\mu_o = 0.5$ is readily made. Therefore, these photons are polarized in the direction perpendicular to the symmetry axis. This explains the positive degree of polarization shown by those photons in the vicinity of the central mound illustrated in the right panel. In the far wing regions where photons are optically thin, the polarization develops in the direction parallel to the symmetry axis.

The bottom panel shows the spectra and polarization for grazingly emergent radiation (analogous to type 2 AGNs). In this case we observe a simple central dip in the left panel because of the negligible area in the upper part of the cylindrical shell where direct escape is possible. Polarization near the line center is very weak and hence significant polarization along the symmetry axis can be observed in the wing regions.

In Fig. 5.11, we plot the same Monte Carlo result for a torus with $A = 1$. In the middle panel of this figure, we notice that the polarization develops in the direction parallel to the symmetry axis in the entire range of wavelength, and no polarization flip is seen. This is in high contrast with the behavior shown in the middle panel of Fig. 5.10. The torus geometry with a low value of $A = 1$ allows mainly Rayleigh scattering in the plane nearly perpendicular to the symmetry axis, resulting in polarization developing in

the direction parallel to the symmetry axis. The presence of polarization flip in Rayleigh scattered Lyα may indicate quite significant covering factor of the molecular torus in AGNs.

In the bottom panel we notice the polarization behavior of the grazingly emergent radiation qualitatively similar to that found in the middle panel. For photons with Rayleigh scattering optical depth τ_s near unity, single Rayleigh scattering dominates in the plane nearly coinciding with the $x - y$ plane, which leads to strong polarization in the parallel direction with the degree of polarization in excess of 10 percent. The weak polarization near the line center shows the effect of multiple scatterings that tend to randomize the electric field associated with the scattered radiation.

In Fig. 5.12, we illustrate the development of polarization in a torus model. In the tall and optically thick torus, photons tend to be polarized in the direction perpendicular to the vertical axis as they diffuse along the vertical direction through a large number of scattering near the inner wall. This behavior is similar to one considered in the optically thick case shown in Fig. 5.9 and explains the polarization flip in Fig. 5.10. In the case of an optically thin torus, emergent radiation is polarized in the direction parallel to the symmetry axis. This is also similar to the polarization behavior found in the optically thin slab model.
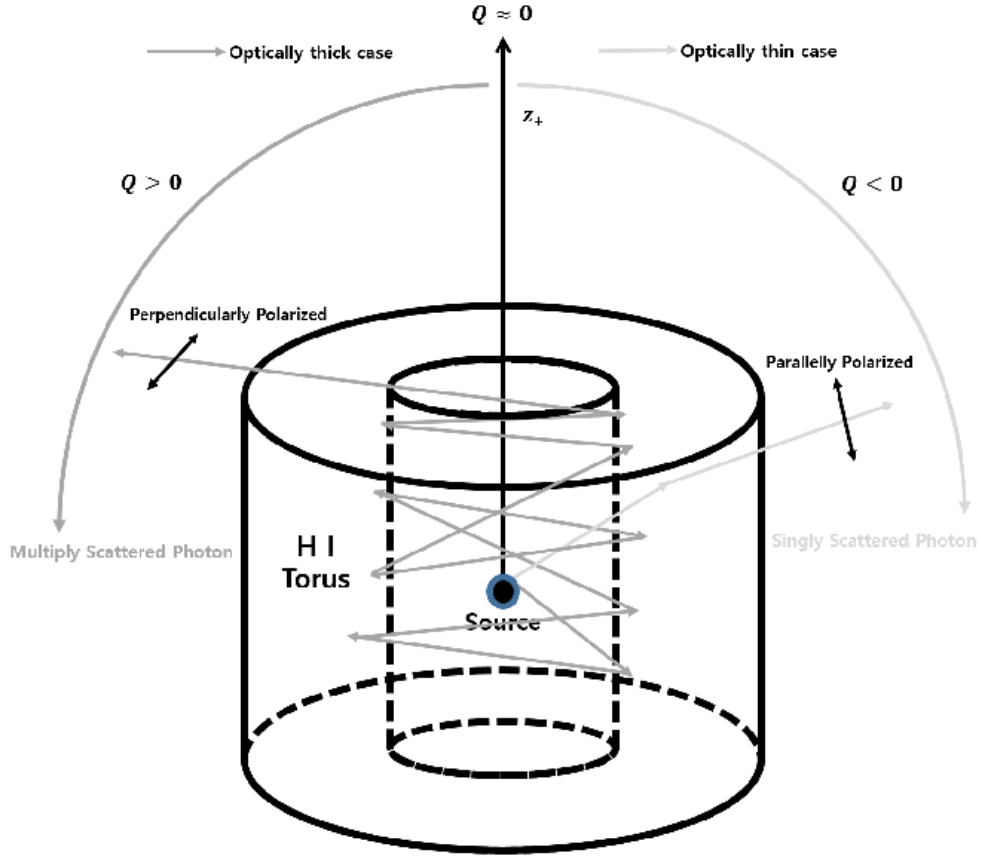
Figure 5.12: Illustration of polarization development in a scattering region with a torus shape. In the case of an optically thick and tall torus, diffusion along the vertical direction tends to orient the electric field in the direction perpendicular to the symmetry axis. In the case of an optically thin torus, emergent light is polarized parallelly to the symmetry axis.
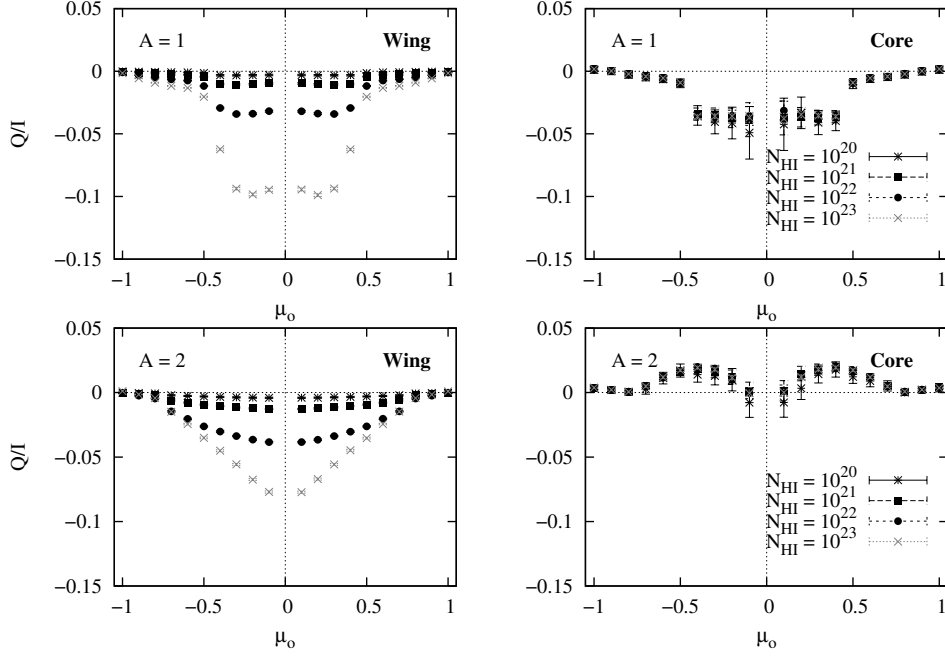
Figure 5.13: Angular distribution of the polarization of Rayleigh scattered from a torus. The left panels are for wing photons $\tau_s < 10$ and the right panels are for core photons ($\tau_s > 10$).

5.3.3.2 Effects of H I Column Density and Covering Factor

In Fig. 5.13 we show the angular distributions of the polarization of Rayleigh scattered from tori with the two values of $A = 1$ and $A = 2$. Four different values of N_{HI} are investigated. In the figure, we divide the incident radiation by the scattering optical depth τ_s in order to clarify the different behaviors of wing photons and core ones.

In the left panels we show the polarization of wing photons ($\tau_s < 10$), all of which are polarized in the direction parallel to the symmetry axis. In the top left panel for the case of $A = 1$, we notice that maximum degree of

polarization is not seen for grazingly emergent radiation but $\mu_o \simeq 0.2$. This is in contrast with the case of $A = 2$ shown in the bottom left panel. In the case of $A = 1$, the polarization behavior resembles that of the wing photons reflected in a slab illustrated in Fig. 5.8. However, in the case of $A = 2$ the polarization behavior resembles that of the transmitted component.

Totally different behaviors are noticed in the case of the transfer of core photons ($\tau_s > 10$). In the top right panel for $A = 1$ all the core photons are polarized in the direction parallel to the symmetry axis, which is the same as their wing counterparts. The degree of polarization is smaller due to the increased number of scatterings required before escape for core photons. However, in the case of $A = 2$ shown in the bottom right panel, core photons are polarized in the perpendicular direction. In this scattering geometry, an core photon needs to climb up along the inner wall of the cylindrical shell by repeated bouncings before it makes the final exit of the scattering region. In the random walk type process of moving up and down along the inner wall, the electric field associated with the photon relaxes in the direction perpendicular to the symmetry axis. This situation is analogous to the perpendicular polarization that develops in the very optically thick slab investigated by Chandrasekhar (1960).
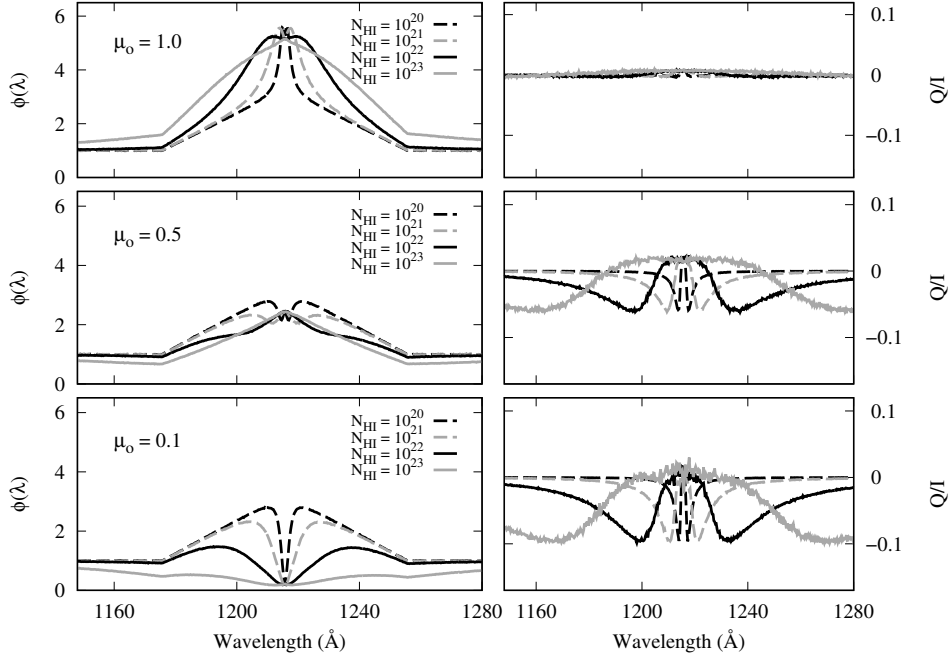
Figure 5.14: Degree of polarization and flux of broad emission and flat continuum incidence source. In this torus model, the shape parameter A is 2.

5.3.4 Mock Spectrum of AGNs in a Torus

In Fig. 5.14, we show our Monte Carlo simulated profiles and polarization of emergent radiation that is Rayleigh scattered in a torus region. The incident radiation consists of a flat continuum and a broad Lyα emission component with a triangular profile, which was considered in section 3.2.3.

The top panels show the data for radiation emergent nearly along the symmetry axis, which is negligibly polarized. However, the profiles are augmented by the Rayleigh scattered flux. For small $N_{HI} = 10^{20}$ cm^{-2} Rayleigh scattering is limited to photons near line center leading to a spiky central
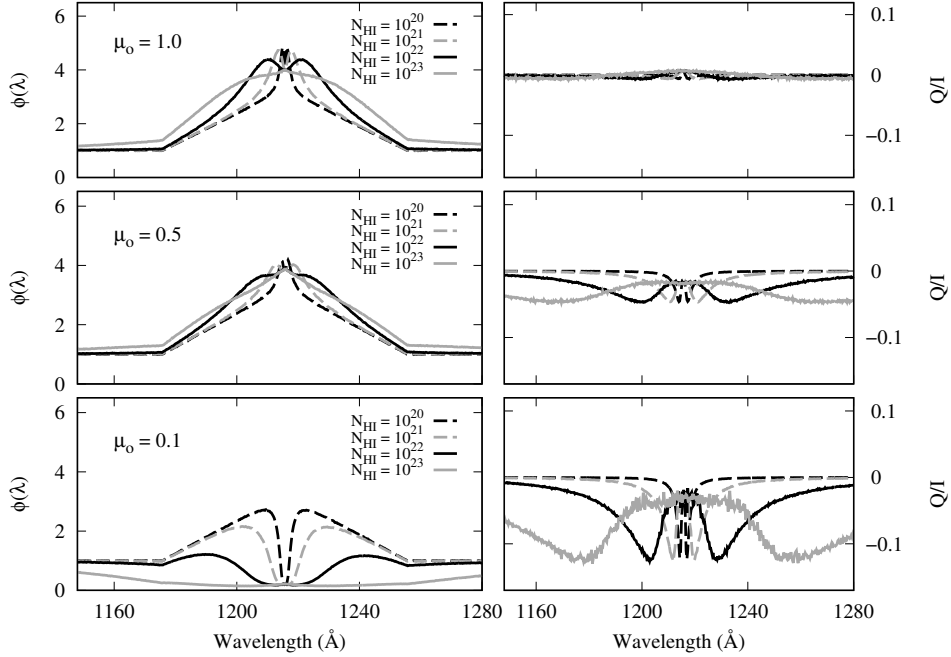
Figure 5.15: This figure is composed by same scheme as in Fig. 5.14 and $A = 1$.

feature.

In the middle panels for emergent radiation with $\mu_o \sim 0.5$, the behavior of polarization flip is apparent. The center part where the scattering optical thickness exceeds unity is polarized in the perpendicular direction. The wing regions exhibit polarization in the parallel direction due to dominant contribution from a small number of scattering occurring in the $x - y$ plane.

The bottom panel shows the simulated data for grazingly emergent radiation. The largest degree of polarization is obtained near the shoulder region with moderate scattering optical depth. In the far wing region where

the scattering optical depth is very small, the degree of polarization is small due to the contribution from the unpolarized incident radiation that is not Rayleigh scattered.

Fig. 5.15 shows our Monte Carlo result for a short torus, for which the behavior is in high contrast with that illustrated in Fig.5.14. In particular, in the middle panel, one can see that Rayleigh scattered radiation near Lyα is polarized in the direction parallel to the symmetry axis and no polarization flip appears. In the bottom panel for which the anisotropy is maximal, the degree of polarization is enhanced and particularly the shoulder part exhibits the degree of polarization in excess of 10 percent.

5.4 Summary and Discussion

In this work, we compute the flux and polarization of the far UV radiation around Lyα Rayleigh scattered in a slab and a torus in order to develop a new spectropolarimetric tool to investigate the unification models of AGNs. In the slab geometry, the transmitted radiation is weakly polarized with the profile exhibiting a central dip in the flux whereas the Rayleigh reflected radiation is significantly polarized with an enhanced line center.

In the torus geometry we find an interesting behavior of polarization flip dependent on the shape of the torus. When the torus is tall with the shape parameter $A = H/R_i = 2$, the Rayleigh thick part near the line center

is polarized in the direction perpendicular to the symmetry axis whereas the wing parts are polarized in the parallel direction. However in the case of a short torus model with $A = 1$, no polarization flip is observed and the emergent radiation is polarized in the direction parallel to the symmetry axis.

It has been proposed that hard X-ray background radiation is significantly contributed by type 2 AGNs (e,g., Comastri et al. 1995). However, the population of type 2 AGNs is only poorly constrained (Gilli et al. 2007). According to AGN unification models, type 2 AGN population is closely related with the geometrical covering factor of the molecular torus. In view of this, detection of polarized Lyα exhibiting a polarization flip in the wing parts may indicate the presence of a tall molecular torus implying a fairly large population of type 2 AGNs.

The models adopted in this work are highly ideal and the H I distribution is more probably far from being axisymmetric. In this case, spectropolarimetric observations may reveal Lyα polarized in different directions depending on wavelength because the Rayleigh scattering optical thickness has no axisymmetry. In this work we made no consideration of narrow Lyα emission component, which may fill the central dip shown in the Rayleigh transmitted component and introduce an additional polarized component.

The Rayleigh scattering cross section is given as a squared sum consist-

ing of contributions from each bound np and free $n'p$ state. For a photon in the vicinity of Lyα, the $2p$ state provides a dominant contribution. A minor contribution from the remaining p states affects the final cross section in a complicated way so that the cross section is larger for radiation redward of Lyα than blueward (Lee 2013).

More quantitatively, for red and blue wavelengths around Lyα, $\lambda_{\pm} = (1 \pm \Delta V/c)\lambda_{\alpha}$ corresponding to the Doppler velocity $\Delta V = 5,000$ km s^{-1}, the asymmetry amounts to

$$\frac{\sigma(\lambda_{+})}{\sigma(\lambda_{-})} - 1 \simeq 0.07. \tag{5.12}$$

The asymmetry amounting to 7 percent in scattering cross section will be more easily detected in the polarized flux than in the total flux. A small excess in the polarized flux redward of Lyα can be regarded as a convincing signature of Rayleigh scattering.

Lying at $+5,900$ km s^{-1} redward of Lyα, the broad N Vλ1240 line is often severely blended with the broad Lyα in many AGNs. This leads to the possibility that the N V line photons can be Rayleigh scattered, which will also enhance the red part of Lyα. However, the red enhancement due to N V is expected to peak at $\Delta V = +5,900$ km s^{-1}, whereas the red enhancement due to asymmetry in cross section is featureless.

One notable example is provided by Koratkar et al. (1995), who used the *Hubble Space Telescope* to perform spectropolarimetry of the quasar PG 1630+377.

They reported that Lyα in this object is significantly polarized with the degree of polarization 7 per cent after correction for unpolarized continuum, whereas no evidence of strong polarization was found in other lines. This is an interesting case because only Lyα can be significantly polarized when the main scattering mechanism is Rayleigh. However, their spectral resolution was too insufficient to reveal any polarization structures, which hinders one from drawing a definite conclusion. Future spectropolarimetric observations will shed much light on the AGN unification model.

Chapter 6

Lyα Radiative Transfer in Lyman Alpha Nebulae: I. Properties of Lyα in Continuous Spherical Halo with a Central Source

6.1   Introduction

Hydrogen Lyα is the most prominent emission line, thus a powerful tool in studying the early universe at $z > 2$. Narrowband imaging surveys have

revealed various strong Lyα-emitting sources: compact Lyα emitters (LAE; Ouchi et al. 2008, 2018), Lyα blobs (LABs; Steidel et al. 2000), and enormous Lyα nebulae (ELAN; Hennawi et al. 2015; Arrigoni Battaia et al. 2019). Lyα blobs are spatially extended over 50–100 kpc and emit a huge amount of Lyα photons with luminosities of $\sim 10^{44}$ erg s^{-1} (Steidel et al. 2000; Matduda et al. 2004; Yang et al. 2009, 2010; Travascio et al. 2020). They are believed to trace massive halos that will evolve into rich galaxy groups or even clusters today. Lyα blobs' gas may represent the proto-intracluster medium, and their embedded galaxies are the progenitors of massive cluster galaxies today.

Spatially extended Lyα emission in the early universe exists in various host galaxies. It has been known that high-z radio galaxies (HzRGs) are often surrounded by gaint Lyα halos. Recently, Borisova et al. (2016) and Arrigoni Battaia et al. (2019) found that extended Lyα nebulae over ~ 50 kpc scale is almost ubiquitous around bright radio-quiet QSOs. Some Lyα nebulae appear to be associated with obscured AGNs (Dey et al. 2005; Yang et al. 2014a). Furthermore, one of the archetypal Lyα blob, SSA22-LAB1, shows multiple small embedded galaxies (Steidel et al. 2000; Matduda et al. 2004; Geach et al. 2016).

However, the origin of their Lyα emission is still controversial. Proposed power sources include photoionization by AGN (Steidel et al. 2000; Arrigoni

Battaia et al. 2019), cooling radiation from cold-mode accretion (Trebitsch et al. 2016; Daddi et al. 2020), shocks due to fast outflows (Cabot et al. 2016; Travascio et al. 2020), and scattering of Lyα photons by the surrounding medium (Hayes et al. 2011; Li et al. 2021). Recently, Li et al. (2021) claimed that, based on Lyα/Hβ line ratios, the extended Lyα emission in SSA22-LAB1 originates from recombination of photo-ionized H II region and subsequent scattering by neutral gas.

Polarimetric observations emerged as a new tool to discriminate among these scenarios. Hayes et al. (2011) first observed a concentric polarization pattern around SSA22-LAB1, claiming that scattering of Lyα photon from a central source is the most viable mechanism. Later, You et al. (2017) and Kim et al. (2020) extended such polarization mapping, showing that polarized Lyα emission is common among Lyα blobs with various embedded sources but with very diverse polarization morphologies. You et al. (2017) show the polarization vectors are aligned as perpendicular to the major axis (also direction of the jet) of in B3 J2330+3927, a Lyα blob around a radio galaxy at $z = 3.087$. Kim et al. (2020) find an asymmetric polarization pattern such that the significant polarizations are detected only toward the southeast of a Lyα nebula, LAB05d. This polarized Lyα emission provides strong evidence that scattering by neutral medium plays an important role in producing extended Lyα emission. However, the interpretation of the po-

larization pattern and strength of scattered Lyα is still challenging due to the small number of statistics on the Lyα polarizations and, more critically, the lack of proper predictions for Lyα polarization in various physical conditions.

The Lyα radiative transfer is the essential tool to investigate the scattered Lyα and origin of extended Lyα emission. However, previous Lyα radiative transfer calculations are not adequate to directly apply to ∼100 kpc scale of Lyα nebulae. For LABs, the radiative transfer simulation has to consider the large scale H I distribution in several tens of kpc scale, broad Lyα emission, and clumpiness of scattering medium. In addition, the RT calculation must carry comprehensive information of scattered Lyα photons, including spatial diffusion, spectral, and polarization information. The previous RT works concentrate mostly on the formation of Lyα spectrum or the polarization under simple geometries: e.g., the classic double-peak solution in a static medium (Neufeld 1990), the formation of Lyα spectra in static or outflowing medium without including polarization (Zheng & Miralda-Escudé 2002; Verhamme et al. 2006), and the surface brightness and polarization profiles of the scattered Lyα in a thin shell geometry (Dijkstra & Loeb 2008). We note that the often-used shell model is not adequate for Lyα nebulae because of the limited H I distribution. Most recently, Eide et al. (2018) investigate the polarization of the scattered Lyα in the context of

compact Lyα-emitting galaxies using spherical or ellipsoidal gas distribution in sub-kpc scale.

Observationally, the clumpiness of the gas in the CGM has to be taken into account — but has been usually overlooked — when investigating the properties of gas. For example, through detailed photo-ionization modeling, Hennawi & Prochaska (2013) and Arrigoni Battaia et al. (2015) suggest that the medium should be composed of numerous unresolved clumps. In addition, several LABs show that their Lyα line peak in velocity space often coincide with the systemic velocity of the embedded galaxies (Prescott et al. 2009; Yang et al. 2011, 2014a). Given that Lyα photons experiencing scattering in *continuous* medium are always scattered off from the systemic velocity of the galaxies and gas (e.g., the double-peaked profile in static medium or redshifted profile in outflowing medium), these Lyα spectra are hard to reconcile with the current RT calculations.

Lyα RT calculations with a full treatment of clumpy medium has not been fully explored, especially in the context of extended Lyα emission. The previous studies concentrate on the Lyα escape fraction from the clumpy medium of star-forming galaxies (Neufeld 1991; Hansen & Oh 2006; Duval et al. 2014). The claim was that the escape fraction increases in the clumpy medium thanks to the surface scattering. When an optically thick photon encounters a clump, the photon quickly escapes through several scatterings

at the surface. Gronke et al. (2016, 2017) investigate the formation of Lyα spectra in clumpy medium and demonstrate that the Lyα spectra in clumpy medium become similar to those in a continuous medium when the covering factor of clumps are very high. Trebitsch et al. (2016) calculate Lyα polarizations in a radiative hydrodynamic simulation to investigate the polarization arising from cold gas accretion. They assume completely polarized photons and adopt the method in Rybicki & Loeb (1999) for Rayleigh scattering to compute the polarization of Lyα. We note that this method is not sufficient to describe the polarization behavior of photons that are resonantly scattered near the line center.

In this paper, we develop Lyα radiative transfer simulations in the context of extended Lyα emission. To explore the various physical parameter space, we plan to present an extensive library of RT calculations for models in both smooth (this thesis) and clumpy medium (in the future). Our simulation adopts a Monte-Carlo technique using ray-tracing in a grid-based geometry. To compute the polarization of scattered Lyα accurately, we utilize a new method, including the effect of resonance scattering in Seon et al. (in prep). The photon packet in our simulation carries multi-dimensional information, including wavelength, direction, position, polarization information. We consider a geometry where a spherical scattering medium surrounds point sources. Our goal is to carry out a systematic study for LABs to test

if the Lyα scattering alone can explain the observed extended Lyα emission. This first of a series of papers studies the scattered-only Lyα in the continuous spherical halo. This paper is organized as follows. In Section 6.2, we describe the algorithm of our simulation. In Section 6.3, we explain the scattering geometry of continuous and clumpy medium and central point source. In Section 6.4, we present surface brightness profiles, polarization, and the integrated Lyα spectra in a smooth medium. In Section 6.5, we summarize our results.

6.2 Radiative Transfer of Lyα

The line formation of Lyα considered in this work is based on the 3D Monte Carlo code *LaRT* that stands for Lyα Radiative Transfer developed by Seon & Kim (2020). They used the *LaRT* code to investigate the Wouthuysen-Field effect, carefully dealing with the hyperfine structure of atomic hydrogen. In this work, modifications are made to *LaRT* in order to incorporate the emission source that is embedded in the medium with a broad spectral line width. In this section, we briefly describe the atomic physics related to the scattering of Lyα adopted in *LaRT*.

6.2.1 Scattering cross section

The scattering cross section of Lyα is characterized by the oscillator strength

$f_{12} = 0.4162$. In this work, no consideration is made about the hyperfine

structures and Lyα is a resonance doublet line associated with the fine struc-

tures $2p_{1/2}$ and $2p_{3/2}$ of the $2p$ level. We denote by 'H' and 'K' the tran-

sitions $(1s_{1/2} - 2p_{1/2})$ and $(1s_{1/2} - 2p_{3/2})$, respectively. The cross section of

Lyα is described by the sum of two Lorentzian functions near the 'H' and

'K' line centers in the rest frame of an atom. Convolution with the local

random motions of hydrogen atoms well approximated by a Gaussian distri-

bution leads to the Voigt profile function describing the cross section in the

observer's frame.

Explicitly, the scattering cross section of Lyα as a function of the fre-

quency is given by

$$\sigma_\nu = \frac{\sqrt{\pi}e^2 f_{12}}{\Delta\nu_D m_e c}\left[\frac{1}{3}H(x_H, a) + \frac{2}{3}H(x_K, a)\right]. \tag{6.1}$$

Here, $H(x, a)$ is the Voigt-Hjerting function given by

$$H(x, a) = \frac{a}{\pi}\int_{-\infty}^{\infty}\frac{e^{-y^2}}{(x-y)^2 + a^2}dy \tag{6.2}$$

where $a = \Gamma/(4\pi\Delta\nu_D)$ is the natural width parameter. The damping con-

stant is $\Gamma = 6.265 \times 10^8$ s^{-1} and the thermal Doppler width is denoted by

$\Delta\nu_D = \nu_{Ly\alpha}v_{\text{th}}/c$ with the thermal speed $v_{\text{th}} = \sqrt{2k_B T/m_p}$.

The dimensionless frequency parameters corresponding to 'H' and 'K' transitions are defined as $x_H = \nu - \nu_H/\Delta\nu_D$ and $x_K = \nu - \nu_K/\Delta\nu_D$, respectively. We set the central frequency of Lyα $\nu_{Ly\alpha} = 2.466 \times 10^{15}$ Hz and the frequency difference between 'H' and 'K' transitions is $\Delta\nu_{HK} = 1.08 \times 10^{10}$ Hz . In this work, the temperature of the scattering medium is fixed to 10^4 K so that the velocity difference of the two lines, $c\nu_{HK}/\nu_{Ly\alpha}$, is much smaller than v_{th}. This in turn leads to the total cross section that is excellently described by a single Voigt profile (Seon & Kim 2020).

6.2.2 Polarization

No rigorous distinction between resonance scattering and Rayleigh scattering can be given to a scattering process of a Lyα photon. A commonly accepted usage of the term 'resonance scattering' refers to a scattering process that occurs in a frequency range within a few Γ from the line center in the rest frame of the scattering atom. In contrast, a scattering process further from the line center may be called Rayleigh scattering. In the case of Lyα, Rayleigh scattering is more effective to yield linearly polarized radiation than resonance scattering.

In particular, it is fascinating that resonance scattering near the $1s_{1/2}-2p_{1/2}$ results in completely unpolarized radiation, whereas weakly polarized radiation appears as a result of resonance scattering associated with the

$1s_{1/2} - 2p_{3/2}$ transition.

Ahn et al. (2002) adopt the density matrix to investigate the polarized radiative transfer using photon packets with the polarization information incorporated into the Hermitian 2×2 density matrix (e.g. Chang et al. 2017; Eide et al. 2018). Here, the photon packet is equivalent to the ensemble average of numerous photons. With this packet formalism, the degree of polarization of an initial photon packet is chosen to be null. The density matrix is renewed to assign the polarization information each time of scattering in the observer's frame. Separate renewing schemes are applied to the two different Rayleigh and resonance scattering processes. The scattering type is determined in a probabilistic way after an appropriate assessment of occurrence probabilities of Rayleigh and resonance scattering as a function of ν.

In our simulation, we adopt the Stokes vector of a photon packet to represent the polarization state of Lyα. The Stokes vector is represented as a column vector

$$\mathbf{S} = \begin{pmatrix} I \\ Q \\ U \\ V \end{pmatrix}.$$

(6.3)

Here, the Stokes parameters are defined by

$$
\begin{aligned}
I &= \; < E_m E_m^* + E_n E_n^* > \\
Q &= \; < E_m E_m^* - E_n E_n^* > \\
U &= \; < E_m E_n^* + E_m^* E_n > \\
V &= \; i < E_m E_n^* - E_m^* E_n >,
\end{aligned}
\tag{6.4}
$$

where E_m and E_n are the electric field along the polarization basis vectors $\hat{\mathbf{m}}$ and $\hat{\mathbf{n}}$, respectively. The transverse nature of the electromagnetic waves requires that the polarization basis vectors are orthogonal to the wavevector $\hat{\mathbf{k}}$.

The renewed Stokes vector $\mathbf{S}'$ is determined by the polar scattering angle $\theta = \hat{\mathbf{k}} \cdot \hat{\mathbf{k}}'$, where $\hat{\mathbf{k}}'$ is the wavevector associated with the scattered radiation. Seon et al. (in prep) introduce the two matrices $\mathbf{M}(\theta)$ and $\mathbf{L}(\phi)$ to obtain $\mathbf{S}'$ given by

$$
\mathbf{S}' = \mathbf{M}(\theta)\mathbf{L}(\phi)\mathbf{S}.
\tag{6.5}
$$

Use is made of the explicit expressions of $\mathbf{M}(\theta)$ and $\mathbf{L}(\phi)$ to yield $\mathbf{S}'$

in relation to $\mathbf{S}$ given by

$$
\begin{aligned}
I' &= [\frac{3}{4}E_1(\cos^2\theta + 1) + E_2]I \\
&+ \frac{3}{4}E_1(\cos^2\theta - 1)(Q\cos 2\phi + U\sin 2\phi) \\
Q' &= \frac{3}{4}E_1(\cos^2\theta - 1)I \\
&+ \frac{3}{4}E_1(\cos^2\theta + 1)(Q\cos 2\phi + U\sin 2\phi) \\
U' &= \frac{3}{2}E_1\cos\theta(-Q\sin 2\phi + U\cos 2\phi) \\
V' &= \frac{3}{2}E_3\cos\theta V.
\end{aligned}
\tag{6.6}
$$

Here, the parameters E_1, E_2, and E_3 are defined as

$$
E_1 = \frac{2x_K x_H + x_H^2}{x_K^2 + 2x_H^2}, \; E_2 = 1 - E_1, \; E_3 = \frac{1}{3}(E_1 + 2).
\tag{6.7}
$$

The computation of $\mathbf{S}'$ using Eq. (6.6) can be carried out only after the scattering angles θ and ϕ are specified. The polar angle θ is selected from the probability density proportional to I'/I, that is,

$$
P(\cos\theta) = \frac{3}{4}E_1(\cos^2\theta + 1) + E_2.
\tag{6.8}
$$

The azimuthal angle ϕ is chosen from a uniform distribution in the range between 0 and 2π. We divide the Stokes vector $\mathbf{S}'$ by I' for nomalization so that

$$
\mathbf{S}' = \begin{pmatrix} 1 \\ Q'/I' \\ U'/I' \\ V/I' \end{pmatrix}.
\tag{6.9}
$$

The Lyα emission source is assumed to be isotropic and unpolarized, and therefore the initial Stokes vector is given by

$$\mathbf{S_i} = \begin{pmatrix} 1 \\ 0 \\ 0 \\ 0 \end{pmatrix}.$$ (6.10)

6.3 Modeling spherical halo with a central point source
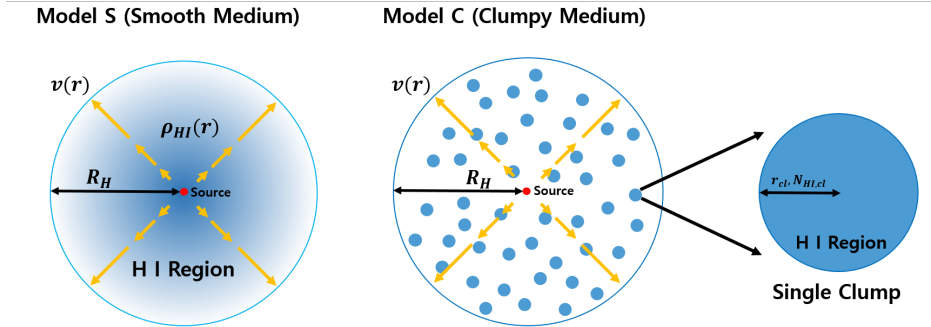
Figure 6.1: Schematic illustration for the Model S (smooth medium) and C (clumpy medium). The red dot is the central Lyα source. Orange arrows mean the expanding velocity proportional to the radius. The clumps are uniformly distributed in the halo and the density of single clump is uniform.

To simulate Lyα halos produced mainly by Lyα scattering, we consider a spherical H I halo with a central Lyα point source. The radius of the scattering medium is fixed to $100\,\mathrm{kpc}$ that is comparable to the typical sizes of LABs or ELANe. We consider two types of models: Model S ("smooth"

medium model) and Model C ("clumpy" medium model) depending on the distribution of neutral H I gas. Note that in this article, we will focus on the Model S, and next series of papers will be devoted to the Model C. Nonetheless, for completeness, we provide the details of both Model C and S here. Figure 6.1 shows the schematic illustration for two models. The H I medium in the Model S is continuously distributed. In Model C, the scattering medium is composed of numerous spherical clumps over the grid of 200^3 pixels. The intra-clump region is set to empty. The source at the center emits Lyα photons with an initial spectrum approximated with a Gaussian function with a width of several hundred $\mathrm{km\,s^{-1}}$. Throughout the paper, we assume that the model halo is located at $z = 3$ with an angular scale of 7.855 kpc arcsec^{-1} and has a Lyα luminosity of $10^{44}\mathrm{erg\,s^{-1}}$. The number of the photon packets emitted from the source is 5×10^5. In the following, we introduce the detailed physical condition of the two models and the point source.

6.3.1 Model S (Smooth Medium)

In Figure 6.1(left), we show the schematic illustration of the Model S. The H I number density of spherical H I region declines exponentially as a function of the distance r. We adopt the expanding velocity field where the outflow speed is proportional to the distance. The H I number density $n_{\mathrm{HI}}(r)$

and the radial velocity $v(r)$ are given by

$$n_{\mathrm{HI}}(r) = n_0 \, e^{-r/R_e}, \quad v(r) = v_{\mathrm{exp}} \, \frac{r}{R_H} \, , \qquad (6.11)$$

where R_e is the effective radius of the exponential profile, and r is the radius from the central source. The v_{exp} is the outflow velocity characterizing kinematics of scattering region. The R_H is the halo radius and fixed to $100\,\mathrm{kpc}$. We explore the range of $R_e/R_H = 0.3$, 0.5, 1, and ∞ (i.e. uniform distribution). For these sets of parameters, the total H I column density N_{HI}, which characterizes the optical thickness of H I region, is given by

$$N_{\mathrm{HI}} = \int_0^{R_H} n_{\mathrm{HI}}(r) dr. \qquad (6.12)$$

We set the range of $N_{\mathrm{HI}} = 10^{18-21}\,\mathrm{cm}^{-2}$. Then, the total neutral H I mass of the spherical halo is given by

$$M_{\mathrm{HI}} \approx 2.5 \times 10^8 M_\odot \left(\frac{R_e}{R_H} \right)^4 \left(\frac{N_{HI}}{10^{18}\mathrm{cm}^{-2}} \right). \qquad (6.13)$$

In the case of the uniform medium $(R_e = \infty)$,

$$M_{HI} \sim 3.4 \times 10^8 M_\odot \left(\frac{N_{HI}}{10^{18}\mathrm{cm}^{-2}} \right). \qquad (6.14)$$

Given that the dark matter halo mass of Lyα blobs at $z \sim 2$ has been estimated $M_{\mathrm{DM}} \sim 10^{12.5-13.0} M_\odot$ (Yang et al. 2010), the range of $N_{\mathrm{HI}} = 10^{18-21}\,\mathrm{cm}^{-2}$ corresponds to $M_{\mathrm{HI}} = 10^{8-11}\,\mathrm{M}_\odot$.

6.3.2 Model C (Clumpy Medium)

Figure 6.1(right) illustrates Model C, where the halo gas consists of numerous small clumps. We adopt the same halo size of $R_H = 100$ kpc as the Model S. All neutral H I is confined within these clumps, and there is no neutral medium in the inter-clump space. The clumps are uniformly distributed over the halo and do not overlap each other. Unlike the Model S, due to the limited hardware memory, we do not vary the density profile of the medium by changing the number distribution of clumps. In a clump, the H I medium is static and uniform, and then the H I number density of the clump is $N_{\mathrm{HI,cl}}/r_{cl}$ where $N_{\mathrm{HI,cl}}$ is the H I column density of a clump. We set the physical radius of the clump r_{cl} to $10\,\mathrm{pc} - 1\,\mathrm{kpc}$ ($r_{cl} \ll R_H$), thus the clumps is not spatially resolved at $z > 2$, which is consistent with observations. Note that Gronke et al. (2017) considered clumps with the radius $10^{-3} - 10^{-2}\,\mathrm{pc}$ in a halo with the size of $100\,\mathrm{pc}$ in their study. Through studying a giant Lyα nebula around a bright QSO (UM287), Arrigoni Battaia et al. (2015) constrained the physical condition of clumps: the hydrogen column density of clumps $N_{\mathrm{HI,cl}} \lesssim 10^{20}\,\mathrm{cm}^{-2}$ and the radius of clumps $r_{cl} \lesssim 20\,\mathrm{pc}$. The total column density of the clumpy halo (N_{HI}) is given by

$$N_{\mathrm{HI}} = f_c N_{\mathrm{HI,cl}}, \tag{6.15}$$

where the covering factor f_c represents the number of clumps in the line of sight between the central source and an observer. We explore the range of f_c = 1 – 100 and $N_{\mathrm{HI,cl}} = 10^{16-19}\,\mathrm{cm}^{-2}$. To describe outflows in the H I halo, we set the radial velocities of individual clumps proportional to the distance between the central source and the center of clumps following Eq. 6.11. The total H I mass of clumpy halo is given by

$$M_{\mathrm{HI}} \sim 4.5 \times 10^8 M_\odot \left(\frac{f_c\ N_{\mathrm{HI,cl}}}{10^{18}\mathrm{cm}^{-2}} \right). \qquad (6.16)$$

The mass of the Model C is more massive by $\sim$ 30% than the uniform medium of the Model S at the same total column density.

6.3.3 Central Point Source

In our simulation, we consider the isotropic emission from the central source. To investigate the dependence on the width of Lyα emission, we consider the spectrum of the input source to follow a Gaussian function $F(\lambda_i)$,

$$F(\lambda_i) = \frac{1}{\sqrt{2\pi}\sigma_{\lambda,src}} \exp\left[-\frac{(\lambda_i - \lambda_{Ly\alpha})^2}{2\sigma_{\lambda,src}^2} \right], \qquad (6.17)$$

where λ_i is the wavelength of an initial photon, and $\sigma_{\lambda,\mathrm{src}}$ is the intrinsic line width of Lyα emission of the input source. Hereafter, we adopt and use the velocity width $\sigma_{\mathrm{src}} = c\sigma_{\lambda,src}/\lambda_{\mathrm{Ly}\alpha}$ as the substitute of $\sigma_{\lambda,\mathrm{src}}$. Depending on the nature of embedded galaxies in Lyα halo, we consider σ_{src} from

Parameter	Range	Note
$N_{\rm HI}$	$10^{18-21}\,{\rm cm}^{-2}$	H I column density
R_e	$0.1R_H - R_H,\ \infty$	Effective radius
$v_{\rm exp}$	$0 - 400\,{\rm km\,s}^{-1}$	Expanding velocity
$\sigma_{\rm src}$	$100 - 400\,{\rm km\,s}^{-1}$	Lyα source width

Table 6.1: The parameters of Model S.

$100\ {\rm km\,s}^{-1}$ (star forming galaxy case) to $400\ {\rm km\,s}^{-1}$ (active galactic nuclei case).

6.4 Smooth Medium (Model S)

To investigate the behavior of Lyα in the smooth medium, we produce the simulated images for observables such as Lyα intensity and polarization. In Figure 6.2, we show examples of the Model S: surface brightness distributions, degrees and orientations of polarization, and Stokes parameters (Q/I and U/I) for three column densities, $N_{\rm HI} = 10^{18}$, 10^{19}, and $10^{21}\,{\rm cm}^{-2}$, respectively. Here, we fix the expanding velocity $v_{\rm exp} = 400\,{\rm km\,s}^{-1}$ and the velocity width of the Lyα source $\sigma_{\rm src} = 400\ {\rm km\,s}^{-1}$.

Here, we briefly describe general trends of the Model S and will discuss the results as functions of various parameters in the following sections. First, we find that the surface brightness profiles become more extended as the total H I column density ($N_{\rm HI}$) increases (Figure 6.2 left). Second, the polarization patterns are concentric due to the spherical symmetry and in-

crease radially outward (Figure 6.2 second column). These predictions are consistent with the previous findings (Dijkstra & Loeb 2008; Eide et al. 2018). Third, the degree of polarization does *not* behave monotonically as a function of N_{HI}. We find that the overall degree of polarization in the case of $N_{\mathrm{HI}} = 10^{19}\,\mathrm{cm}^{-2}$ is larger than those of $N_{\mathrm{HI}} = 10^{18}$ and $10^{21}\,\mathrm{cm}^{-2}$ cases. Lastly, we find that in the case of $N_{\mathrm{HI}} = 10^{19}\,\mathrm{cm}^{-2}$, the P increases steeply from the nearly 0% at the center of the halo to 20% right in the vicinity of the center. Throughout the paper, we will refer this behavior as "polarization jump". This discontinuous P profile is one of the most surprising results from our simulation.

In the following, we describe the Lyα halos in the parameter space defined in Table 6.1. We present the surface brightness profile and the degree of polarization as a function of the projected radius in Section 6.4.1 and 6.4.2, respectively. In Section 6.4.1, we measure the observable sizes of Lyα halos (R_{obs}) in order to determine whether scattered Lyα photons from a point source can produce the observed Lyα halos at high redshift with typical sizes of 100 kpc ($\sim$10). In Section 6.4.2, we explain the origin of the polarization jump in detail and compute the polarization at R_{obs}. In Section 6.4.3, we present the integrated Lyα spectra and explain Doppler shift by the scattering in expanding medium with the Hubble flow-like velocity field. We measure the velocity offset of the line peak to investigate the re-

lation between the offset and the kinematics of the scattering medium.

For the Lyα source spectrum, we consider two extremes: $\sigma_{\mathrm{src}} = 100$ km s^{-1} for typical star-forming galaxies (SFGs) and $\sigma_{\mathrm{src}} = 400$ km s^{-1} for the active galactic nuclei (AGNs) case. Hereafter, we will refer to these two cases as SFG and AGN cases.
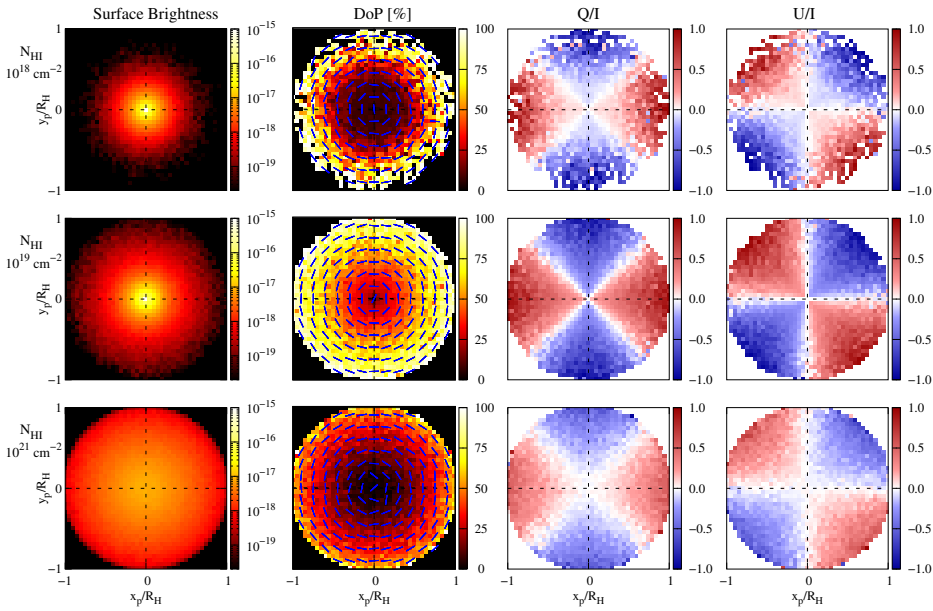
Figure 6.2: The projected image for $N_{\mathrm{HI}} = 10^{18}$ cm^{-2} (top), 10^{19} cm^{-2} (middle), and 10^{21} cm^{-2} (bottom) with $v_{\mathrm{exp}} = 400$ km s^{-1}, $A = \infty$, and $\sigma_{\mathrm{src}} = 400$ km s^{-1}. The left panels are the surface brightness in the logarithmic scale. The three right panels represent the polarization information, the degree of polarization, Stokes parameters Q/I, and U/I. The blue solid lines mean the direction of the polarization. At the center, the surface brightness is highest and the polarization is zero. In the middle panels, the polarization steeply increases near the center. This dramatic increase is called 'Polarization Jump'.
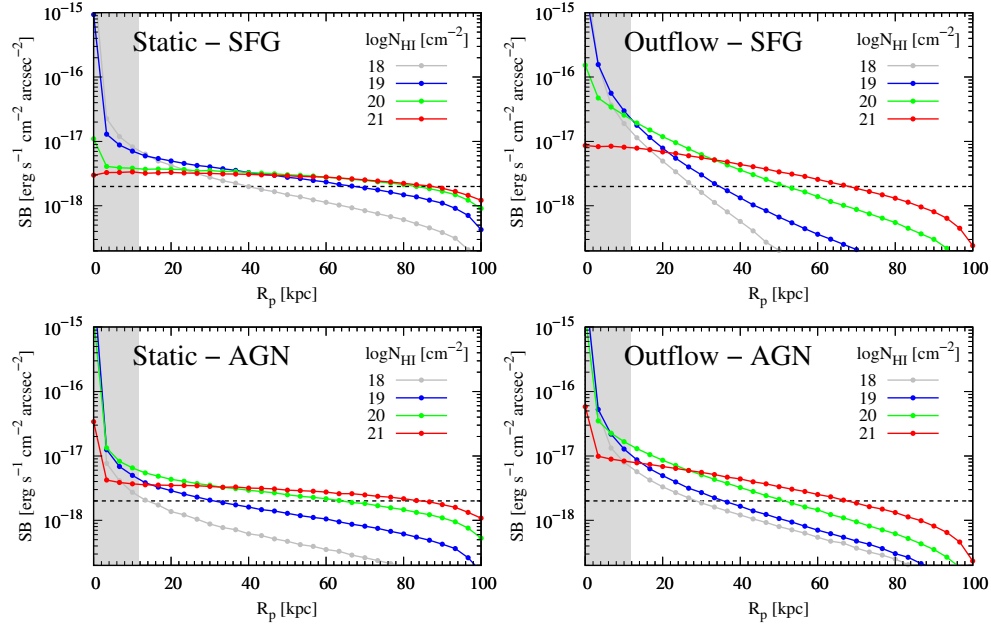
Figure 6.3: The radial profiles of surface brightness for $N_{\mathrm{HI}} = 10^{18-21}\,\mathrm{cm}^{-2}$. The y-axis is the surface brightness in cgs unit. The x-axis is the projected radius $R_p = \sqrt{x_p^2 + y_p^2}$. The density of H I halo is uniform (i.e. $R_e = \infty$). The top and bottom panels represent SFG and AGN cases, respectively. 'Static' (left panels) and 'Outflow' (right panels) mean $v_{\mathrm{exp}} = 0\,\mathrm{km\,s}^{-1}$ and $400\,\mathrm{km\,s}^{-1}$. The gray zone with $R_p \lesssim 10\,\mathrm{kpc}$ is the region affected by seeing effect. The vertical dashed line is the observational threshold, 2×10^{-18} $\mathrm{erg\,s}^{-1}\,\mathrm{cm}^{-2}\,\mathrm{arcsec}^{-2}$.

6.4.1 Surface Brightness

In our model, Lyα photons propagate outward through the diffusion process in both spatial and frequency domains until they can escape the system. The spatial diffusion renders a central Lyα point source into extended Lyα halos. Naturally, the more Lyα photons experience scattering, the more extended surface brightness profile emerges. To investigate the properties of Lyα halos resulting from the Model S, we extract radial surface brightness profiles as
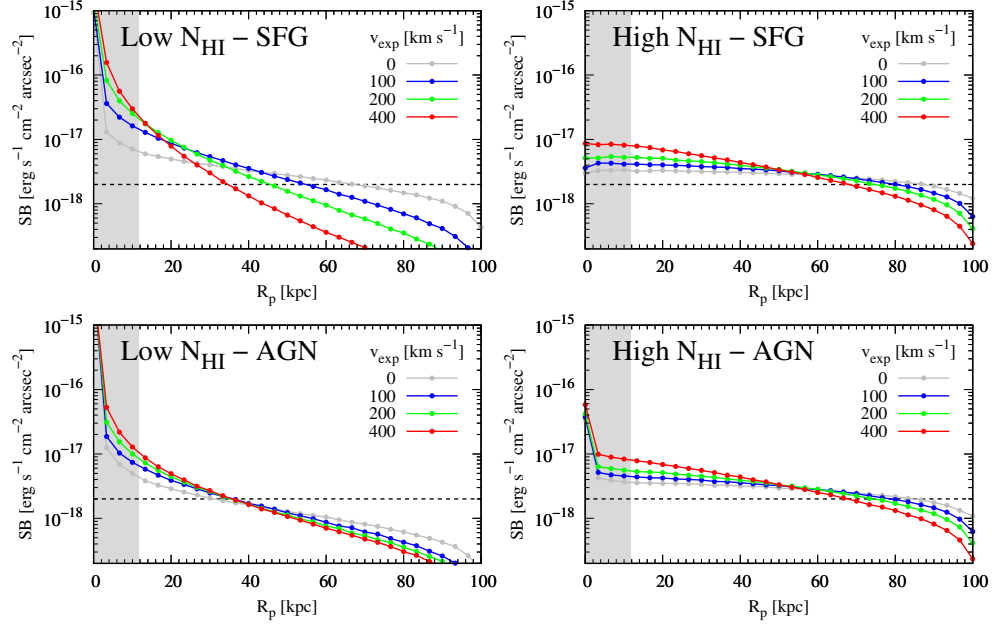
Figure 6.4: The surface brightness profiles for $v_{\mathrm{exp}} = 0 - 400\,\mathrm{km\,s^{-1}}$. The structure is similar in Figure 6.3. 'Low N_{HI}' (left panels) and 'High N_{HI}' (right panels) mean $N_{\mathrm{HI}} = 10^{19}$ and $10^{21}\,\mathrm{cm^{-2}}$.

a function of the projected distance from the center, $R_p = \sqrt{x_p^2 + y_p^2}$. Our findings are:

- The surface brightness profile becomes more extended with increasing N_{HI} and decreasing v_{exp}, respectively.

- The SFG cases produce more extended halos than the AGN cases except when outflow is very strong ($v_{\mathrm{exp}} \sim 400\,\mathrm{km\,s^{-1}}$).

- The surface brightness profiles become less extended with higher concentrations of the scattering medium (i.e., smaller R_e/R_H). However, the dependence on the R_e is comparably weaker than other parameters.
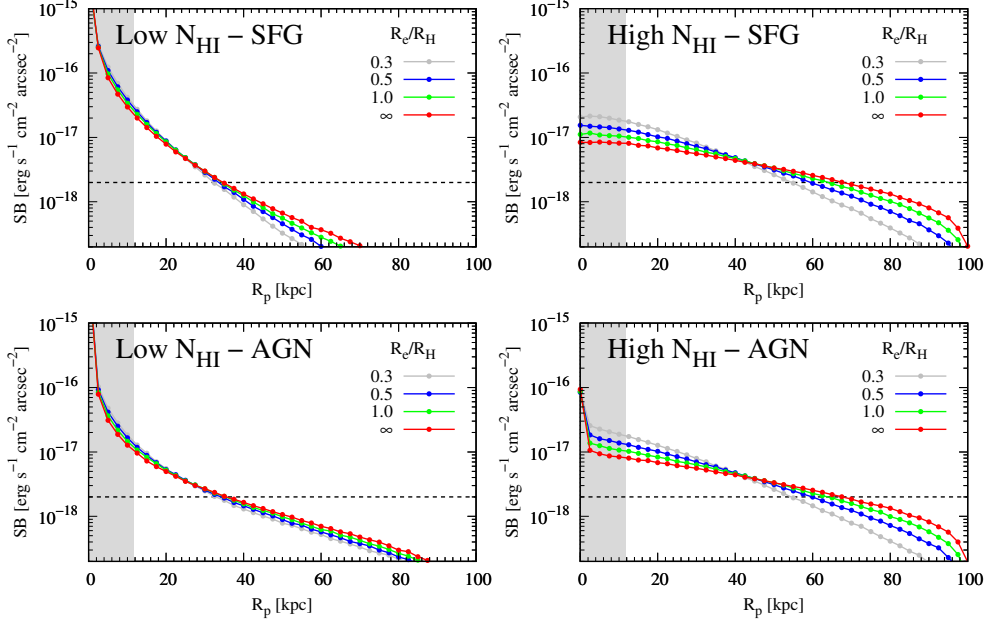
Figure 6.5: The surface brightness for $R_e = 0.3R_H - \infty$ with strong outflow, $v_{\exp} = 400\,\mathrm{km\,s^{-1}}$. The structure is similar in Figure 6.4.
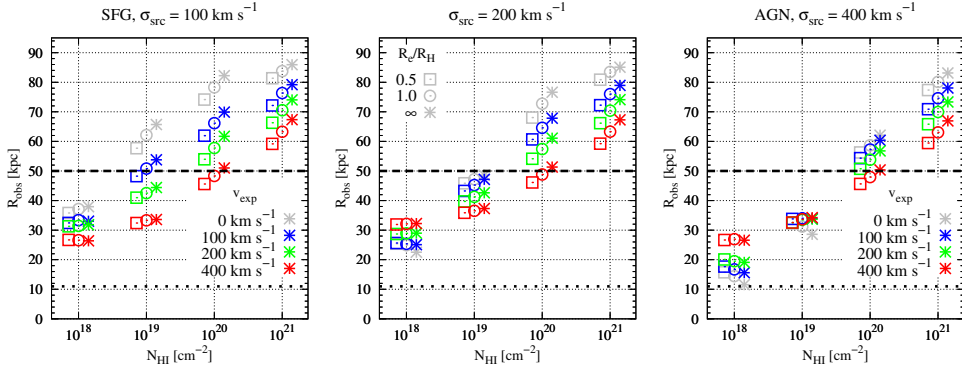
Figure 6.6: The observable radius R_{obs} for $\sigma_{\mathrm{src}} = 100\,\mathrm{km\,s^{-1}}$ (SFG), 200 $\mathrm{km\,s^{-1}}$, 400 $\mathrm{km\,s^{-1}}$ (AGN). The color and shape of marks represent $v_{\exp}$ and R_e, respectively. The dotted vertical lines represent the radius of Lyα halo considering only seeing effect without scattering ($R_{obs} = 12\,\mathrm{kpc}$). The dashed black lines are $R_e = 50\,\mathrm{kpc}$.

- At the high column density ($N_{\mathrm{HI}} = 10^{21} \, \mathrm{cm}^{-2}$), the surface brightness profiles become very flat and show a significant dependence on v_{exp} and R_e regardless of the source types (SFG vs. AGN case).

- The size of Lyα halo in the Model S becomes extended over $\sim$100 kpc as long as $N_{\mathrm{HI}} \geq 10^{20} \, \mathrm{cm}^{-2}$.

6.4.1.1 Dependence on Column Density

We find that the surface brightness profiles become more extended with increasing column density (N_{HI}) due to the increased number of scattering. Figure 6.3 shows how the surface brightness profiles change as a function of N_{HI} from 10^{18} to 10^{21} cm^{-2} for different combinations of outflow speeds and input Lyα sources. As N_{HI} increases, all profiles become more extended, and the resulting halos will be observed larger.

Depending on how much the input Lyα photons are scattered off from the sight-line, the morphology of Lyα halos can vary. In the case of the SFG with low column density ($N_{\mathrm{HI}} \leq 10^{20}$), Ly$\alpha$ photons from the central source can directly escape the system without much scattering; thus, the spatial profile near $R_p = 0$ is very peaky like a point-source. In other words, observers can see the input source directly through the scattering medium. This is also true for both the (Static – AGN) and (Outflow – AGN) cases. Note that these bright point-sources will be observed as bright cores in ob-

servation due to the seeing or point spread functions as indicated by the shaded gray regions ($R_p \lesssim 10$ kpc; ~ 1) in Figure 6.3.

As N_{HI} increases further in the Static – SFG case ($N_{\mathrm{HI}} = 10^{21}\,\mathrm{cm}^{-2}$) or Outflow – SFG cases, it takes more scatterings for photons to escape the system and the surface brightness profile becomes more extended and flatter. In these scattering-dominated cases, one cannot see the input source directly through the gas halo, but only the scattered photons as a diffuse halo.

We note that the fore-mentioned polarization jump originates because these directly escaping photons dilute any polarized signal near the center of halos. In Section 6.4.2, we show that the bright core and polarization jump co-exist.

6.4.1.2 Dependence on Outflow Speed (v_{exp})

The surface brightness profile becomes more extended and flattened with decreasing v_{exp}. Figure 6.4 shows variation of the surface brightness profiles as a function of v_{exp} (0, 100, 200, 400 $\mathrm{km\,s}^{-1}$) for four different combinations of column densities (high/low case for $10^{19}/10^{21}\,\mathrm{cm}^{-2}$) and input Ly$\alpha$ sources (SFG and AGN). This dependence can be understood as follows. As we will describe the Lyα spectrum in Section 6.4.3, when the scattering occurs in an outflowing medium compared to a static one, photons can escape the system more easily due to large changes in the wavelength after scattering.

Thus the photons see smaller optical depth, experience smaller number of scattering, and escape the system at a distance closer to the center.

However, we note that this dependence of the spatial extent on v_{exp} could be different depending on the input sources (σ_{src}). We find that the surface brightness profile shows largest dependence on v_{exp} in the low column density ($N_{\mathrm{HI}} \leq 10^{19}\,\mathrm{cm}^{-2}$) and SFG case where v_{exp} can be larger than the width of the input Lyα emission (σ_{src}). For example, the surface brightness profiles of the SFG case are more sensitive to v_{exp} than those of the AGN case (see low N_{HI} column in Figure 6.4). The profiles of the AGN and low N_{HI} case in the left bottom panel are almost indistinguishable. Furthermore, we note that the dependence on v_{exp} could be even inverted as we will discuss in Section 5.4.1.6.

6.4.1.3 Dependence on Input Sources (σ_{src})

In general, the surface brightness profile of the SFG case is more extended than those of the AGN case at the same N_{HI} and v_{exp} (Static cases in Figure 6.3 left). In the AGN case with $\sigma_{\mathrm{src}} = 400\,\mathrm{km\,s}^{-1}$, there could be photons with wavelength much further from the line center of the scattering medium; therefore these photon easily escapes due to the smaller optical depth.

The only exception is when the outflow speed is high enough for photons at the velocity wings of AGN to be effectively scattered by the medium.

In this case, the surface brightness profile of the AGN case is more extended than those of the SFG case. In Figure 6.7, we compute the optical depth of initial photons for $v_{\mathrm{exp}} = 0-400\,\mathrm{km\,s^{-1}}$ as a function of wavelength. Even at $N_{\mathrm{HI}} < 10^{19}\,\mathrm{cm^{-2}}$, the fast-moving outer halo can scatter the initial photons at the wavelength blueward from 0 to $-v_{\mathrm{exp}}$. In the right panels of Figure 6.3 with $v_{\mathrm{exp}} \sim 400\,\mathrm{km\,s^{-1}}$, the surface brightness profile for the AGN case with $N_{\mathrm{HI}} \leq 10^{19}\,\mathrm{cm^{-2}}$ becomes more extended than the SFG case.

6.4.1.4 Dependence on Concentration (R_e)

The surface brightness profile becomes more extended with increasing effective radius (R_e), with a uniform halo being most extended. In other words, the Lyα halo looks more extended for a more extended scattering medium. However, this dependence is significant only for large column densities. Figure 6.5 shows the surface brightness profile for $R_e/R_H = 0.3$, 0.5, 1.0, and ∞ for the four combinations. Note that a uniform distribution corresponds to a limiting case of $R_e/R_H \to \infty$. In the regime of the low column density ($N_{\mathrm{HI}} = 10^{19}\,\mathrm{cm^{-2}}$), the dependence on R_e is negligible. In the high column density case ($N_{\mathrm{HI}} = 10^{21}\,\mathrm{cm^{-2}}$), the surface brightness profiles show a significant variation with increasing R_e. This is because N_{HI} is large enough to make photons scattered even at the outer radii.

6.4.1.5 High Column Density Case

We confirm that the surface brightness profile with high column density ($N_{\mathrm{HI}} \sim 10^{21}\,\mathrm{cm}^{-2}$) depends on two geometrical parameters, v_{exp} and R_e, regardless of σ_{src}. The halo with the high column density erases the information of the intrinsic Lyα emission. In the right panels of Figure 6.4, the profiles become more extended with decreasing v_{exp}. The upper and lower right panels for SFG and AGN cases show similar extended profiles without a small central bright core in the AGN case. At $N_{\mathrm{HI}} = 10^{21}\,\mathrm{cm}^{-2}$, the scattering continuously occur despite the photon is far from the line center, $\gtrsim 1,000\,\mathrm{km\,s}^{-1}$. As a result, in the right panels of Figure 6.4, the surface brightness profiles in the static medium look like a flat slope. The photon quickly escapes through significant wavelength variation by scattering in a fast-moving medium. The escaping photon's average distance from the halo's center is 0.90, 0.80, 0.72, and 0.63R_H for $v_{\mathrm{exp}} = 0$, 100, 200, and 400$\,\mathrm{km\,s}^{-1}$, respectively. In the right panels of Figure 6.5, the surface brightness profiles become more extended with increasing R_e. The dependence of R_e in the right panels is stronger than the left panels for the low column density. The high column density ($N_{\mathrm{HI}} = 10^{21}\,\mathrm{cm}^{-2}$) is high enough to cause the significant scattering in the outer H I halo. Hence, the decreasing probability of the outer scattering by R_e affects the formation of Lyα halo.

6.4.1.6 When Large Lyα Halos Are Produced by Scattering?

To investigate when scattering by the neutral gas around galaxies or AGNs can produce large Lyα halos such as the Lyα blobs or ELANe (e.g., REF), we measure the size of Lyα halo from each model library. We define an observed halo radius R_{obs} as a distance from the center to a fixed observational threshold (SB $= 2 \times 10^{-18}$ erg s^{-1} cm^{-2} arcsec^{-2}) corresponding to horizontal dashed lines in Figures 6.3 – 6.5. Figure 6.6 shows R_{obs} as a function of N_{HI} for three types of sources, $\sigma_{\mathrm{src}} = 100$ (SFG), 200, and 400 km s^{-1} (AGN), respectively. In each panel, we also show the dependence of R_{obs} on R_e/R_H (three different symbols) and v_{exp} (different colors), respectively. If this size is comparable to 50kpc in a model, we regard this model as a LAB or ELAN.

   As we discussed above, the most dominant factor to determine the size of the scattered halo is the H I column density (N_{HI}). In SFG cases with $N_{\mathrm{HI}} = 10^{18-19}$ cm^{-2} (left panel), R_{obs} also shows strong dependence on v_{exp}: the smaller v_{exp}, the larger Lyα halos. The concentration of the scattering medium (R_e/R_H) is the most marginal parameter affecting the halo size. If $N_{\mathrm{HI}} \geq 10^{20}$ cm^{-2}, the profiles always become extended out to $R_{obs} \sim 50$ kpc, thus the system will be observed as typical Lyα blobs with $L(\mathrm{Ly}\alpha) = 10^{44}$ erg s^{-1}. In particular, in the AGN case, the total column density (N_{HI}) is almost the only dominant factor to produce $R_{obs} > 50$ kpc. Otherwise, for

the low – intermediate column densities with $N_{\mathrm{HI}} = 10^{18-19}\,\mathrm{cm}^{-2}$, the system should have a SFG-like σ_{src} (100–200 km s^{-1}) *and* weak outflow speed ($v_{\mathrm{exp}} \sim 100$ km s^{-1}) together to be observed as large Lyα halos.

Note that as we will discuss in Section **??**, in the $\sigma_{\mathrm{src}} \geq 200$ km s^{-1} cases, the size dependence on v_{exp} become inverted — large outflow produce larger halos — at the low column density. Regardless of σ_{src}, we find that R_{obs} at $N_{\mathrm{HI}} = 10^{21}\,\mathrm{cm}^{-2}$ shows similar behavior with increasing v_{exp} and R_e.

6.4.2 Polarization

Lyα scattering processes include single and multiple wing scattering and core scatterings. The polarization in our models can be explained by relative contributions of these scattering types. Here we summarize our findings for our model libraries and discuss the principles and polarization patterns in detail below:

- Polarization jump occurs when single wing scattering dominates the escape of Lyα photons: at $N_{\mathrm{HI}} \lesssim 10^{19}\,\mathrm{cm}^{-2}$ in the SFG case and at $10^{20}\,\mathrm{cm}^{-2}$ in the AGN case, respectively.

- At $N_{\mathrm{HI}} \sim 10^{21}\,\mathrm{cm}^{-2}$, the polarization behavior is dominated by geometrical parameters, v_{exp} and R_e, regardless of the width of Lyα emission.
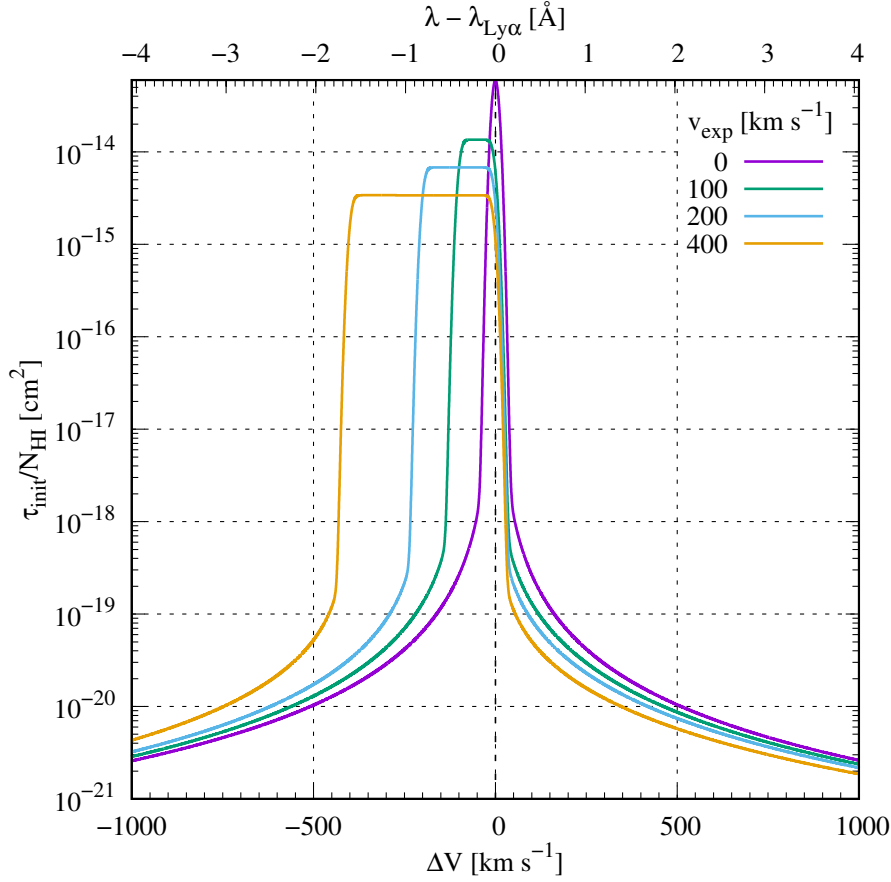
Figure 6.7: The optical depth of the uniform halo τ_{init} as a function of λ. The y-axis is $\tau_{init}/N_{\mathrm{HI}}$ in logarithmic scale as τ_{init} is proportional to N_{HI} in the uniform density halo (i.e. $R_e = \infty$). The upper and lower x-axis is the wavelength and Doppler shift from the line center. The color of solid lines represents the various v_{exp}.

- Due to the relative contributions of three scattering types, the polarization profile is very complex and does not behave monotonically with N_{HI}, v_{exp}, and σ_{src}.

- The overall degree of polarization increases to a characteristic N_{HI} values, then decreases.
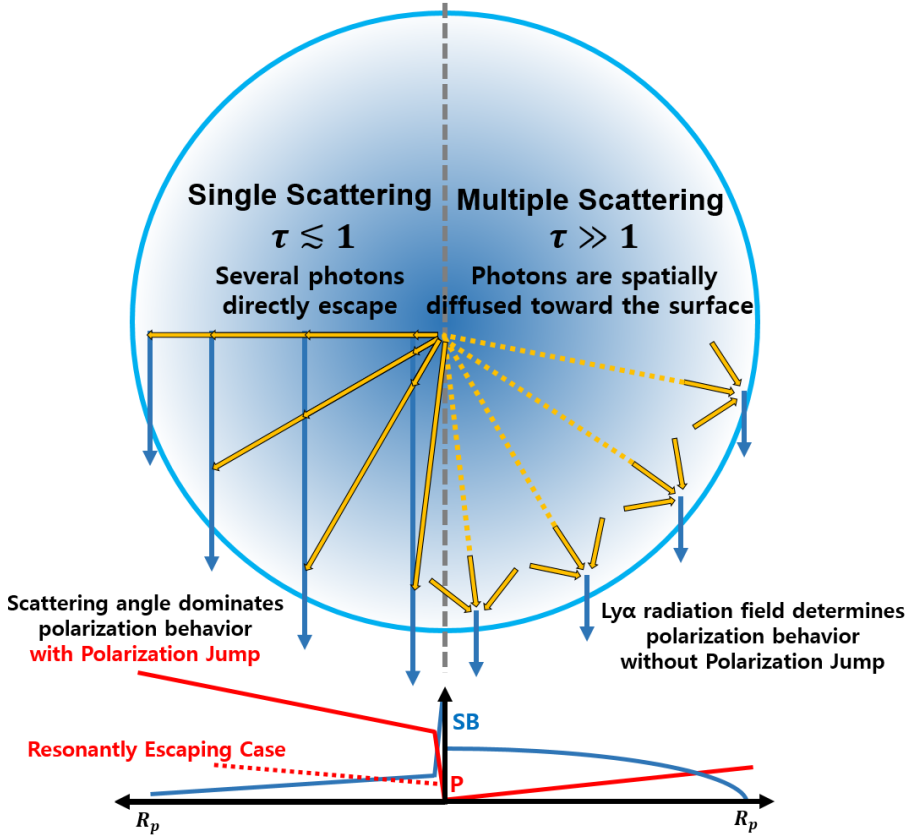
Figure 6.8: The schematic illustrations for the case dominated by single (left side) and multiple (right side) scattering. The blue arrows represent the direction of the photon escaping from the H I halo. The yellow arrows represent the incident direction of the photon at last scattering. In single scattering case, the photon can escape with large scattering angle from the deep halo. The polarization is induced by the degree of polarization of individual photon packet with the scattering angle near 90°. The bright core and polarization jump exist in this case. In multiple scattering case, the photon is continuously diffused toward the surface of the halo. The flattened surface brightness profile and the gradually increasing polarization appear. The polarization is induced by the radiation field of multiply scattered photons near the surface.

- The overall degree of polarization profile increases with increasing $v_{\exp}$,

  except the outflowing case with the low column density ($N_{\mathrm{HI}} \sim 10^{18}\,\mathrm{cm}^{-2}$).
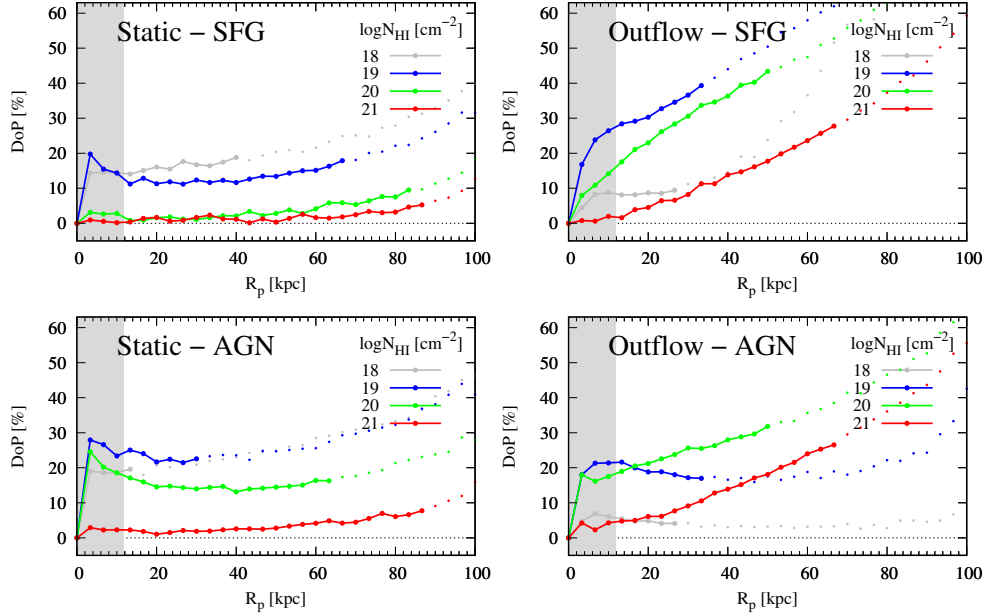
Figure 6.9: The profiles of the degree of polarization by the projected radius R_p for $N_{HI} = 10^{18-21}\,\mathrm{cm}^{-2}$ at $R_e = \infty$. The y-axis is the degree of polarization, $= \sqrt{Q^2 + U^2}/I$. The structure is similar in Figure 6.3. The color dots with/without solid lines represent the surface brightness over/under the dashed lines in Figure 6.3.

6.4.2.1 Polarization of Scattered Lyα Photons

Before we describe polarizations in the Model S in detail, we first explain the polarization behavior of the single and multiple scattering cases in this section. Figure 6.8 shows the schematic illustration for the cases where single ($\tau \lesssim 1$) and multiple ($\tau \gg 1$) scattering dominates.

It is the initial wavelength of a photon from the central source that ultimately determines the subsequent journey in the radiative process, especially at the low column density ($10^{18-19}\,\mathrm{cm}^{-2}$). To illustrate this, in Figure
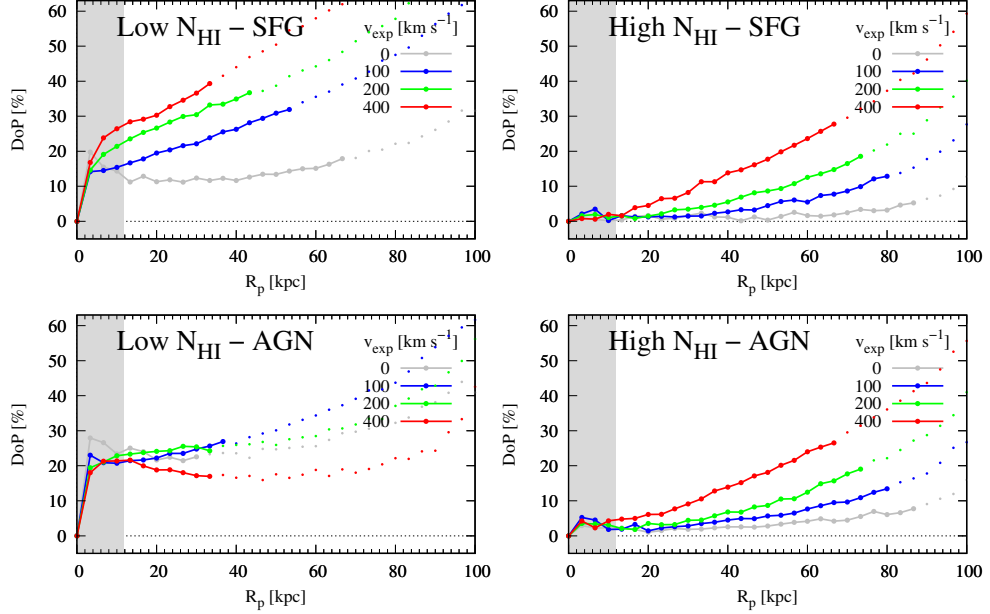
Figure 6.10: The profiles of the degree of polarization for $N_{\mathrm{HI}} = 10^{18-21}\,\mathrm{cm}^{-2}$ at $R_e = \infty$. The parameters in each panels are identical with Figure 6.4.

6.7 we show the optical depth of an initial photon τ_{init} in a uniform halo as a function of wavelength/velocity for different expanding velocities. We choose to plot $\tau_{init}/N_{\mathrm{HI}}$ at the y-axis because τ_{init} is proportional to N_{HI}. The Lyα cross section of atomic hydrogen follows the Voigt profile. In our models, the intrinsic width of Lyα emission and the outflow velocity is much larger than the thermal motion ($\sim 13\,\mathrm{km\,s^{-1}}$). The τ_{init} is extremely high and flat in the velocity range $\Delta V = -(v_{\mathrm{exp}} + v_{th})$ to $+v_{th}$. Outside this region, the τ_{init} dramatically decreases and becomes the Lorentzian function. The two regions, the flat and Lorentzian-like regions, are referred to as "core" and "wing" regions, respectively. In the low column density ($N_{\mathrm{HI}} \leq 10^{19}\,\mathrm{cm}^{-2}$),
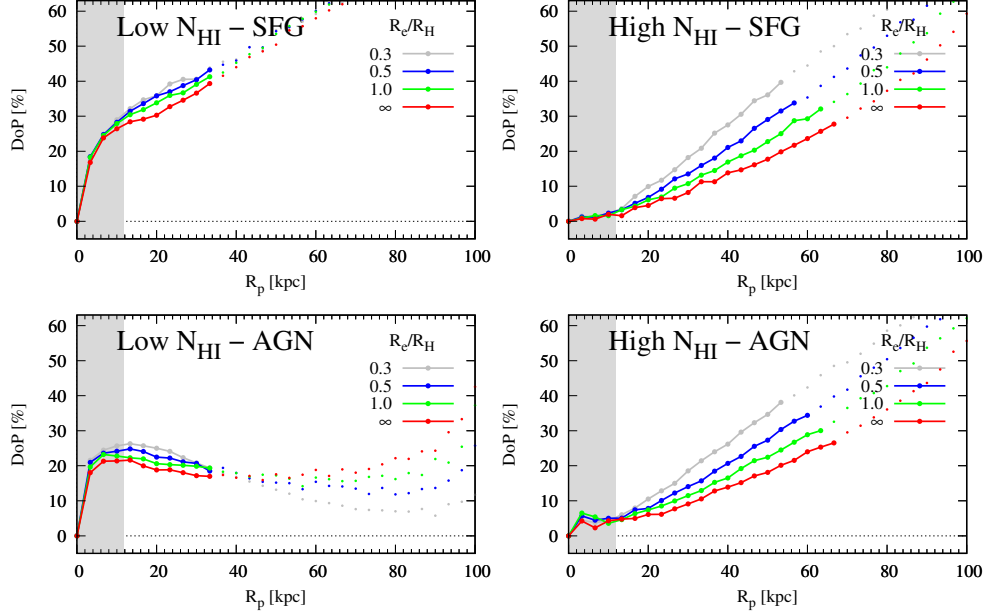
Figure 6.11: The profiles of the degree of polarization for $R_e = 0.3R_H - \infty$ at $v_{\exp} = 400\,\mathrm{km\,s^{-1}}$. The parameters in each panels are identical with Figure 6.5.
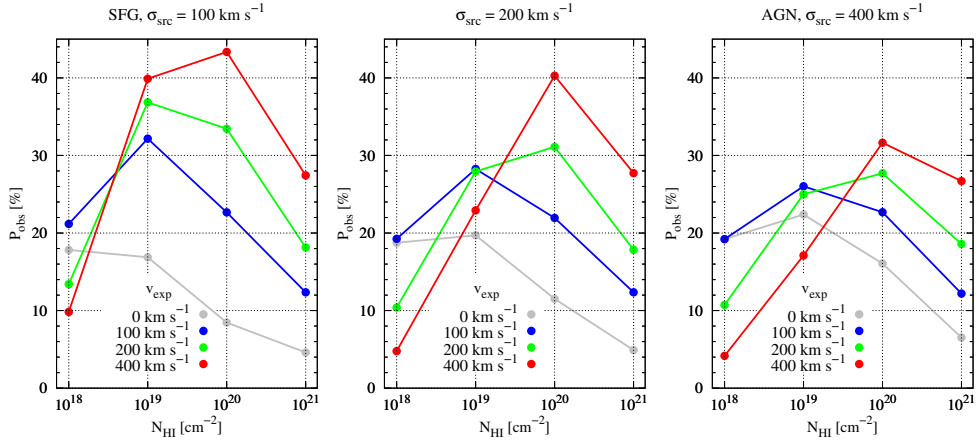
Figure 6.12: The degree of polarization at observable radius R_{obs} for $\sigma_{\mathrm{src}} = 100\,\mathrm{km\,s^{-1}}$ (SFG), $200\,\mathrm{km\,s^{-1}}$, $400\,\mathrm{km\,s^{-1}}$ (AGN). The color and shape of marks represent $v_{\exp}$ and R_e, respectively.

the photon in the wing region is optically thin, and single scattering domi-nates. The photon in the core region has to random-walk to the wing region through several scattering to escape the H I halo.

The type and angle of scattering determine the polarization state of scattered Lyα photon packet (Dijkstra & Loeb 2008; Chang et al. 2017; Eide et al. 2018). Two scattering types are resonance (core) and Rayleigh (wing) scattering. The photon after Rayleigh scattering maintains the de-gree of polarization in forward and backward scattering cases or develops intense polarization if the scattering angle is closed to 90°. Resonance scat-tering produces unpolarized light ($1s_{1/2} - 2p_{1/2}$ transition) or weak polariza-tion ($1s_{1/2} - 2p_{3/2}$ transition). Therefore, if the single wing scattering dom-inates in the model, the scattering angle is the key parameter that deter-mines the overall polarization (Chang et al. 2017). On the other hand, if the photon experiences multiple wing scatterings, most individual photon packets are entirely polarized ($\sim 100\%$). In this case, the anisotropy of Lyα radiation field determines the polarization (Seon et al. in prep). In the case that the core scattering dominates, the photon packets can be weakly po-larized (singly scattered) or unpolarized (multiple scattering) depending on the number of scatterings.

6.4.2.2 Polarization Jump from Single Wing Scattering

We find that *polarization jump* originates from the singly wing-scattered photons. In the left side of Figure 6.8, we schematically illustrate how polarization jump is developed when the single scattering dominates in the low column density. The photons projected at $R_p \sim 0$ are composed of the directly escaping unpolarized photons and the photons scattered by the medium. Due to spherical symmetry, the degree of polarization exactly at the center should be zero even if the line-of-sight can include polarized scattered photons. When the line-of-sight slightly diverges from the center, the symmetry is broken, and the scattered photon with the scattering angle closed to 90° induces strong polarization. As a result, the degree of polarization steeply increases at the right off-center. From here, the degree of polarization increases radially outward because the fraction of scattered photons with scattering angles near 90° increases.

Because the directly escaping photons from the central sources are the main reason for the polarization jump, we find that the single scattering case shows the bright core + faint halo morphology at the same time. Theoretically, this polarization jump is interesting; however, the polarization jump might be hard to observe because the seeing would erase any steep gradient, and the spherical symmetry can be easily broken in the realistic environment.

6.4.2.3 Polarization Profile from Multiple Wing Scattering

In an optically thick case where multiple wing scattering dominates, a gradually increasing polarization pattern emerges without a polarization jump. Figure 6.9 shows the degree of polarization for $N_{\mathrm{HI}} = 10^{18-21}\,\mathrm{cm}^{-2}$ and the combinations of v_{exp} and σ_{src}. The solid lines represent the region within the observable halo radius R_{obs} above the surface brightness threshold, while the unconnected dots indicate the area beyond the R_{obs} where observations of the surface brightness and polarization would be extremely challenging. In the high column density ($N_{\mathrm{HI}} = 10^{21}\,\mathrm{cm}^{-2}$), all profiles are gradually and monotonically increasing from 0% at the center to 10–30% at the R_{obs}.

This polarization behavior can be understood as illustrated in the right side of Figure 6.8. In the extremely optically thick case like the static halo with the high column density ($N_{\mathrm{HI}} = 10^{21}\,\mathrm{cm}^{-2}$), most Ly$\alpha$ photons are spatially diffused toward the halo's surface through the wing scattering, then scattered for the last time before reaching to an observer. In other words, the last scattering surface of the observed photons is close to the boundary of the halo. In this case, the surface brightness profile becomes very flat due to a large number of scattering, and we can only see the surface of the halo. Before this last scattering atom, the radiation field of multiply scattered photons becomes anisotropic because there are no Lyα photons beyond this radius. In other words, The symmetry of the radiation field is gradually

broken from the deep inside the halo to the radially outward. . As the line-of-sight is diverging from the center, the scattering angle of the photons are more likely close to 90, therefore higher polarization results as R_p increases. Because even in the vicinity of the center, almost all Lyα photons are scattered at least once (actually a lot), therefore the photon packets carry at least some degree of polarization, thus no polarization jump exist.

In the static medium case (left panels), we find that the degree of polarization profiles for $N_{\rm HI} = 10^{21}\,{\rm cm}^{-2}$ (red solid lines) gradually increase from zeros and reach to a maximum value of $\approx 11.7\%$ at $R_p = 100\,{\rm kpc}$. . This gradually increasing polarization is analogous to the polarization behavior in the optically thick semi-finite slab. Using an analytic solution, Chandrasekhar (1960) shows that the polarization increases to $\approx 11.7\%$ in the Thomson thick slab. Chang et al. (2017) also reproduces this polarization behavior for the Rayleigh thick slab using a numerical method employing the density matrix formula.

6.4.2.4 Effect of Core Scattering

One of the key features of our RT calculation is the consistent treatment of core scattering. Here, we emphasize that the core scattering must be considered properly in Lyα radiative transfer to calculate polarization. If core scattering is not included in the calculation, the overall degree of polariza-

tion must increase with decreasing N_{HI} because single wing scattering occurs more frequently as N_{HI} decreases. However, on the contrary, Figure 6.2 shows that the overall degree of polarization with $N_{\mathrm{HI}} = 10^{18}\,\mathrm{cm}^{-2}$ is *smaller* than that of $10^{19}\,\mathrm{cm}^{-2}$ case. We attribute this behavior to the fact that there is a large number of photons that escape through core scattering due to the small optical depth. In Figure 6.7, if $N_{\mathrm{HI}} \sim 10^{18}\,\mathrm{cm}^{-2}$, τ_{init} is much smaller than unity in wing region. The initial photons directly escape in the wing region. The photons in the core region escape going through only core scattering.

The core scattering affects the polarization behavior significantly at low column density ($N_{\mathrm{HI}} \lesssim 10^{19}\,\mathrm{cm}^{-2}$). In the right panels of Figure 6.9, we find that resonantly escaping photon reduces the overall degree of polarization at $N_{\mathrm{HI}} = 10^{18}\,\mathrm{cm}^{-2}$. Similarly, if the strong outflow medium surrounds the broad emission, the reasonable fraction of the core escaping photon induces a decrease in the degree of polarization. In the left bottom panel of Figure 6.10, we confirm that the overall degree of polarization with the low column density ($N_{\mathrm{HI}} = 10^{19}\,\mathrm{cm}^{-2}$) become weaker with increasing v_{exp}. The effect of core scattering is negligible at $N_{\mathrm{HI}} > 10^{19}\,\mathrm{cm}^{-2}$. In this high N_{HI} regime, the spatial diffusion by core scattering is negligible. The photons have to go through wing scattering to escape from the H I halo.

6.4.2.5 Polarization Dependence on Model Parameters

Polarization Jump. We find that polarization jump is strongest at $N_{\rm HI} \sim$ $10^{19}\,{\rm cm}^{-2}$ regardless of $\sigma_{\rm src}$. In Figure 6.9, the polarization jump disappears at $N_{\rm HI} > 10^{19}$ and $N_{\rm HI} > 10^{20}\,{\rm cm}^{-2}$ in SFG and AGN cases, respectively. This is because polarization jump originates from high contribution of single wing scattered photons. Figure 6.10 and 6.11 show how the polarization profile changes for a range of $v_{\rm exp} = 0 - 400$ and $R_e/R_H = 0.3 - 1$, ∞, respectively. In the low $N_{\rm HI}$ cases ($10^{19}\,{\rm cm}^{-2}$; left panels), we find that the level of polarization jump is $\sim 20\%$, which is not sensitive to $v_{\rm exp}$ and R_e.

While polarization jump is not expected generally in high $N_{\rm HI}$, we note that small polarization jump can still exist if input Lyα spectrum has enough photons in the wing region. In the high $N_{\rm HI}-$ AGN cases (bottom right panels of Figure 6.10 and 6.11), we find small polarization jumps at $\sim5\%$ level, although this small jump would be hard to observe. As we discuss in Figure 6.4 and 6.5, the bright cores are still visible in this case confirming that the core + halo morphology and the polarization co-exist.

Non-monotonic Polarization Profile We find that the degree of polarization does not always increase monotonically as a function of projected radius (R_p). If Lyα photons escape the system via only one type of scattering mechanism or an RT calculation includes one scattering mechanism, the

degree of polarization profile would always increase radially outward. How-
ever, in our simulation, the relative contribution of singly and multiply scat-
tered photons determines the polarization profile. For example, in the Static
– SFG case with $N_{\mathrm{HI}} = 10^{19}\,\mathrm{cm}^{-2}$ (top left panel of Figure 6.9), the polar-
ization decreases to ∼10% after the high polarization jump (20%) and in-
creases gradually again. This non-monotonic behavior is also observed in the
Static – AGN case with $N_{\mathrm{HI}} = 10^{20}\,\mathrm{cm}^{-2}$. In these cases, the polarization
behavior is dominated by the single scattering at the center's vicinity and
by the multiple scattering at the outer halo. The relative contribution of the
single and multiple cases becomes more complex with increasing σ_{src}.

Dependence on v_{exp}. We find that the dependence of the polarizations
on the v_{exp} is complex and also not monotonic. In Figure 6.12, we measure
the degree of polarization P_{obs} at the observable halo radius R_{obs} for three
input sources, $\sigma_{\mathrm{src}} = 100,\ 200,\ 400\ \mathrm{km\,s}^{-1}$.

In high N_{HI} cases ($\geq 10^{20}$ cm^{-2}), the overall degree of polarization
tends to increase with increasing v_{exp} for all three input sources because
the photons can easily escape due to large changes in wavelength induced
by the fast-moving medium. As shown in Figure 6.7, τ_{init} in the wing re-
gion decrease as the outflow becomes stronger. The decrease of the optical
depth in the wing region allows more photons to escape through single wing

scatterings, thus increases the overall polarization strength. In the top left panel of Figure 6.10, we show that the overall degree of polarization for the SFG case in $N_{\mathrm{HI}} = 10^{19}\,\mathrm{cm}^{-2}$ increase from $P_{obs} \sim 30\%$ to 40% when v_{exp} increase from $100\,\mathrm{km\,s}^{-1}$ to $400\,\mathrm{km\,s}^{-1}$.

However, this P dependence on v_{exp} becomes inverted for low column density ($N_{\mathrm{HI}} = 10^{18}$) due to the increased contribution of photons escaping through core scatterings. In the intermediate column density ($N_{\mathrm{HI}} \sim 10^{19}\,\mathrm{cm}^{-2}$), P_{obs} shows the complex dependence on v_{exp} because the relative contribution of single, multiple wing scatterings and core scattering changes in complex way depending on v_{exp} and σ_{src}. Note that the exact N_{HI} values at which this inversion occurs are different for different input sources (σ_{src}). In the low N_{HI}– AGN case ($N_{\mathrm{HI}} = 10^{19}\,\mathrm{cm}^{-2}$; the bottom left panel), the polarization profile for $v_{\mathrm{exp}} = 400\,\mathrm{km\,s}^{-1}$ is about $\sim 10\%$ smaller than other v_{exp}'s. In this outflow medium, the broad input Lyα emission increases the contribution of core escaping photon.

Dependence on R_e. Similar to the case of strong outflows, the large density concentration allows the photons to escape from the deeper region in the halo. Note that higher concentration at the fixed column density or mass implies that the density declines faster than those with low concentration. The symmetry of the radiation field is more broken when the number of photons

escaping from the more inner halo increases . Therefore, we confirm that the overall degree of polarization increase with decreasing R_e.

6.4.3 Spectrum
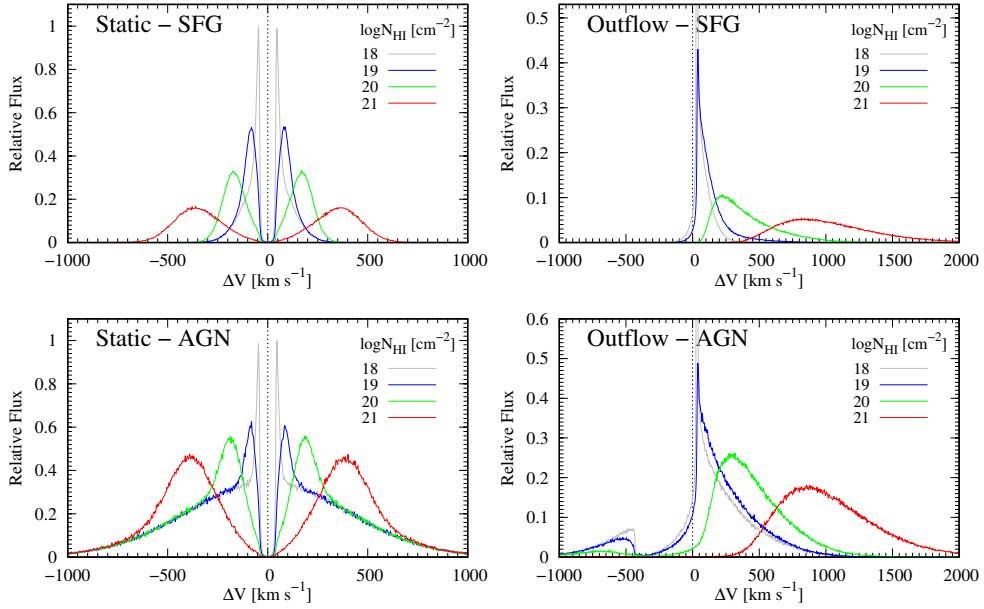
Figure 6.13: The total integrated Lyα spectra for $N_{\mathrm{HI}} = 10^{18-21}\,\mathrm{cm}^{-2}$. The y-axis is the value divided by the peak value of the gray solid line ($N_{\mathrm{HI}} = 10^{18}\,\mathrm{cm}^{-2}$). The x-axis is Doppler shift from the line center ΔV. The parameters in each panel are identified with Figure 6.3.

6.4.3.1 Formation of Lyα Spectrum

Before we describe Lyα spectra in detail, we briefly explain the formation of Lyα spectrum by scattering in this section. Scatterings cause not only spatial diffusion but also broadening and shift of Lyα emission lines. In the static medium, the wavelength of the scattered Lyα photon changes by ran-
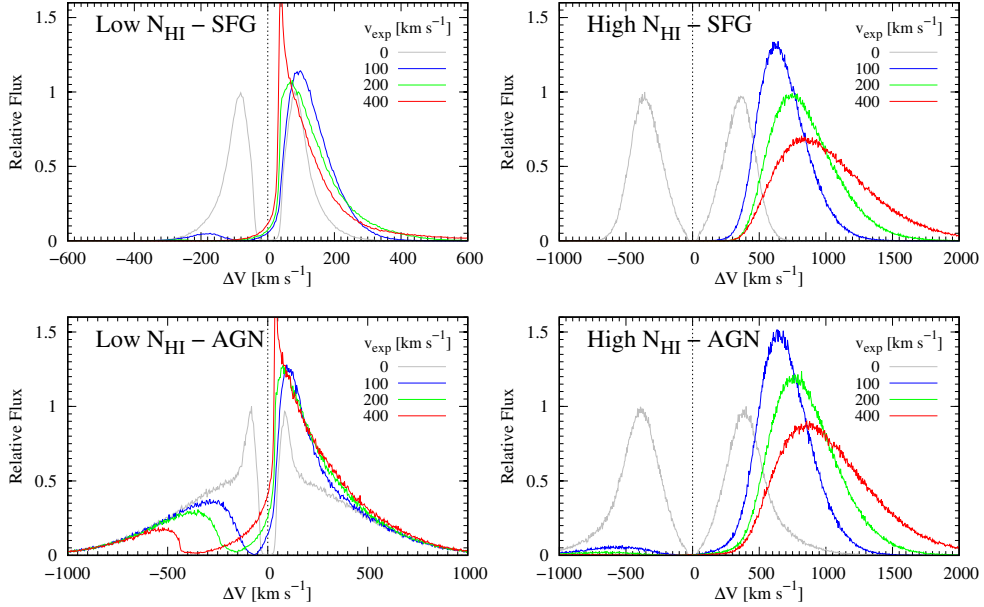
Figure 6.14: The total integrated Lyα spectra for the parameters identified with Figure 6.4.

dom amounts from one scattering to another, and the width of these changes is determined by the thermal motion of atoms. The spectrum from static medium shows characteristic symmetric double peaks. The width of two peaks and the separation between peaks become larger with increasing optical depth (e.g., Neufeld 1990; Ahn et al. 2002). In an outflowing medium, the wavelength of the scattered Lyα photon can be changed by the amount comparable to the expanding velocity. When Lyα photons experience scatterings in the outflowing medium, the spectrum becomes a red enhanced asymmetric profile (Zheng & Miralda-Escudé 2002; Verhamme et al. 2006; Dijkstra & Loeb 2008). Figure 6.13 shows the integrated Lyα spectra for
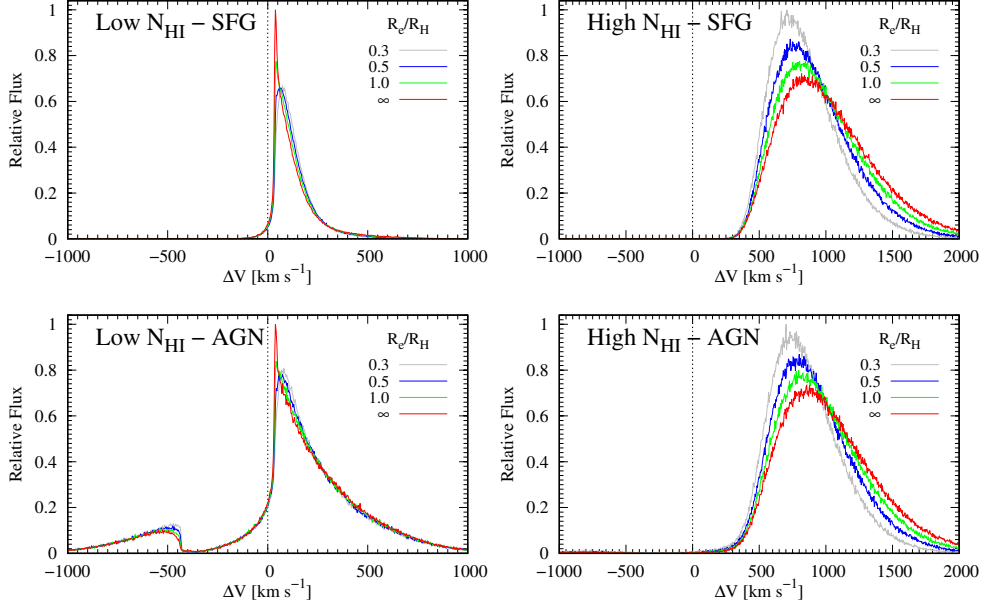
Figure 6.15: The total integrated Lyα spectra for the parameters identified with Figure 6.5.
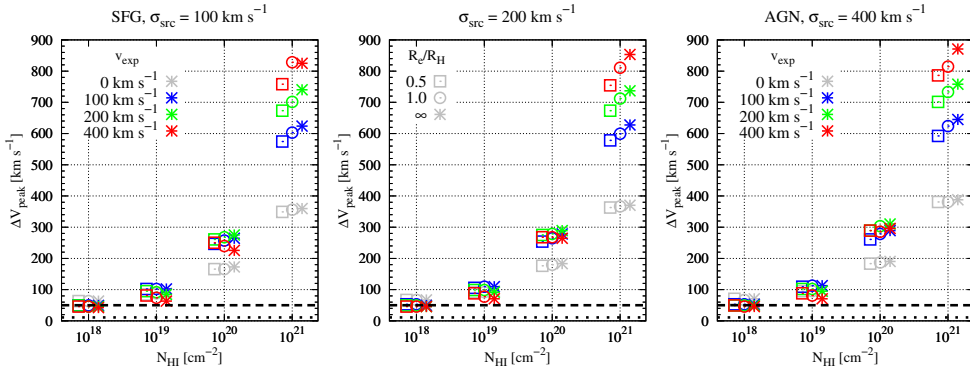
Figure 6.16: The velocity offset of the line peak for $\sigma_{\mathrm{src}} = 100\,\mathrm{km\,s^{-1}}$ (SFG), $200\,\mathrm{km\,s^{-1}}$, and $400\,\mathrm{km\,s^{-1}}$ (AGN). The color and shape of marks represent v_{exp} and R_e, respectively.

$N_{\mathrm{HI}} = 10^{18-21}\,\mathrm{cm^{-2}}$ and the combinations of v_{exp} and σ_{src}. We confirm that

the spectra are broadened with increasing N_{HI} at the same v_{exp}. The static

(left) and outflow medium (right panels) show double-peaked and red asym-

metric profiles, respectively.

In our model, we adopt a Hubble-like velocity field with the outflow velocity proportional to the distance from the central source. In this case, unlike a typical shell geometry often studied in the past (Dijkstra & Loeb 2008), the scattered photons are always redshifted, as explained below. The scattering medium is always expanding at any position toward any line of sight. Thus, the optical depth profile follows the profile similar to τ_{init} in Figure 6.7. The optical depth profile consists of the flat core and the Lorentzian-like wing region. When the incident photon with the wavelength λ_{in} is scattered by an atomic hydrogen, the wavelength of scattered photon λ_s is given by,

$$\lambda_s = \lambda_{in}[1 + \frac{v_{rel}}{c}(1 - \mathbf{k_{in}} \cdot \mathbf{k_s})], \tag{6.18}$$

where $\mathbf{k_{in}}$ and $\mathbf{k_s}$ are the wavevector of the incident and scattered photon, respectively. The v_{rel} is the relative velocity between the current and previous scattering position. In Hubble-like outflow, v_{rel} is always positive because $\mathbf{k_{in}}$ and the relative velocity are along the same direction. The forward scattering does not change the wavelength, while the backward scattering causes a Doppler shift toward $+2v_{rel}$. Therefore, the wavelength becomes longer as long as the photon is scattered in the outflowing medium.

6.4.3.2 Velocity Offset of Lyα Line Peak

In this section, we carry out a systematic study of Lyα spectra for the various parameters in the Model S. Figure 6.13 – 6.15 show the total integrated Lyα spectra that we produce by summing all of the photons from the central source. In Figure 6.16, we show how the velocity offset (ΔV_{peak}) of the line peak varies as a function of v_{exp}, σ_{src}, and R_e/R_H. Note that the ΔV_{peak} should vary as a function of the distance from the center, but for simplicity, we adopt a single value of ΔV_{peak} measured from the integrated spectra. Our findings are:

- The velocity offset of the line peak increases with increasing N_{HI}.

- At $N_{\mathrm{HI}} \sim 10^{21}\,\mathrm{cm}^{-2}$, the line peak moves toward the redward with increasing v_{exp} and R_e.

- At $N_{\mathrm{HI}} \lesssim 10^{19}\,\mathrm{cm}^{-2}$, the dependence on v_{exp} is the opposite, although negligible. As v_{exp} increases, the line peak becomes closer to the line center.

- In the AGN case with $N_{\mathrm{HI}} \leq 10^{19}\,\mathrm{cm}^{-2}$, the absorption feature appears in the blue-ward near $-v_{\mathrm{exp}}$ due to the outflow.

- The velocity width of the central source (SFG vs. AGN) does not affect the velocity offset of the line peak.

Dependence on N_{HI}. First, we confirm the basic trend of Lyα RT that Lyα lines become broader, and the line peaks are shifted further in the velocity space as N_{HI} increases. The N_{HI} is the most dominant parameter affecting the ΔV_{peak} of resulting Lyα profiles. In the static medium (left panels in Figure 6.13), the separations between the double peaks increase while both red- and blue-side profiles being broader with increasing N_{HI}. Note that the spectra in the AGN case has much broader wings up to $\sim \pm 1000 \ \mathrm{km\,s^{-1}}$ than the SFG case due to directly escaping photons at $\Delta V > 500 \ \mathrm{km\,s^{-1}}$. However, the separations between the double peaks in both cases are similar at a given N_{HI}. In the presence of outflows (right panels), Lyα lines are redshifted. For example, the line peaks appear in $\Delta V \sim 800 \ \mathrm{km\,s^{-1}}$ for $N_{\mathrm{HI}} = 10^{21} \ \mathrm{cm^{-2}}$ cases.

Dependence in the high column density. In the high column density regime ($N_{\mathrm{HI}} = 10^{21} \ \mathrm{cm^{-2}}$) where multiple wing scattering dominates, the spectra become broader and more extended to the red with larger velocity offsets as v_{exp} and R_e increase. At $N_{\mathrm{HI}} \sim 10^{21} \ \mathrm{cm^{-2}}$, τ_{init} in the wing region (Figure 6.7) is large enough to cause additional wing scattering. Although the scattered photon's wavelength is in the wing region, multiple scatterings are required for the photons to escape the system. Hence, the Lyα spectrum in the outflow medium with this high column density shows an asymmetric

profile with a single red peak. In Figure 6.14, we show how Lyα spectra vary with $v_{\mathrm{exp}} = 0 - 400\,\mathrm{km\,s^{-1}}$ for the combinations of N_{HI} and σ_{src}. In the right panels ($N_{\mathrm{HI}} = 10^{21}\,\mathrm{cm^{-2}}$), we find that the spectra become broader and more extended to the redward with increasing v_{exp}. When the photon is multiply scattered in the wing region, the strong outflow causes large velocity changes in each scattering. The scattered photon in strong outflow becomes more redshifted and quickly escapes from the H I halo. Figure 6.15 is the same plot but showing the dependence of Lyα spectra on gas concentration ($R_e/R_H = 0.3,\ 0.5,\ 1,\ \mathrm{and}\ \infty$). In the right panels ($N_{\mathrm{HI}} = 10^{21}\,\mathrm{cm^{-2}}$), the line peak is shifted more toward the redward with increasing R_e because the higher R_e implies more neutral gas at the large distance; thus the photons are more likely to be scattered by the faster medium in the outer halo.

Dependence in the low column density. In the low column density regime ($N_{\mathrm{HI}} \lesssim 10^{19}\,\mathrm{cm^{-2}}$) where most of the photons can escape through single wing scattering, the resulting spectra have very small offset ($\Delta V_{\mathrm{peak}} = 0\text{--}100\ \mathrm{km\,s^{-1}}$) and become almost indistinguishable each other for a range of v_{exp} and R_e. For example, in the right panels in Figure 6.13, the spectra with $N_{\mathrm{HI}} = 10^{18-19}\,\mathrm{cm^{-2}}$ (gray and blue lines) show almost zero velocity offsets.

But we note that there is a trend such that the red peak of the Lyα spectra becomes closer to the systemic velocity with increasing v_{exp} (left panels of Fig, 6.14). Although this trend is negligible, this behavior is the opposite to that of the high column density ($N_{\mathrm{HI}} = 10^{21}\,\mathrm{cm}^{-2}$) case. This opposite trend arises because the photons in the red wing can directly escape the system in the low column density. As shown in Figure 6.7, the optical depth of initial photons (τ_{init}) in the redward ($\Delta V > 0\,\mathrm{km\,s}^{-1}$) is smaller than unity in the low column density. Note that due to the velocity field, the overall optical depth at $\Delta V > 0\,\mathrm{km\,s}^{-1}$ decreases with increasing v_{exp} while the optical depth is greatly enhanced on the blue side ($\Delta V < 0\,\mathrm{km\,s}^{-1}$). Because of this small optical depth, most of Lyα photons in the red wings of the input spectrum can directly escape and thus produce the observed asymmetric profiles with small velocity offsets. As v_{exp} increases, the overall optical depth decreases, and the line peak gets closer to the systemic velocity and also sharper. The photons escaping through scattering appear at $\Delta V < 2v_{\mathrm{exp}}$ in the redward because of large scattering angles ($> 90°$).

In this regime of the low column density, R_e affects the only sharpness of the line peak. Figure 6.15, we show Lyα spectra for $R_e = 0.3R_H - \infty$, respectively. The left panels of Figure 6.15 show that the peaks become sharper with decreasing R_e although its effect is negligible.

Absorption features in AGN case. In the AGN case with the low column density ($N_{\mathrm{HI}} \lesssim 10^{19}\,\mathrm{cm}^{-2}$), the outflows imprint absorption features in the blueward of the Lyα spectra. In the bottom left panel of Figure 6.14, we find that this blue absorption feature becomes broader and more blueshifted with increasing v_{exp}. This feature originates from the optically thick core region, i.e., the central flat part in Figure 6.7 that is stretched from $\Delta V = 0\ \mathrm{km\,s}^{-1}$ to $-v_{\mathrm{exp}}$. This increasing strength of this blue absorption as a function of v_{exp} can explain why the surface brightness profiles are more extended in the strong outflow. The initial photons in $\Delta V = [0,\ -v_{\mathrm{exp}}\ ]$ become optically thick and scattered into outer region by the fast-moving medium. Most of the scattering occurs near the line center of the atom in this low column density region. When the photon's wavelength approach to $-v_{\mathrm{exp}}$, the scattering probability near the surface of the H I halo increase. In the top left panel for the SFG case, the blue absorption features are not produced. Because the σ_{src} is smaller than v_{exp}, the initial Lyα spectrum does not cover the optically thick core region.

Dependence on multiple parameters. In Figure 6.16, we summarize how the velocity offset ΔV_{peak} depends on v_{exp} and R_e/R_H for three σ_{src} = 100, 200, 400 $\mathrm{km\,s}^{-1}$. We confirm that (1) ΔV_{peak} increases with increasing N_{HI}, (2) ΔV_{peak} increases with increasing v_{exp} and R_e/R_H in the case of

high column density ($N_{\mathrm{HI}} \sim 10^{21}\,\mathrm{cm}^{-2}$), (3) ΔV_{peak} is not sensitive to v_{exp} and R_e/R_H at $N_{\mathrm{HI}} \lesssim 10^{19}\,\mathrm{cm}^{-2}$, and finally (4) ΔV_{peak} does not depend on σ_{src}.

6.5 Summary

In this article, we investigate Lyα scattering from the central sources within spherical H I halos of $\sim 100\,\mathrm{kpc}$ through the Monte-Carlo radiative transfer simulation. In our simulation, photons carry multi-dimensional information: position, wavelength, direction, and polarization state. We test if scattering by the H I halo alone can produce spatially extended features over $\sim 100\,\mathrm{kpc}$ scale like the recently found Lyα blobs or enormous Lyα nebulae. We find that the column density of the scattering medium is the major parameter to determine the size of the observable Lyα halos. For a fixed Lyα luminosity of 10^{44} erg s^{-1} at $z = 3$, a considerable column density of $N_{\mathrm{HI}} \gtrsim 10^{20}\,\mathrm{cm}^{-2}$ is required to make Lyα halos larger than $R_{obs} \gtrsim 50\,\mathrm{kpc}$.

We explore how various observables (surface brightnesses, velocity profiles, and polarizations) depend on the total H I column density, the most dominant parameter. As N_{HI} increases, we find that (1) the surface brightness becomes more extended and flattened, (2) the velocity offset (ΔV_{peak}) and the line width of the Lyα spectra increase, however, (3) the polarization behavior is more complex and does not monotonically vary as a function

204

of N_{HI}. In the low column density regime, we show that the velocity off-set of the line peak does not depend on the expanding velocity, the surface brightness strongly depends on the type of embedded source, and the polarization decreases due to core scattering. On the other hand, in the high column density regime ($N_{\mathrm{HI}} = 10^{21}\,\mathrm{cm}^{-2}$), the properties of Ly$\alpha$ halo depend on the kinematics and density profiles of H I halo regardless of the input sources. As v_{exp} decreases and/or R_e/R_H increases, we find that the surface brightness profile becomes more extended, the degree of polarization increases, and the velocity offset decreases.

In the future, we will extend our RT calculations to the halos where the medium is composed of small clumps and compare them with the results for the smooth medium presented in this article.

References

Ahn, S. -H., Lee, H.-W., 2015, JKAS, 48, 195

Ahn, S.-H., Lee, H.-W. Lee, H. M., 2002, ApJ, 567, 922

Angel, J. R. P., 1969, ApJ, 158, 219

Angeloni, R., Contini, M., Ciroi, S., Rafanelli, P., 2010, MNRAS, 402, 2075

Antonucci, R., 1993, ARA&A, 31, 473

Antonucci, R., Miller, J. S., 1985, ApJ, 297, 621

Akras, S., Gonçalves, D. R., Ramos-Larios, G., 2017, MNRAS, 465, 1289

Akras, S., Guzman-Ramirez, L., Leal-Ferreira, M. L., Ramos-Larios, G., 2019, ApJS, 240, 21

Ao, Y., Zheng, Z., Henkel, C., Nie, S., Beelen, A., Cen, R., Dijkstra, M., 2020, Nature Astronomy, 47

Arrieta, A., Torres-Peimbert, S, 2002, RMxAC, 12, 154

Arrieta, A., Torres-Peimbert, S, 2003, ApJS, 147, 97

Arrigoni Battaia, F., Hennawi, J. F., Prochaska, J. X., Cantalupo, S., 2015, ApJ, 809, 163

Arrigoni Battaia, F., Hennawi, J. F., Prochaska, J. X., Oñorbe, J., Farina, E. P., Cantalupo, S., Lusso, E., 2019, MNRAS, 482, 3162

Bach, K, Lee, H.-W, 2014, JKAS, 47, 187

Balick, B., 1989, AJ, 97, 476

Bethe, H. A. & Salpeter, E. E., 1957, Quantum Mechanics of One and Two Electron Atoms (New York: Academic Press)

Bentz, M. C. et al., 2009, ApJ, 705, 199

Berestetskii, V. B., Lifshitz, E. M., Pitaevskii, V. B., 1971, Relativistic quantum theory(Reading: Pergamon Press)

Birriel, J., Espey, B. R., Schulte-Ladbeck, R. E., 2000, ApJ, 545, 1020

Birriel, J. J., 2004, ApJ, 612, 1136

Blandford, R. D., McKee, C. F., 1982, ApJ, 255, 419

Blandford, R. D., Netzer, H., Woltjer, L., Courvoisier, T. J.-L., Mayor, M., 1990, Active Galactic Nuclei(Reading: Springer-Verlag)

Borisova, E., Cantalupo, S., Lilly, S. J., Marino, R. A., Gallego, S. G., et al., 2016, ApJ, 831, 39

Brinch, C., Hogerheijde, M. R., 2010, A&A, 523, A25

Cabot, S. H. C., Cen, R., Zheng, Z., 2016, MNRAS, 462, 1076

Celnikier, L. M., Lefévre, J., 1974, A&A, 36, 429

Chandrasekhar, 1960, Radiative Transfer (Reading : New York Dover)

Chang, S.-J., Heo, J.-E., Di Mille, F., Angeloni, R., Palma, T., Lee, H.-W., 2015, ApJ, 814, 98

Chang, S.-J., Lee, H.-W., Yang, Y., 2017, MNRAS, 464, 5018

Chang, S.-J., Lee, H.-W., Lee, H.-G., Hwang, N., Ahn, S.-H., Park, B.-G., 2018, ApJ, 866, 129

Chen, Z., Frank, A., Blackman, E. G., Nordhaus, J., Carroll-Nellenback, J., 2017, MNRAS, 468, 4465

Choi, B.-E., Chang, S.-J., Lee, H.-G., Lee, H.-W., 2020, ApJ, 889, 2

Choi, B.-E., Lee, H.-W., 2020, ApJL, 903L, 39

Chiang, C.-Y., Cackett, E. M., Gandhi, P., & Fabian, A., 2013, MNRAS, 430, 2943

Cohen, M. H., Ogle, P. M., Tran, H. D., Vermeulen, R. C., Miller, J. S., Goodrich, R. W., Martel, A. R., 1995, ApJ, 448, L77

Comastri, A., Setti, G., Zamorani, G., Hasinger, G., 1995, A&A, 296, 1

Comastri, A., Gilli, R., Marconi, A., Risaliti, G., Salvati, M. 2015, A&A, 574, 10

Daddi, E., Valentino, F., Rich, R. M., Neill, J. D., 2020, arXiv:2006.11089

Dey, A., Bian, C., Soifer, B. T., et al. 2005, ApJ, 629, 654

de Val-Borro, M., Karovska, M., Sasselov, D. D., Stone, J. M., 2017, MN-RAS, 468, 3408

Dietrich, M. et al., 2012, ApJ, 757, 53

Dijkstra, M., Kramer, R., 2012, MNRAS, 424, 1672

Dopita, M. A., Nicholls, D. C., Sutherland, R. S., Kewley, L. J., Groves, B. A., 2016, ApJL, 824, L13

Dumm, T., Schmutz, W., Schild, H., Nussnaumer, H., 1999, A&A, 349, 169

Duval, F., Schaerer, D., Östlin, G., Laursen, P., 2014, A&A, 562, 52

Dijkstra, M., Loeb, A., 2008, MNRAS, 386, 492

Eide, M. B., Gronke, M., Dijkstra, M., Hayes, M., 2018, ApJ, 856, 156

Fekel, F. C., Hinkle, K. H., Joyce, R. R., Skrutskie, M. F., 2000, AJ, 120, 3255

Francis, P. J., et al. 2001, ApJ, 554, 1001

Gilli, R., Comastri, A., Hasinger, G., 2007, A&A, 463, 79

Gavrila, M., 1967, PhRv, 163, 147

Geach, J. E., Narayanan, D., Matsuda, Y., et al., 2016, ApJ, 832, 37

Groves, B., Dopita, M. A., Williams, R. E., Hua, C.-T., 2002, PASA, 19, 425

Gronke, M., Dijkstra, M., McCourt, M., Oh, S. P., 2016, ApJL, 833, 26

Gronke, M., Dijkstra, M., McCourt, M., Oh, S. P., 2017, A&A, 607, 71

Harries, T. J., Howarth, I. D., 1996, A&AS, 119, 61

Hansen, M., Oh, S. P., 2006, MNRAS, 367, 979

Hayes, M., Scarlata, C., Siana, B., 2011, Nature, 476, 304

Hennawi, J. F., Prochaska, J. X., Cantalupo, S., Arrigoni-Battaia, F., 2015, Science, 348, 779

Hennawi, J. F., Prochaska, J. X., 2013, ApJ, 766, 58

Heo, J.-E., Lee, H.-W., 2015, JKAS, 48, 105

Heo, J.-E., Angeloni, R., Di Mille, F., Palma, T., Lee, H.-W., 2016, ApJ, 833, 286

Hummer, D. G., 1962, MNRAS, 125, 21

Hummer, D. G., Mihalas, D., 1967, ApJ, 150L, 57

Ikeda, Y., Akitaya, H., Matsuda, K., Homma, K., Seki, M., 2004, ApJ, 604, L357

Ivison, R. J., Bode, M. F., Meaburn, J., 1994, A&AS, 103, 2011

Isliker, H., Nussbaumer, H., Vogel, M., 1989, A&A, 219, 271

Jung, Y.-C., Lee, H.-W., 2004, MNRAS, 355, 221

Kang, E.-H., Lee, B.-C., Lee, H.-W., 2009, ApJ, 695, 542

Kenyon, S. J., 1986, The Symbiotic Stars, Cambridge : Cambridge University Press

Kenyon, S. J., 2009, The Symbiotic Stars(Reading, UK: Cambridge University Press)

Kim, H. J., Lee, H.-W. & Kang, S., 2007, MNRAS, 374, 187

Kim, E., Yang, Y., Zabludoff, A., Smith, P., Jannuzi, B., Lee, M. G., Hwang, N., Part, B.-G., 2020, ApJ, 894, 33

Koratkar, A., Antonucci, R. R. J., Goodrich, R. W., Bushouse, H., Kinney,
  A. L., 1995, ApJ, 450, 501

Laor, A., 2006, ApJ, 643, 112

Lee, H.-W., Blandford, R. D., Western, L., 1994, MNRAS, 267, 303

Lee, H.-W., & Blandford, R. D., 1997, MNRAS, 288, 19

Lee, K.-W., Lee, H.-W., 1997, MNRAS, 292, 573

Lee, H.-W., & Yun, J. H., 1998, MNRAS, 301, 193

Lee, H.-W., Park. M.-G., 1999, ApJL, 515, L89

Lee, H.-W., 2000, ApJ, 541, L25

Lee, H.-W., 2000, ApJL, 541, L25

Lee, H.-W., Hyung, S., 2000, ApJL, 530, L49

Lee, H.-W., Jung, Y.-C., Song, I.-O., Ahn, S.-H., 2006, ApJ, 636, L1045

Lee, H.-W., 2013, ApJ, 772, 123

Lee, H.-W., 2000, ApJ, 541, 25

Lee, H.-W., Kang, Y.-W., Byun, Y.-I., 2001, ApJ, 551, 121

Lee, H.-W., Jung, Y.-C., Song, I.-O., Ahn, S.-H., 2006, ApJ, 636, 1045

Lee, Y.-M., Lee, H.-W., Lee, H.-G., Angeloni, R., 2019, MNRAS, 487, 2166

Li, Z., Steidel, C. C., Gronke, M., Chen, Y., 2021, 2021, MNRAS, 502, 2389

Lykins, M. L., Ferland, G. J., Kisielius, R., 2015, ApJ, 807, 118

Magdziarz, Pawel, Zdziarski, Andrzej A., 1995, MNRAS, 273, 837

Mas-Ribas, L., Chang, T.-C., 2020, Phys. Rev. D, 101, 083032

Matsuda, Y., Yamada, T., Hayashino, T., et al. 2004, AJ, 128, 569

Matsuda, Y., Yamada, T., Hayashino, T., et al. 2011, MNRAS, 410, L13

Miller, J. S., Goodrich, R. W., 1990, ApJ, 355, 456

Mikołajewska, J., 2012, Baltic Astronomy, 21, 5

Murray, N., Chiang, J., 1995, ApJ, 454, 105

Mürset, U., Schmid, H., M., 1999, A&AS, 137, 473

Mürset, U., Nussbaumer, H., Schmid, H., M., Vogel, M., 1991, A&A, 248, 458

Netzer, H., 2015, ARA&A, 53, 365

Neufeld, D. A., 1990, ApJ, 350, 216

Neufeld, D. A., 1991, ApJL, 370, L85

Nilsson, K. K., Fynbo, J. P. U., Møller, P., Sommer-Larsen, J., & Ledoux, C. 2006, A&A, 452, L23

Nussbaumer, H., Schmid, H. M., Vogel, M., 1989, A&A, 211, L27

Ogle, P. M., Cohen, M. H., Miller, J. S., Tran, H. D., Fosbury, R. A. E., Goodrich, R. W., 1997, ApJ, 482, L37

Osterbrock, D. E., Ferland, G. J., 2006, Astrophysics of gaseous nebulae and active galactic nuclei (Reading CA: University Science Books)

Ouchi, M., Shimasaku, K., Akiyama, M., Simpson, C., et al., 2008, ApJS, 176, 301

Ouchi, M., Harikane, Y., Shibuya, T., Shimasaku, K., et al., 2018, PASJ, 70S, 13

Park, Daeseong, 2012, ApJ, 747, 30

Peterson, B. M., 1993, PASP, 105, 247

Peterson, B. M. 1997, An Introduction to Active Galactic Nuclei, Cambridge: Cambridge University Press

Peterson, Bradley M., 1993, PASP, 105, 247

Péquignot, D., Baluteau, J.-P., Morisset, C., Boisson, C., 1997, A&A, 323, 217

Phillips, K. C., Meszaros, P., 1986, ApJ, 310, 284

Prescott, M. K. M., Dey, A., & Jannuzi, B. T. 2012, ApJ, 748, 125

Prescott, M. K. M., Dey, A., Jannuzi B. T., 2009, ApJ, 702, 554

Reynolds, C. S., et al., 2015, ApJ

Ricci, C.; Ueda, Y.; Ichikawa, K.; Paltani, S.; Boissay, R.; Gandhi, P.; Stalevski, M.; Awaki, H, 2014, A&A, 142, 15

Rybicki, G. B., Loeb, A., 1999, ApJL, 520, L79

Sadeghpour, H. R., Dalgarno A., 1992, JPhB, 25, 4801

Saladino, M. I., Pols, O. R., van der Helm, E., Pelupessy, I., Portegies Zwart, S., 2018, A&A, 618, A50

Sakurai, J. J., 1967, Advanced Quantum Mechanics, Reading: Addison-Wesley

Saslow, W. M., Mills, D. L., 1969, Phys. Rev., 187, 1025

Schmid, H. M., 1989, A&A, 211L, 31

Schmid, H. M., 1992, A&A, 254, 224

Schmid, H. M., 1995, MNRAS, 275, 227

Schmid, H. M., Corradi, R., Krautter, J., Schild, H, 2000, A&A, 355, 261

Schild, H., Schmid, H. M., 1996, A&A, 310, 211

Sekerá (š, M., Skopal, A., 2012, MNRAS, 427, 979

Sekeráš, M., Skopal, A., 2015, ApJ, 812, 162

Selvelli, P. L., Bonifacio, P., 2000, A&A, 364, 1

Seon, K.-I., Min, K. W., Choi, C. S., Nam, U. W., 1994, JKAS, 27, 45

Seon, K.-I., 2009, PKAS, 24, 43

Seon, K.-I., 2015, JKAS, 47, 57

Seon, K.-I., Kim, C.-G., 2020, ApJS, 250, 9

Seon, K.-I., Song, H., Chang, S.-J., 2021, ApJS, ? , ?

Skopal, A., 2006, A&A, 457, 1003

Skopal, A., 2008, JAVSO, 36, 9

Shore, S. N., Wahlgren, G. M., Genovali1, K., Bernabei, S., Koubsky, P., 2010, A&A, 510, A70

Stenflo, J. O., 1980, A&A, 84, 68

Storey, P. J., Hummer, D. G., 1995, MNRAS, 272, 41

Steidel, C. C., Adelberger, K. L., Shapley, A. E., et al. 2000, ApJ, 532, 170

Tomov, N. A., Tomova, M. T., 2002, A&A, 388, 202

Tomov, N. A., Tomova, M. T., Bisikalo, D. V., 2008, MNRAS, 389, 829

Totani, T., Aoki, K., Hattori, T., Kawai, N., 2016, PASJ, 68, 15

Tran, H. D., Brotherton, M. S., Stanford, S. A., van Breugel, W., Dey, A., Stern, D., Antonucci, R., 1999, ApJ, 516, 85

Tran, H. D., 2010, ApJ, 711, 1174

Trebitsch, M., Verhamme, A., Blaizot, J., Rosdahl, J., 2016, A&A, 593, 122

Travascio, A., Zappacosta, L, Cantalupo, S., Piconcelli, E., Arrigoni Battaia, et al., 2020, A&A, 635, 157

Trippe, S., 2014, JKAS, 47, 15

van de Steene, G. C., Wood, P. R., van Hoof, P. A. M., 2000, ASPC, 199, 191

Vanden Berk, D. E., et al., 2001, AJ, 122, 549

Vanden Berk, D. E., Richards, G. T., Bauer, A., 2001, AJ, 122, 549

van Gronigen, E., 1993, MNRAS, 264, 975

Van Winckel, H., Duerbeck, H. W., Schwarz, H. E., 1993, A&AS, 102, 401

Verhamme, A., Schaerer, D., Maselli, A., 2006, A&A, 460, 397

Yang, Y., Zabludoff, A., Tremonti, C., Eisenstein, D., Davé, R. 2009, ApJ, 693, 1579

Yang, Y., Zabludoff, A., Eisenstein, D., Davé, R. 2010, ApJ, 719, 1654

Yang, Y., Zabludoff, A., Jahnke, K., Dave, R., Schectman, S. A., Kelson, D. D., 2011, ApJ, 735, 87

Yang, Y., Walter, F., Decarli, R., Bertoldi, F., Weiss, A., Dey, A., 2014, ApJ, 787, 171

Yoo, J. J., Bak, J.-Y., Lee, H.-W., 2002, MNRAS, 336, 467

You, C., Zabludoff, A., Smith, P., Yang, Y., Kim, E., Jannuzi, B., Prescott, M. K. M., Matsuda, Y., Lee, M. G., 2017, ApJ, 834, 182

Zheng Wei, Kriss, Gerard A., Telfer, Randal C., Grimes, John P., Davidsen, Arthur F., 1997, AJ, 475, 469

Zheng, Z., Miralda-Escudé, J., 2002, ApJ, 578, 33

국문초록

중성 수소에 의한 레일리 산란과 라만 산란을 통한 복사 전달 연구

세종대학교 대학원

천문우주학과

장석준

기둥 밀도가 높은 중성 수소 지역에서 원자외선 광자는 레일리 산란과 라만 산란을 겪으면서 실공간과 주파수 공간 모두에서 확산 과정을 거쳐 전달된다. 우리는 3차원 실공간에서 주파수 변화와 편광 정보를 함께 취급하는 몬테칼로 코드인 STaRS (Sejong Radiative Transfer through Raman and Rayleigh Scattering)를 개발하였다. 여기에서 고려되는 수소 원자에 의한 라만 산란은 바닥 상태에 있는 중성 수소에 $Ly\alpha$보다 에너지가 큰 원자외선이 입사하고, 수소 원자가 $2s$ 상태로 되가라앉으면 가시광 영역 혹은 이보다 더 낮은 에너지를 갖는 광자가 방출되는 과정에 해당한다.

라만 산란에 의하여 $Ly\beta$와 $Ly\gamma$ 근처의 원자외선 광자들은 $H\alpha$와 $H\beta$ 근처의 가시광으로 전환되며, 산란 효율이 선 중심에서 급격하게 커지므로, 라만 산란광은 발머 방출선의 인근에서 폭이 매우 넓은 날개 영역을 형성한다. 발머 방출선의 날개 영역은 백색왜성과 거성의 쌍성계인 공생별에서 잘 관측되고

있으며, 특히 Hα의 날개 영역의 분광학적 폭은 수천 km s^{-1}에 이른다고 알려져 있다. 우리는 몬테 칼로 방법을 적용하여 라만 산란에 의한 발머선 형성 과정을 모사하고 두 공생별 Z Andromedae와 AG Draconis의 관측 자료와 비교하였다. 이들 두 공생별에서 Hα의 날개는 Hβ 날개보다 더 강하고 큰 폭으로 나타났으며, 이것은 라만 산란에 의한 날개 형성 과정에서 예측되는 바와 잘 일치한다.

활동성은하핵의 통일 모형에 따르면 넓은폭 방출선 지역을 가리는 두꺼운 도넛 성분이 존재하며, 이 지역에 원자외선이 입사하면 라만 산란이 일어날 수 있다. 공생별에서와 비슷한 방법을 적용하여, 우리는 활동은하의 통일 모형에서 기대되는 Hα와 Hβ의 날개 형성 과정을 조사하였다.

활동성은하핵의 넓은폭 방출선 Lyα 광자들은 두꺼운 도넛 성분에 입사하면 기둥 밀도가 10^{22} cm^{-2}를 넘는 경우에 Rayleigh 산란될 수 있다. 또한, 산란 지역의 비등방성 때문에 Lyα는 선편광을 갖게 된다. 특히 선중심 영역은 광학 두께가 몹시 크고, 날개 지역은 광학 두께가 작으므로, 매우 다른 산란 과정을 겪으면서 편광도와 편광 방향이 크게 대비된다. 활동성은하핵에 대한 Lyα 근처의 정밀한 spectropolarimetry를 통해 활동성 은하핵의 통일 모형의 검증을 시도할 수 있을 것으로 기대된다.

Lyα blob(LAB 천체)은 100 kpc에 걸쳐 Lyα 방출을 보이는 적색이동이 큰 초창기 우주에서 발견되는 천체로서 은하단의 초창기 형태로 간주되고 있다. 우리는 활동은하핵으로부터 형성된 Lyα 광자가 주변에 분포하는 중성 수소 지역으로 입사하여 산란되어 Lyα halo를 형성하는 과정을 몬테 칼로 기법으로

기술하였다. 이 과정에서 예상되는 Lyα의 표면 밝기와 선편광을 계산하였다. Lyα halo형성에 가장 큰 영향을 주는 물리량은 중성 수소의 기둥 밀도임을 제시하였다.

주요어휘: 복사전달, 산란, 편광